NICKEL COMPLEXES CONTAINING N_4 SCHIFF-BASE MACROCYCLES DEREIVED FROM DIPHENYLAMINE-2,2'-DICARBOXALDEHYDE FOR CATALYTIC CO_2 REDUCTION

Mr. Methasit Juthathan

จุฬาลงกรณ์มหาวิทยาลัย
CHULALONGKORN UNIVERSITY

A Dissertation Submitted in Partial Fulfillment of the Requirements
for the Degree of Doctor of Philosophy in Chemistry
Department of Chemistry
FACULTY OF SCIENCE
Chulalongkorn University
Academic Year 2022
Copyright of Chulalongkorn University

สารเชิงซ้อนนิกเกิลที่ประกอบด้วย N_4 ชิฟเบสมาโครไซเคิลจากไดเฟนิลเอมีน-2,2'-ไดคาร์บอกซัลดีไฮด์ สำหรับรีดักชันเชิงเร่งปฏิกิริยาของคาร์บอนไดออกไซด์

นายเมธาสิทธิ์ จุฑาทานต์

จุฬาลงกรณ์มหาวิทยาลัย
CHULALONGKORN UNIVERSITY

วิทยานิพนธ์นี้เป็นส่วนหนึ่งของการศึกษาตามหลักสูตรปริญญาวิทยาศาสตรดุษฎีบัณฑิต
สาขาวิชาเคมี ภาควิชาเคมี
คณะวิทยาศาสตร์ จุฬาลงกรณ์มหาวิทยาลัย
ปีการศึกษา 2565
ลิขสิทธิ์ของจุฬาลงกรณ์มหาวิทยาลัย

Thesis Title	NICKEL COMPLEXES CONTAINING N_4 SCHIFF-BASE MACROCYCLES DEREIVED FROM DIPHENYLAMINE-2,2'-DICARBOXALDEHYDE FOR CATALYTIC CO_2 REDUCTION
By	Mr. Methasit Juthathan
Field of Study	Chemistry
Thesis Advisor	Assistant Professor PANNEE LEELADEE, Ph.D.

Accepted by the FACULTY OF SCIENCE, Chulalongkorn University in Partial Fulfillment of the Requirement for the Doctor of Philosophy

..... Dean of the FACULTY OF SCIENCE
(Professor POLKIT SANGVANICH, Ph.D.)

DISSERTATION COMMITTEE

..... Chairman
(Associate Professor Khamphee Phomphrai, Ph.D.)

..... Thesis Advisor
(Assistant Professor PANNEE LEELADEE, Ph.D.)

..... Examiner
(Professor THAWATCHAI TUNTULANI, Ph.D.)

..... Examiner
(Assistant Professor WIPARK ANUTRASAKDA, Ph.D.)

..... Examiner
(Assistant Professor JUNJUDA UNRUANGSRI, Ph.D.)

..... External Examiner
(Assistant Professor Teera Chantarojsiri, Ph.D.)

จุฬาลงกรณ์มหาวิทยาลัย
Chulalongkorn University

เมธาสิทธิ์ จุฑาทานต์ : สารเชิงซ้อนนิกเกิลที่ประกอบด้วย N_4 ชิฟเบสมาโครไซเคิลจากไดเฟนิลเอมีน-2,2'-ไดคาร์บอกซัลดีไฮด์สำหรับรีดักชันเชิงเร่งปฏิกิริยาของคาร์บอนไดออกไซด์. (NICKEL COMPLEXES CONTAINING N_4 SCHIFF-BASE MACROCYCLES DEREIVED FROM DIPHENYLAMINE-2,2'-DICARBOXALDEHYDE FOR CATALYTIC CO_2 REDUCTION) อ.ที่ปรึกษาหลัก : ผศ. ดร.พรรณี ลีลาดี

ในวิทยานิพนธ์ฉบับนี้ สารเชิงซ้อนนิกเกิล(II) ที่ประกอบด้วย N_4 ชิฟเบสมาโครไซเคิลจากไดเฟนิลเอมีน-2,2'-ไดคาร์บอกซัลดีไฮด์ (1-Ni, 2-Ni และ $[2\text{-Ni}]^{Me}$) ได้ถูกสังเคราะห์และทดสอบปฏิกิริยาเชิงไฟฟ้าเคมีสำหรับการรีดักชันของคาร์บอนไดออกไซด์ สารเชิงซ้อนนิกเกิลดังกล่าวได้รับการทดสอบคุณสมบัติทางไฟฟ้าเคมีด้วยเทคนิคไซคลิกโวลแทมเมทรี พบว่าสารเชิงซ้อนของนิกเกิล 1-Ni และ 2-Ni แสดงการเพิ่มสัญญาณของกระแสไฟฟ้าในสภาวะที่มีก๊าซคาร์บอนไดออกไซด์ แสดงให้เห็นถึงความสามารถที่จะใช้สารเชิงซ้อนเหล่านี้สำหรับรีดักชันเชิงเร่งปฏิกิริยาของคาร์บอนไดออกไซด์ ในขณะที่มีการเพิ่มของสัญญาณกระแสไฟฟ้าน้อยมากเมื่อใช้สารเชิงซ้อนนิกเกิล $[2\text{-Ni}]^{Me}$ เพื่อพัฒนาตัวเร่งปฏิกิริยารีดักชันของคาร์บอนไดออกไซด์แบบวิวิธพันธ์ในตัวกลางที่เป็นน้ำ สารเชิงซ้อนนิกเกิลเหล่านี้ได้ถูกยึดติดบนวัสดุรองรับคาร์บอนที่มีการเจือด้วยไนโตรเจนผ่านอันตรกิริยาแบบนอนโคเวเลนต์ ตัวเร่งปฏิกิริยาไฮบริดระหว่างสารเชิงซ้อนนิกเกิลบนวัสดุรองรับคาร์บอนที่มีการเจือด้วยไนโตรเจน (Ni@NG) แสดงผลรีดักชันของคาร์บอนไดออกไซด์เชิงไฟฟ้าเคมีที่น่าพอใจโดยสามารถเปลี่ยนก๊าซคาร์บอนไดออกไซด์เป็นผลิตภัณฑ์ก๊าซคาร์บอนมอนอไซด์ด้วยประสิทธิภาพฟาราเดอิก 60-80% ที่ศักย์ไฟฟ้าเกินตัว 0.56 V ตัวเร่งปฏิกิริยาไฮบริด $[2\text{-Ni}]^{Me}$@NG แสดงให้เห็นว่าผลของหมู่ฟังก์ชัน N-H บนลิแกนด์ต่อการเร่งปฏิกิริยารีดักชันของคาร์บอนไดออกไซด์มีบทบาทน้อยลงในสภาวะการเร่งปฏิกิริยาแบบวิวิธพันธ์ซึ่งมีน้ำและไบคาร์บอเนตเป็นสารให้พันธะไฮโดรเจนและแหล่งโปรตอนทดแทน นอกจากนี้สารเชิงซ้อนนิกเกิลที่มีองค์ประกอบของหมู่อะคริดีนและชิฟเบส ($[NiL^{ACR}]^{2+}$) ถูกสังเคราะห์ขึ้นผ่านกลไกการจัดเรียงตัวใหม่ของไดเฟนิลเอมีน-2,2'-ไดคาร์บอกซัลดีไฮด์ และได้รับการวิเคราะห์คุณสมบัติทางไฟฟ้าเคมีเบื้องต้นผ่านการทดสอบการเร่งปฏิกิริยาการผลิตก๊าซไฮโดรเจนอีกด้วย

สาขาวิชา เคมี ลายมือชื่อนิสิต .....

ปีการศึกษา 2565 ลายมือชื่อ อ.ที่ปรึกษาหลัก .....

6172873123 : MAJOR CHEMISTRY

KEYWORD: Nickel complexes, Organic-inorganic hybrid composites, Electrocatalysis, Carbon dioxide reduction

Methasit Juthathan : NICKEL COMPLEXES CONTAINING N_4 SCHIFF-BASE MACROCYCLES DEREIVED FROM DIPHENYLAMINE-2,2'-DICARBOXALDEHYDE FOR CATALYTIC CO_2 REDUCTION. Advisor: Asst. Prof. PANNEE LEELADEE, Ph.D.

In this dissertation, nickel(II) complexes featuring N_4-Schiff base macrocycles derived from diphenylamine-2,2'-dicarboxaldehyde (1-Ni and 2-Ni) with a new crystal structure ([2-Ni]^{Me}) were synthesized and investigated for electrochemical CO_2 reduction (ECR). Cyclic voltammetry (CV) of two nickel complexes, 1-Ni and 2-Ni, illustrated the catalytic response whereas one, [2-Ni]^{Me}, virtually remained peak-shaped in the presence of CO_2, indicating the feasibility of ECR activity for these nickel complexes. To develop heterogeneous ECR catalysts in aqueous media, all nickel complexes were adhered on N-doped graphene (NG) through non-covalent interaction, obtaining Ni@NG hybrid catalysts. The Ni@NG catalysts showed satisfactory ECR activity with the faradaic efficiency of CO production (FE_{CO}) of 60-80% at the overpotential of 0.56 V *vs.* RHE. The ECR activity of Ni@NG catalysts demonstrated that the necessity of N-H functionality from the ligand is less important in the heterogeneous aqueous system owing to plenty of viable hydrogen-bond and proton donors from water and bicarbonate species. Besides, an unexpected formation of nickel complexes bearing acridine-based Schiff base ligand ([NiL^{ACR}]$^{2+}$) was obtained *via* the rearrangement of diphenylamine-2,2'-dicarboxaldehyde. In addition, electrochemical properties and hydrogen evolution reaction of the nickel complexes were preliminary investigated.

จุฬาลงกรณ์มหาวิทยาลัย
Chulalongkorn University

Field of Study: Chemistry Student's Signature .....

Academic Year: 2022 Advisor's Signature .....

ACKNOWLEDGEMENTS

The completion of my Ph.D. dissertation depends on several key people, funding sources, and organizations. Firstly, I would like to convey my heartfelt gratitude to my advisor, Assistant Professor Pannee Leeladee, for her supervision throughout my Ph.D. study. Without her tremendous suggestions, I would not have been successful in completing this project. I am extremely grateful to the chair of the committee – Associate Professor Khamphee Phomphrai. Also, I would like to express my deepest appreciation to the defense committee, including Professor Thawatchai Tuntulani, Assistant Professor Wipark Anutrasakda, Assistant Professor Junjuda Unruangsri, and Assistant Professor Teera Chantarojsiri.

My endeavor toward Ph.D. pursuit would not have been possible without the assistance of the following people: Professor Patchanita Thamyongkit and Dr. Teera Butburee for giving me the opportunity to conduct electrochemical experiments and use resources in the research laboratory. I am also thankful for Assistant Professor Kittipong Chainok, who kindly helped me in crystallographic techniques. My humble thanks go to Professor Thawatchai Tuntulani for his insightful comments and suggestions. I would like to express my special thanks to Assistant Professor Teera Chantarojsiri, who generously provided insight into electrochemistry.

I had the pleasure of working and collaborating with my senior colleagues – Mr. Jirapong Luangchaiyaporn and Mr. Permsak Chairat. I learned a lot of experiences, skills, and competencies from them throughout the projects. Being a part of Supramolecular Chemistry Research Unit (SCRU) is beautiful and fantastic. I had precious experiences and grew up with the members of SCRU. So, I would like to express my deep thanks to all current and former members of SCRU. Many thanks to my high school and college friends and colleagues for the fun times we had together. Plus, I would like to thank everyone who has been there for me emotionally and intellectually as I have proceeded with my Ph.D. journey.

Besides my lovely and supportive people, it is undeniable that I would not have undertaken this journey without financial support. Therefore, I would like to take

จุฬาลงกรณ์มหาวิทยาลัย
Chulalongkorn University

this unique opportunity to acknowledge my funding bodies. I gratefully acknowledge Science Achievement Scholarship of Thailand (SAST) and Research Cess Fund from Malaysia-Thailand Joint Authority (MTJA) during my 5-year study.

Finally, I would like to thank my lovely family – father, mother, brothers, uncle, aunt, and cousin – for their pure love. They have never opposed my good intention and have always supported me every step of the way. Especially, my greatest love and profound appreciation goes to my mother for her unwavering support and encouragement.

Methasit Juthathan

จุฬาลงกรณ์มหาวิทยาลัย
Chulalongkorn University

TABLE OF CONTENTS

Page

ABSTRACT (THAI) iii

ABSTRACT (ENGLISH) iv

ACKNOWLEDGEMENTS v

TABLE OF CONTENTS vii

LIST OF TABLES x

LIST OF FIGURES xi

CHAPTER 1 INTRODUCTION AND THESIS OBJECTIVES 16

1.1 Rising of atmospheric CO_2 level 16

1.2 CO_2 transformation and utilization 17

1.2.1 Reverse water-gas shift reaction 17

1.2.2 Direct CO_2-to-methanol conversion 17

1.2.3 CO_2 methanation (Sabatier reaction) 18

1.2.4 Dry reforming of CH_4 (DRM) 18

1.2.5 Photochemical CO_2 reduction 19

1.3 Electrochemical CO_2 reduction 20

1.4 Chemistry of carbon dioxide and its reduction mechanism with catalytic metal centers 21

1.5 Transition metal-based molecular catalysts for ECR 24

1.6 Secondary-sphere effects in electrochemical CO_2 reduction 30

1.6.1 Enzymatic catalysis of CO_2 reduction 30

1.6.2 Synthetic molecular ECR catalysts based on the secondary sphere effects 31

จุฬาลงกรณ์มหาวิทยาลัย
Chulalongkorn University

1.7 Carbon-supported molecular catalysts – trend for modern heterogenous catalysis 35

1.8 Nickel(II) complexes featuring N_4-Schiff base macrocycles derived from diphenylamine-2,2'-dicarboxaldehyde 38

CHAPTER 2 IMMOBILIZATION OF NICKEL(II) COMPLEXES CONTAINING N_4-SCHIFF BASE MACROCYCLES ON N-DOPED GRAPHENE FOR ELECTROCHEMICAL CO_2 REDUCTION 41

2.1 Materials and method 41

2.2 Instrumentation 42

2.3 Electrochemical measurements 42

2.3.1 Electrochemical measurements in non-aqueous electrolyte 42

2.3.2 Electrochemical measurements in aqueous electrolyte 43

2.4 Synthetic Procedure for nickel(II) complexes containing N_4-Schiff base macrocycles 46

2.4.1 Synthesis of 2,2'-iminobis(methyl benzoate) 46

2.4.2 Synthesis of 2,2'-iminobis(hydroxymethyl benzene) 47

2.4.3 Synthesis of diphenylamine-2,2'-dicarboxaldehyde 48

2.4.4 Preparation of N_4-Schiff base nickel(II) complexes 48

2.4.4.1 Preparation of [1-Ni](BF_4) 48

2.4.4.2 Preparation of [2-Ni](BF_4) 49

2.4.4.3 Preparation of [2-Ni]^{Me}(BF_4) 50

2.4.5 Preparation of Ni@NG hybrid catalysts 50

2.4.6 Preparation of catalyst ink and fabrication of electrode 50

2.4.7 Determination of Ni content in hybrid catalysts 51

2.5 Structural comparison of the N_4-Schiff base nickel complexes 51

2.6 Electrochemical studies of nickel complexes in NBu_4PF_6/CH_3CN 55

จุฬาลงกรณ์มหาวิทยาลัย
Chulalongkorn University

2.7 Immobilization of nickel complexes onto N-doped graphene 62

2.8 Electrochemical studies of Ni@NG catalysts in aqueous electrolyte 63

2.8.1 Controlled potential electrolysis (CPE) 64

2.8.2 KSCN poisoning experiment – elucidation of active site for ECR 66

2.8.3 Comparison studies of ECR 68

2.8.4 Prolonged electrolysis – the stability performance 71

CHAPTER 3 AN UNEXPECTED FORMATION OF PENTADENTATE NICKEL(II) COMPLEXES BEARING ACRIDINE-BASED SCHIFF-BASE LIGAND THROUGH THE REARRANGEMENT OF DIPHENYLAMINE 76

3.1 Materials and Reagents 77

3.2 Instrumentation 77

3.3 Synthesis of acridine-based Schiff-base Ni(II) complexes 78

3.3.1 Synthesis of $[NiL^{ACR}](BF_4)_2$ 78

3.3.2 Synthesis of $[NiL^{ACR}](ClO_4)_2$ 78

3.4 X-ray crystallography 79

3.5 Structural descriptions and properties of acridine-based nickel(II) complexes .. 80

3.6 Plausible Mechanism of Acridine-Based Complex Formation 85

3.7 UV-visible adsorption profiles of acridine-based nickel(II) complexes 86

3.8 Electronic properties and preliminary observation toward electrocatalytic H_2 production 87

CHAPTER 4 CONCLUSION 92

APPENDIX 94

REFERENCES 128

VITA 139

LIST OF TABLES

Page

Table 1 Standard potentials of CO_2 reduction and H_2 evolution reaction in aqueous solution[20] 20

Table 2 Crystal data and structural refinement for 1-Ni, 2-Ni, and $[2\text{-Ni}]^{Me}$ 53

Table 3 Comparison of selected bond lengths (Å), angles (°) and twist of diphenylamine unit for 1-Ni, 2-Ni and $[2\text{-Ni}]^{Me}$ 54

Table 4 Summarized electrochemical data of N_4-Schiff base nickel macrocycles..... 56

Table 5 Summary of data in bulk electrolysis for 1 h in a CO_2-saturated 0.5 M $NaHCO_3$ solution (pH 7.4) using Ni@NG catalysts at various applied potential. 70

Table 6 Summarized catalytic activity of Ni@NG catalysts for ECR at -0.67 V vs. RHE. 74

Table 7 Crystal data and structural refinement for $[NiL^{ACR}](BF_4)_2$ and $[NiL^{ACR}](ClO_4)_2$.. 84

Table 8 Summarized data for electrochemical hydrogen production using $[NiL^{ACR}](BF_4)_2$ 91

จุฬาลงกรณ์มหาวิทยาลัย
CHULALONGKORN UNIVERSITY

LIST OF FIGURES

Page

Figure 1 Global CO_2 emission by sector and per capita between 1990-2021 (in Gt unit).[3] 16

Figure 2 (a) Overview of the possible routes for CO_2 conversion. (b) Schematic illustration of photochemical CO_2 reduction. [20] 19

Figure 3 (a) Schematic illustration of CO_2 electrolyzer (b) Development aspects for electrochemical CO_2 reduction.[25] 21

Figure 4 Reaction pathways of electrochemical CO_2 reduction (ECR) over catalytic surfaces.[24] 22

Figure 5 (a) Modes of CO_2 coordination via the single metal center. (b) CO_2 insertion into metal hydride (M-H) species.[26] 24

Figure 6 Proposed mechanism for electrochemical reduction of CO_2 catalyzed by $[Ni(cyclam)]^{2+}$ complex.[26, 35] 26

Figure 7 Molecular structure of bio-inspired cyclam-based nickel complexes.[39] 27

Figure 8 (a) Molecular structure of $[Ni(isocyclam)]^{2+}$ and chalcogenide-containing isocyclam-based nickel complexes. (b) Cyclic voltammograms of Ni-L^N, Ni-L^O, Ni-L^S and Ni-L^{Se} in 0.1 M Bu_4NPF_6/CH_3CN at 0.1 V/s. (c) Linear sweep voltammograms of Ni-L^N, Ni-L^O, Ni-L^S and Ni-L^{Se} in CO_2-saturated CH_3CN:H_2O (4:1) with 0.1 M Bu_4NPF_6.[38] 27

Figure 9 (a) Imine-functionalized nickel macrocycles for CO_2-to-oxalate reduction (b) Cyclic voltammograms of $[Co^{III}N_4H(Br)_2]^+$ in CH_3CN (black), with CO_2 (red), and with CO_2 and H_2O (blue). (c) Plausible outline for CO_2 involving putative $[CoN_4H]$. (d) Stepwise modification of PDI ligand through extended conjugation, electron-withdrawing effect and electrostatic effects.[43] 29

Figure 10 (a) Active site of [NiFe] carbon monoxide dehydrogenase (CODH) represented in ball-stick model.[46] (b) Proposed reaction mechanism of CO_2-to-CO reduction by [NiFe]-CODH.[50] 31

จุฬาลงกรณ์มหาวิทยาลัย
Chulalongkorn University

Figure 11 (a) Isomeric structure of positional amide-functionalized iron porphyrins.[52] (b) Catalytic current response and Tafel plots for amide-functionalized iron porphyrins.[52] (c) Effect of pK_a in CO_2 reduction using iron hangman porphyrins.[54] 34

Figure 12 Merging concept of organocatalysis and electrocatalysis for enhancing activity and tuning selectivity.[57] 35

Figure 13 (a) Immobilization of MTPP onto carbon nanotube (CNT) and carbon black (CB) using simple sonication method.[66] (b) Steric modification of cobalt phthalocyanine (CoPc) for suppressing aggregation.[70] 37

Figure 14 (a) Non-heme Fe complexes with in-plane N_4 dicarboxamide ligand and catalytic performance toward CO_2-to-CO reduction.[71] (b) Pyrene-functionalized $Ni(cyclam)^{2+}$ and its faradaic efficiency of CO production at various potential.[72] 37

Figure 15 Chemical structures of diphenylamine-2,2'-dicarboxaldehyde and nickel complexes used in this study. 39

Figure 16 Schematic illustration of one-compartment electrochemical cell for electrochemical measurements in non-aqueous electrolyte 45

Figure 17 Schematic illustration of two-compartment H-shaped electrochemical cell for electrochemical measurements in aqueous electrolyte. 46

Figure 18 Perspective views of cationic complexes (a) 1-Ni, (b) 2-Ni, and (c) $[2\text{-Ni}]^{Me}$, showing the coordination environment of the nickel(II) atom. Anions and hydrogen atoms are omitted for clarity. The X-ray structure of 1-Ni and 2-Ni was obtained from ref. 76 and 75 53

Figure 19 CVs of 1 mM (a) 1-Ni, (b) 2-Ni and (c) $[2\text{-Ni}]^{Me}$ recorded in N_2-saturated CH_3CN/ 0.1 M NBu_4PF_6/CH_3CN solution (**V** = 0.1 V/s, glassy carbon electrode: A = 0.071 cm^2). 55

Figure 20 CVs of 1-Ni in CH_3CN at different scan rate and plots of reductive current vs. the square root of the scan rate of 1-Ni in CH_3CN at E = -1.86 V vs. $Fc^{+/0}$. 57

Figure 21 CVs of 2-Ni in CH_3CN at different scan rate and plots of reductive and oxidative currents vs. the square root of the scan rate of 2-Ni in CH_3CN at E = -1.72 V vs. $Fc^{+/0}$. 57

Figure 22 CVs of $[2\text{-Ni}]^{Me}$ in CH_3CN at different scan rate and plots of reductive and oxidative currents vs. the square root of the scan rate of $[2\text{-Ni}]^{Me}$ in CH_3CN at E = -1.52 V vs. $Fc^{+/0}$..... 58

Figure 23 Cyclic voltammograms of (a) 1-Ni, (b) 2-Ni, and (c) $[2\text{-Ni}]^{Me}$ at 1 mM concentration in 0.1 M NBu_4PF_6/CH_3CN (**ν** = 0.1 V/s) under N_2 (blue); under CO_2 without 1 M H_2O (red), and with 1 M H_2O (green). Background signals under CO_2 were collected and illustrated in black dashed line. Carbon paper (A = 1 cm^2) was used as working electrode. 61

Figure 24 (a) Cyclic voltammograms of carbon paper (black trace) and NG (blue trace) under CO_2-saturated condition, and 1-Ni@NG under N_2- (red dotted line) and CO_2-saturated condition (red trace) recorded in 0.5 M $NaHCO_3$ solution at the scan rate of 0.05 V/s. (b) Current-time responses for controlled potential electrolysis at -0.67 V vs. RHE for 1 h using carbon paper, NG, and 1-Ni@NG in N_2- and CO_2-containing 0.5 M $NaHCO_3$. (c) Faradaic efficiencies of CO and H_2 and (d) Quantitative analysis of gas products for controlled potential electrolysis for 1 h at -0.67 V vs. RHE in N_2- and CO_2-saturated 0.5 M $NaHCO_3$ solution. Note: CP stands for carbon paper (TGP-H-60) and NG is an abbreviation of nitrogen-doped graphene. 65

Figure 25 KSCN poisoning experiment. (a) and (c) Cyclic voltammograms of NG and 1-Ni@NG with (red broken line) and without 10 mM KSCN (black solid line) in 0.5 M $NaHCO_3$. (b) and (d) Current-time profiles of NG and 1-Ni@NG with (red dotted line) and without 10 mM KSCN (black dotted line) in 0.5 M $NaHCO_3$. (e) Electrochemical setup for KSCN poison experiment. 67

Figure 26 Faradaic efficiencies of (a) CO and (b) H_2, and specific current density of (c) CO production and (d) H_2 evolution at various applied potential from -0.57 V to -0.87 V vs. RHE for 1h-bulk electrolysis in CO_2-saturated 0.5 M $NaHCO_3$..... 71

Figure 27 Current-density time profiles and faradaic efficiencies of CO (blue) and H_2 (red) evolution in controlled potential electrolysis at -0.67 V vs. RHE in CO_2-saturated 0.5 M $NaHCO_3$ using (a) 1-Ni@NG, (c) 2-Ni@NG and (e) $[2\text{-Ni}]^{Me}$@NG. Time courses of the moles of CO (blue) and H_2 (red) production from bulk electrolysis and theoretical product yields (black) calculated from $e^-/2$ of charge required during the bulk electrolysis for (b) 1-Ni@NG, (d) 2-Ni@NG and (f) $[2\text{-Ni}]^{Me}$@NG. 75

Figure 28 (a) Structural motif of diphenylamine-2,2'-dicarboxaldehyde, and (b) acridine-based cobalt (II) complexes rearranged from diphenylamine-based precursor.[94] (c) Nickel (II) complexes bearing Schiff-base acridine-based ligand in this work. 80

Figure 29 Thermogravimetric analysis curve of $[NiL^{ACR}](BF_4)_2$ 81

Figure 30 ORTEP diagram of $[NiL^{ACR}]^{2+}$ showing the coordination environment for nickel(II) atom. The atoms are represented by 50% probability thermal ellipsoids. 82

Figure 31 Perspective views of the one-dimensional column structures forming by the complementary hydrogen bonding and **π-π** stacking interactions in (a) $[NiL^{ACR}](BF_4)_2$ and (b) $[NiL^{ACR}](ClO_4)_2$. 83

Figure 32 Plausible mechanism of nickel-mediated acridine-based ligand formation 86

Figure 33 UV-vis spectroscopic characterization of 0.1 mM $[NiL^{ACR}](BF_4)_2$ (red trace) $[NiL^{ACR}](ClO_4)_2$ (black trace), and 2,2'-dpadc in acetonitrile solution (dashed blue trace). 87

Figure 34 (a) CVs of $[NiL^{ACR}](BF_4)_2$ in N_2-saturated 0.1 M NBu_4PF_6/DMF at scan rate of 0.1 V/s and (b) at different scan rate. Ferrocene (Fc) was used as internal redox standard ($E_{1/2}$ = 0.09 V ± 0.01 V vs. 0.01 M $AgNO_3$/Ag). 88

Figure 35 CVs of (a) $[NiL^{ACR}](BF_4)_2$ and (b) blank in N_2-saturated 0.1 M NBu_4PF_6/DMF in the presence of 0-30 mM CH_3COOH. 88

Figure 36 CVs of $[NiL^{ACR}](BF_4)_2$ in N_2-saturated 0.1 M NBu_4PF_6/DMF in the presence of CH_3COOH (red trace) and after rinse test (blue trace) and blank signal (dashed line) 89

Figure 37 Charge build-up profiles during bulk electrocatalysis for 1 h at -2.1 V (broken line) and -2.3 V vs. $Fc^{+/0}$ (solid line)..... 91

จุฬาลงกรณ์มหาวิทยาลัย
CHULALONGKORN UNIVERSITY

CHAPTER 1

INTRODUCTION AND THESIS OBJECTIVES

1.1 Rising of atmospheric CO_2 level

Over the past decades, rapid economic growth has contributed to increasing energy demand. An apparent result of this rapid change is a rise in fossil fuel consumption (such as coal, oil, and natural gas) which have emerged as primary energy sources since the industrial revolution. Carbon dioxide (CO_2) accounts for a major emission of greenhouse gas which has been related to various anthropogenic activities: combustion of non-renewable resources and transportation.[1, 2] According to the emission database for global atmospheric research (EDGAR), global emission of CO_2 have progressively increased from 15.9 Gt in 1970 to a total of 37.9 Gt in 2021 with an overall increase by about 58% between 1990 and 2021 (**Figure 1**).[3] In recognition of the adverse effects that fossil fuels have an impact on the global environment with respect to the emission of CO_2, their pervasive use has given rise to considerable environmental concerns. The mitigation of atmospheric CO_2 concentration in the environmental system is of paramount importance as being largely responsible for threatening the global climate patterns. Therefore, enormous efforts in transforming and utilizing CO_2 as chemical feedstock to produce chemical commodities have increasingly caught attention in the scientific community.

จุฬาลงกรณ์มหาวิทยาลัย
Chulalongkorn University

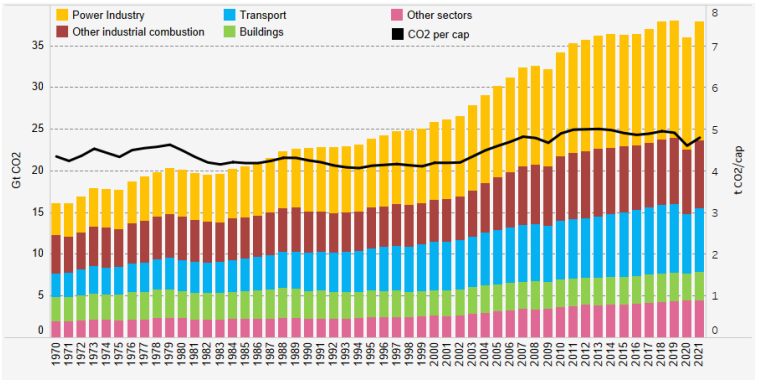

Figure 1 Global CO_2 emission by sector and per capita between 1990-2021 (in Gt unit).[3]

1.2 CO_2 transformation and utilization

The utilization and transformation of CO_2 has nowadays received attention since it offers potential benefits in generation of high-value chemicals and allows reduction of its emission into the atmosphere. It is well known that CO_2 is a highly stable molecule with lower Gibb's free energy (ΔG°_{f} = -394 kJ/mol) compared to its conversion products.[4, 5] That means the conversion of CO_2 will require an amount of energy input from the energetic standpoint. Several chemical approaches have been reviewed and reported for transformation of CO_2 with the different energy inputs – heat, light and electricity.[4, 6-8]

1.2.1 Reverse water-gas shift reaction

$$CO_2 + H_2 \longleftrightarrow CO + H_2O \quad \Delta H^{\circ} = 41.2 \text{ kJ/mol} \quad \textbf{(eq. 1)}$$

Reverse water-gas shift (RWGS) is an equilibrium reaction in which a gas mixture of CO_2 and H_2 was consumed as substrate to produce CO and H_2O (**eq. 1**), being favorable at high temperature (550 – 750 $^{\circ}$C) owing to the endothermic character and low pressure (0 – 5 bar) catalytic condition. The RWGS can be regarded as an intermediate reaction in other CO_2 conversion processes such as CO_2 and CO methanation (**eq. 4-5**). Common RWGS catalysts can be Cu-based and noble metals supported on metal oxides,[9, 10] and transition metal carbides.[11]

จุฬาลงกรณ์มหาวิทยาลัย
Chulalongkorn University

1.2.2 Direct CO_2-to-methanol conversion

$$CO_2 + 3H_2 \longrightarrow CH_3OH + H_2O \quad \Delta H^{\circ} = -49.5 \text{ kJ/mol} \quad \textbf{(eq. 2)}$$

$$CO + 2H_2 \longrightarrow CH_3OH \quad \Delta H^{\circ} = -90.6 \text{ kJ/mol} \quad \textbf{(eq. 3)}$$

Methanol is one of ubiquitous chemicals that is widely used for chemical productions and fuels.[12, 13] One of possible routes to produce CH_3OH from CO_2 is the hydrogenation of CO_2 (**eq. 2**). Alternatively, methanol synthesis can be carried out *via* dry reforming of CH_4 (**eq. 6**) followed by the hydrogenation of CO (**eq. 3**). Taking consideration of enthalpy, the direct CO_2-to-CH_3OH conversion is very exothermic and favorable at the low-temperature and high-pressure condition.

1.2.3 CO_2 methanation (Sabatier reaction)

$$CO_2 + 4H_2 \longleftrightarrow CH_4 + 2H_2O \quad \Delta H^\circ = -165 \text{ kJ/mol} \qquad (\textbf{eq. 4})$$

$$CO + 3H_2 \longleftrightarrow CH_4 + H_2O \quad \Delta H^\circ = -206 \text{ kJ/mol} \qquad (\textbf{eq. 5})$$

The reaction of CO_2 methanation is an old paradigm of CO_2 conversion, which nowadays has been widely known as "Sabatier reaction" due to its discovery by Sabatier and Senderens in 1902. According to the thermodynamic aspect, Sabatier reaction is a highly favorable process as its highly negative enthalpy of formation and Gibb's free energy. Nonetheless, it is kinetically limited as producing CH_4 from CO_2 is an 8-electron transfer process. Therefore, Sabatier reaction is usually conducted at elevated temperature (300 – 500 °C). The common catalysts used for CO_2 methanation could be either noble metals (*e.g.*, Rh- and Ru-based catalysts) or non-noble metals (*e.g.*, Ni).[14-17]

1.2.4 Dry reforming of CH_4 (DRM)

$$CO_2 + CH_4 \longrightarrow 2CO + 2H_2 \quad \Delta H^\circ = 248 \text{ kJ/mol} \qquad (\textbf{eq. 6})$$

Dry reforming involves CO_2 and hydrocarbon natural gas, commonly methane (CH_4), to produce syngas ($CO + H_2$). From thermodynamic point of view, dry reforming of methane is a strongly endothermic process, requiring the high-temperature and pressurized process. The major problem of dry reforming is a coke or carbon deposition on the surface of catalysts, causing catalyst deactivation.[18, 19] These multiple challenges of dry reforming restrict the implementation on the industrial level. Alternative routes of dry reforming of methane exist as bi-reforming (**eq. 7**) and oxy-CO_2 reforming of methane (**eq. 8**).[19]

$$3CH_4 + CO_2 + 2H_2O \longrightarrow 4CO + 8H_2 \qquad (\textbf{eq. 7})$$

$$3CH_4 + CO_2 + O_2 \longrightarrow 4CO + 6H_2 \qquad (\textbf{eq. 8})$$

จุฬาลงกรณ์มหาวิทยาลัย
Chulalongkorn University

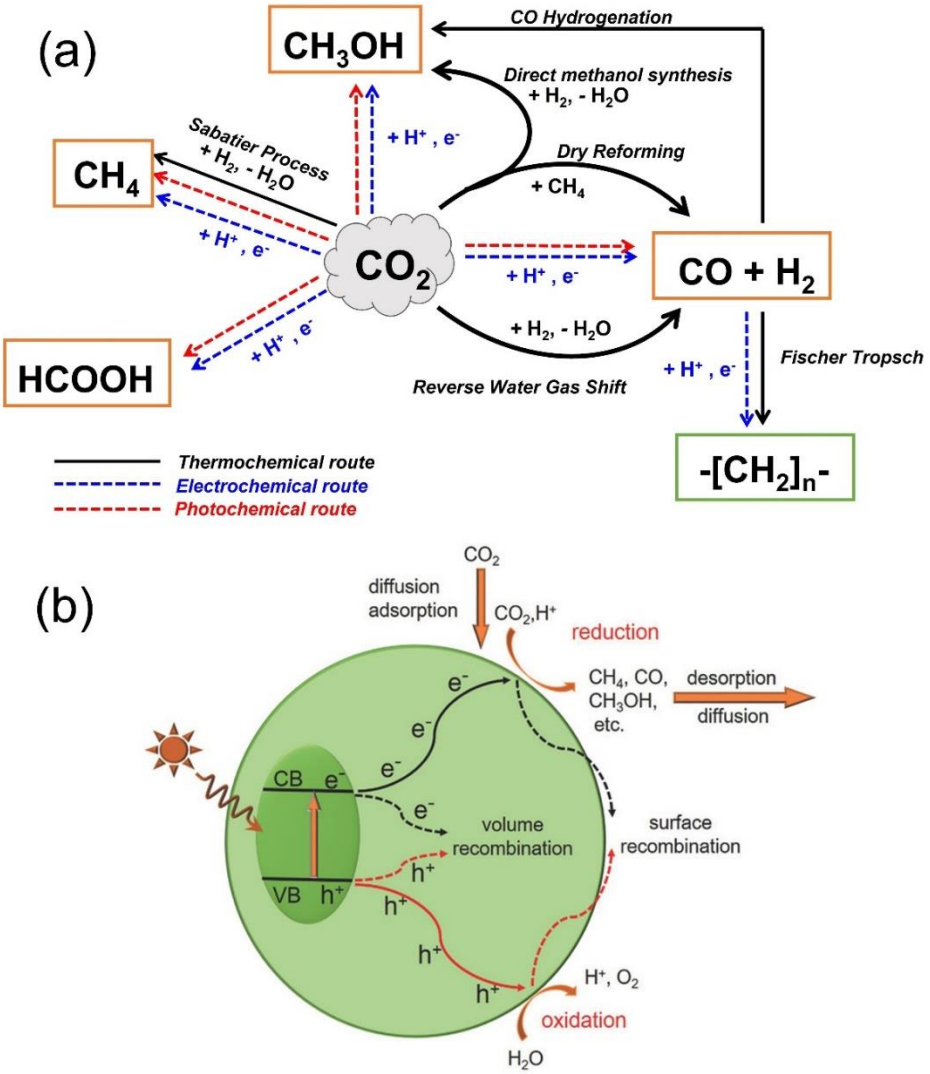

ศูนย์วิทยทรัพยากร
CHULALONGKORN UNIVERSITY

Figure 2 (a) Overview of the possible routes for CO_2 conversion. (b) Schematic illustration of photochemical CO_2 reduction. [20]

1.2.5 Photochemical CO_2 reduction

$$CO_2 + bH_2O + h\underline{\nu} \longrightarrow 2C_xH_yO_z + O_2 \qquad \textbf{(eq. 9)}$$

Photochemical CO_2 reduction represents a promising alternative route of CO_2 conversion as the process of which mimics natural photosynthesis (**eq. 9**).[20] The objective of this approach is to utilize sunlight as an economic and sustainable energy source to convert atmospheric CO_2 into valuable chemicals. The photochemical CO_2 reduction is mediated by photocatalysts that harvest light and

transform the energy to activate CO_2. The overall process of photochemical CO_2 reduction is briefly described as follows (**Figure 2b**): (1) light (or photon) adsorption to generate excited electrons in valence band and holes in conduction band (2) Photogenerated electron-hole separation and transportation (3) CO_2 adsorption and activation over the surface of photocatalysts (4) CO_2 reduction to hydrocarbons and water oxidation (5) Product desorption from the surface of photocatalysts.

1.3 Electrochemical CO_2 reduction

Table 1 Standard potentials of CO_2 reduction and H_2 evolution reaction in aqueous solution[20]

Half reaction	E^0 (V vs. NHE, *pH = 7*)
Electrochemical CO_2 reduction (CO_2RR)	
$CO_2 + e^- \rightarrow CO_2^{\bullet-}$	-1.90
$CO_2 + 2H^+ + 2e^- \rightarrow CO + H_2O$	-0.52
$CO_2 + 2H^+ + 2e^- \rightarrow HCOOH + H_2O$	-0.61
$CO_2 + 4H^+ + 4e^- \rightarrow HCHO + H_2O$	-0.51
$CO_2 + 6H^+ + 6e^- \rightarrow CH_3OH + H_2O$	-0.38
$CO_2 + 8H^+ + 8e^- \rightarrow CH_4 + 2H_2O$	-0.24
$2CO_2 + 12H^+ + 12e^- \rightarrow C_2H_4 + 4H_2O$	-0.34
Electrochemical H_2 evolution reaction (HER)	
$2H^+ + 2e^- \rightarrow H_2$	-0.41

จุฬาลงกรณ์มหาวิทยาลัย
CHULALONGKORN UNIVERSITY

Electrochemical CO_2 reduction (ECR) is envisioned as a promising approach for utilizing and transforming CO_2 into value-added chemicals, which can be carried out by applying electrical input at the regulated potential. The key component for this approach is to incorporate cathode catalysts for CO_2 reduction and anode catalysts for H_2O oxidation in the CO_2 electrolyzers (**Figure 3a**). From the energetic viewpoint, the thermodynamic stability of CO_2 causes difficulty in the activation of CO_2, requiring

the large external driving force to initiate the process. Indeed, ECR required a high applied bias to commence the single-electron reduction of linear CO_2 molecule into bent-shaped $CO_2^{\bullet-}$ radical anion (E^0 = -1.90 V *vs.* NHE) or to experience a PCET process, producing various hydrocarbon products.[21-24] For practical application of ECR, the CO_2 electrolyzer has to be operated under high current densities, high faradaic efficiencies and high energetic efficiencies. Therefore, several ECR development aspects have drawn attention amongst the scientific and engineering community. These advancements include catalyst design, reactor design and mechanistic insight of ECR (**Figure 3b**).[25]

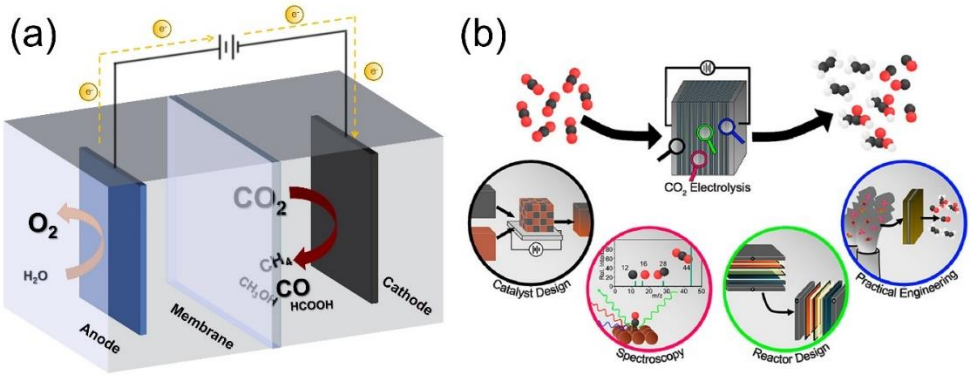

Figure 3 (a) Schematic illustration of CO_2 electrolyzer (b) Development aspects for electrochemical CO_2 reduction.[25]

จุฬาลงกรณ์มหาวิทยาลัย
Chulalongkorn University

1.4 Chemistry of carbon dioxide and its reduction mechanism with catalytic metal centers

CO_2 is a 16-electron linear molecule in electronic ground state, of which symmetry belongs to $D_{\infty h}$ group. Despite overall neutral charge and thermodynamic stability of CO_2 molecules, some chemical reactivities are anticipated for CO_2 molecule thanks to an electrophilic site on the carbon center and nucleophilic sites on the oxygen atoms. Its electronic structure is presented by $O^{\delta-}$–$C^{\delta+}$–$O^{\delta-}$. With this polarization, CO_2 molecules are susceptible to being attacked by nucleophiles at the carbon centers and subjected to reduction. Thus, the utilization of transition metal

electrocatalysts to mediate the electrochemical reduction is one of promising approaches for CO_2 conversion.

To regulate the ECR at sufficiently high current density, product selectivity and energy efficiency, a comprehension regarding the process by which CO_2 is reduced at an electrode is necessary. Typically, the initial step in reduction of CO_2 involves the activation of CO_2, manifesting the bending of molecule and interacting with nucleophiles or electrophiles through its frontier orbitals. In ECR, activated CO_2 molecules will interact with the active form of electrocatalyst, and the products are relied on the numbers of electrons and protons involved in the specific reaction (**Table 1** and **Figure 4**).[21-24]

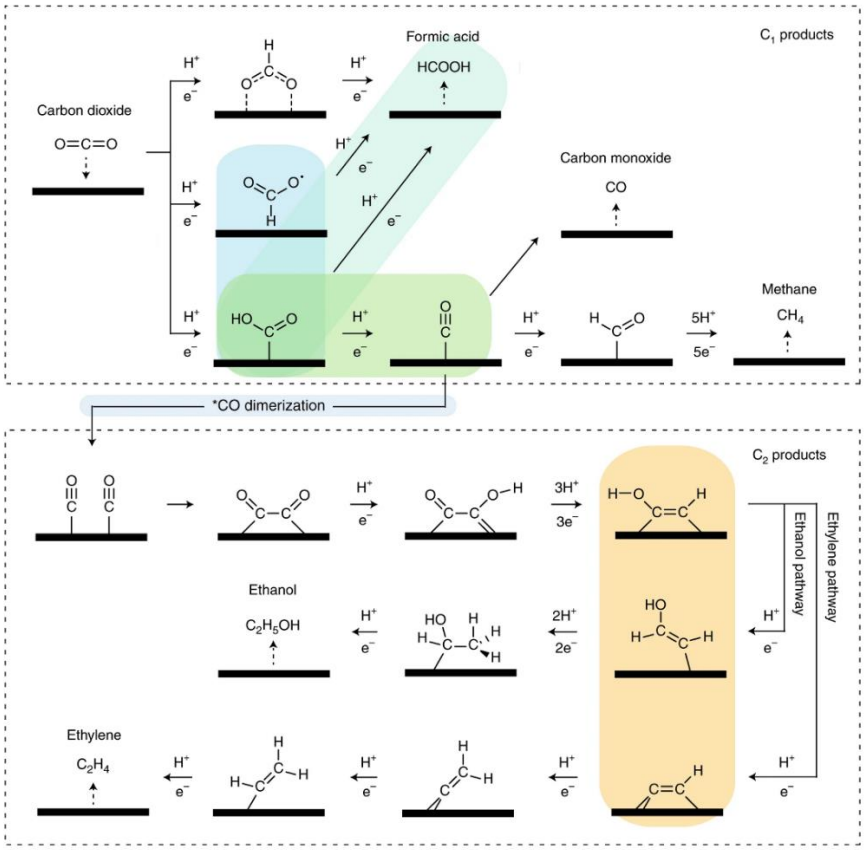

Figure 4 Reaction pathways of electrochemical CO_2 reduction (ECR) over catalytic surfaces.[24]

To obtain 2-electron transfer ECR products, it is well understood that the most likely first ECR intermediate is *COOH and *OCHO (* refers to binding site) for CO and HCOOH production, respectively (**eq. 10 and 11**).[22, 26, 27]

$$* + CO_2 + H^+ + e^- \longrightarrow *COOH \qquad \textbf{(eq. 10)}$$

$$* + CO_2 + H^+ + e^- \longrightarrow *OCHO \qquad \textbf{(eq. 11)}$$

$$* + H^+ + 2e^- \longrightarrow *H \qquad \textbf{(eq. 12)}$$

The first protonation in ECR could either undergo *via* the generation of *COOH (CO pathways) or *OCOH (HCOOH pathways) intermediates, which could be subsequently subjected to the reduction to produce C_1 products, *e.g.*, CO, HCOOH, CHO, CH_3OH and CH_4 with respect to the number of electrons involved in the specific reaction.

Two common pathways of CO_2 activation over catalytic metal centers are (1) CO_2 coordination with metal centers (2) CO_2 insertion into metal-hydride (M-H) bond. In the first scenario, CO_2 can be activated *via* binding to the vacant site of metal centers. By means of CO_2 coordination, there are three typical modes (**Figure 5a**) – coordination *via* carbon atoms (η^1-C mode), coordination *via* carbon and one of oxygen atoms (η^2-C, O mode) and coordination *via* oxygen atoms (η^1-O mode). The binding modes depend on the electron density of metal centers. For example, the η^1-C mode is preferential for electron-rich metal centers, whereas the η^1-O mode is preferred to electron-poor metal centers. An insertion of CO_2 into M-H bond is a route to produce formate ($HCOO^-$) *via* metalloformate intermediate. This activation, unlike coordination, requires the formation of metal hydrides species prior to insertion of CO_2 into M-H bonds (**Figure 5b**). In this aspect, metal centers and ancillary ligands have an impact on the polarity of the M-H bond, which exerts hydride or proton transfer. Typically, hydride ligand holds a fraction of negative charge and is expected to attack electrophilic carbon atom (Path A, hydride transfer). Alternatively, CO_2 can attach to M-H bonds in the other formation, with the oxygen atom bound to the H moiety of metal complex (proton transfer, Path B).

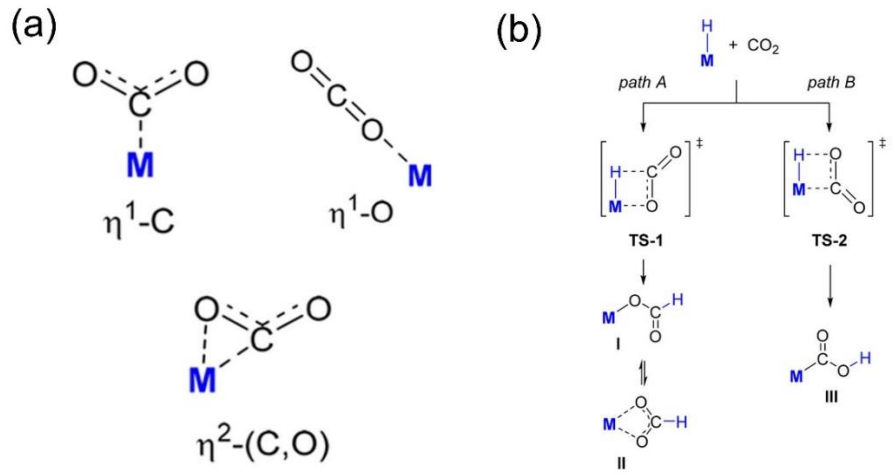

Figure 5 (a) Modes of CO_2 coordination via the single metal center. (b) CO_2 insertion into metal hydride (M-H) species.[26]

To enhance the possibility of obtaining beyond C_1 products, the CO-CO dimerization over the catalytic surface is the necessary step, therefore reducing the activation energy of *CO dimerization will promote the routes for $C_{\geq 2}$ products. In fact, hydrogen evolution reaction (HER) is considered as a competitive reaction for ECR since it is more thermodynamically favorable. HER prefers to take places with metal atoms which strongly interact to *H, as reflected by the less positive value of the Gibbs free energy changes (**Δ**G) for *H intermediates compared to that of *COOH/*OCOH intermediates. Therefore, the first proton transfer dictate whether HER or ECR will be dominant in electrocatalysis.

จุฬาลงกรณ์มหาวิทยาลัย
CHULALONGKORN UNIVERSITY

1.5 Transition metal-based molecular catalysts for ECR

The transition metal-based catalysts can be roughly categorized into two main groups, *i.e.*, molecular, and heterogeneous catalysts. In molecular electrocatalysis, a well-defined active site is regularly proposed, consisting of a metal center surrounded by a particular organic ligand framework. Coordination environments have a huge impact on electronic and steric properties of molecular catalysts, directly influencing their ECR activity. Therefore, a rational catalyst design is

required for elucidating the structure-activity relationship as well as improving the catalytic performance. Recent advances have shown that a variety of nitrogen-based ligands supporting transition-metal molecular catalysts has been reported for efficient and selective ECR such as polypyridyl, phthalocyanine, porphyrin and aza-macrocycle.[28-34]

Amongst them, aza-macrocycle-based catalysts have featured prominently.[35-38] In particular, $[Ni(cyclam)]^{2+}$ (cyclam = 1,4,8,11-tetraazacyclotetradecan) has received widespread attention since it was reported in 1986 as an ECR electrocatalyst platform by Beley and co-workers.[35] In that work, $[Ni(cyclam)]^{2+}$ exhibited the excellent catalytic behavior for selective reduction of CO_2 to CO on the mercury electrode. However, it has been shown that the catalytically active species: $[Ni(cyclam)]^{+}$ is absorbed on the surface of mercury electrode. Thereby, this limitation restricts broader application and environmentally friendly approach. In 2012, Froelich and Kubiak reported that $[Ni(cyclam)]^{2+}$ was shown to homogeneously catalyze ECR at the glassy carbon electrode.[36] Three nickel cyclam complexes with different numbers of methyl substitution were examined. The ECR reactivity was found to be diminished with the methyl substitution on cyclam ligands. This may confer the importance of N-H functionality on supporting ligands, forming hydrogen-bonding interaction to bound CO_2 molecules (**Figure 6**).

จุฬาลงกรณ์มหาวิทยาลัย
Chulalongkorn University

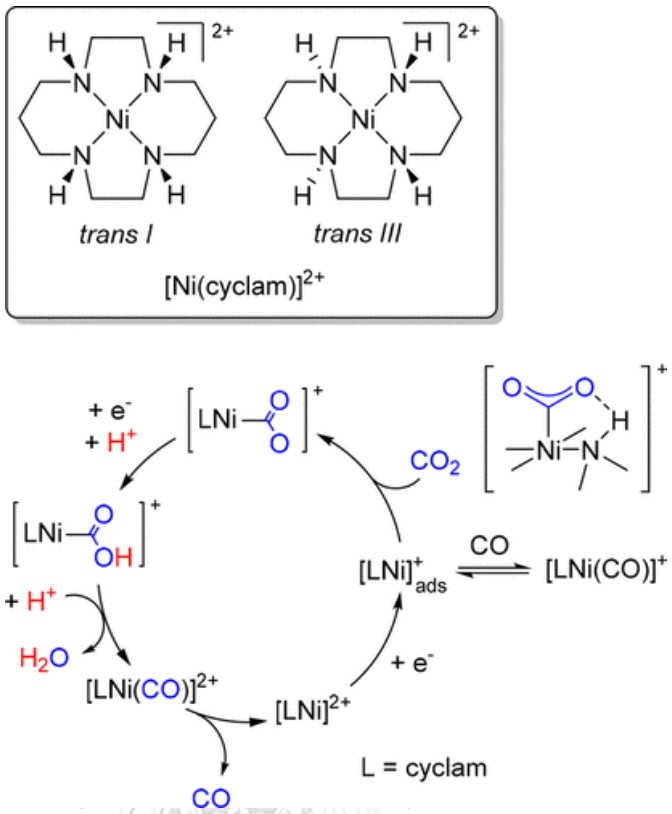

Figure 6 Proposed mechanism for electrochemical reduction of CO_2 catalyzed by $[Ni(cyclam)]^{2+}$ complex.[26, 35]

In 2018, Cao and co-workers developed cyclam-based nickel catalysts inspired by [NiFe]-containing carbon monoxide dehydrogenase ([NiFe]-CODH), through a dinuclear metal synergistic catalysis (DMSC) effect.[39] The molecular structures of nickel catalysts are shown in **Figure 7**. Structurally, **1** possesses the suitable separation between two catalytic nickel centers, *i.e.*, $[Ni(cyclam)]^{2+}$, for the generation of DMSC effect, whereas **2** with mononuclear $[Ni(cyclam)]^{2+}$ complex and **3** with farther separation were synthesized for comparison. The beneficial effect of DMSC in **1** is reflected by the excellent faradaic efficiency of CO production (FE_{CO}) of 95% and TOF of 190 s^{-1} which is approximately 40-fold higher than that of **2** and **3**. This study shed the light of judicious design of molecular catalysts and is of importance to achieve excellent catalytic behavior.

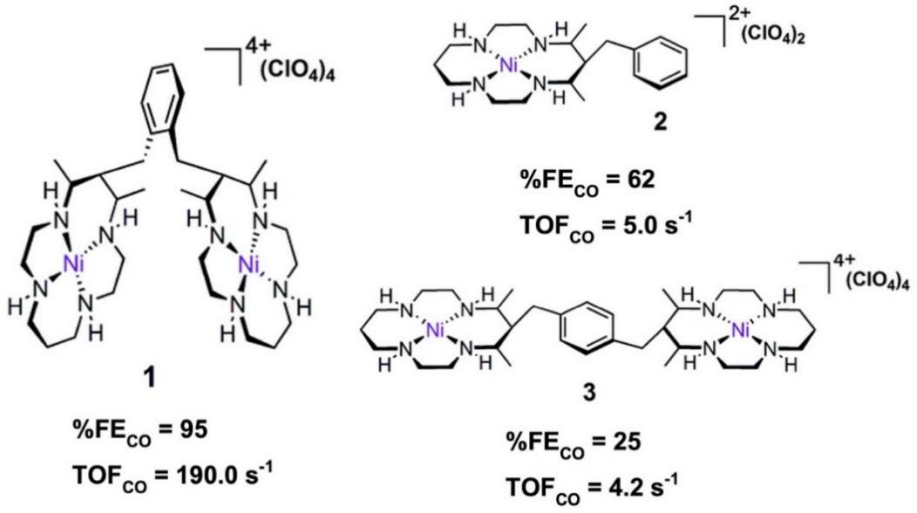

Figure 7 Molecular structure of bio-inspired cyclam-based nickel complexes.[39]

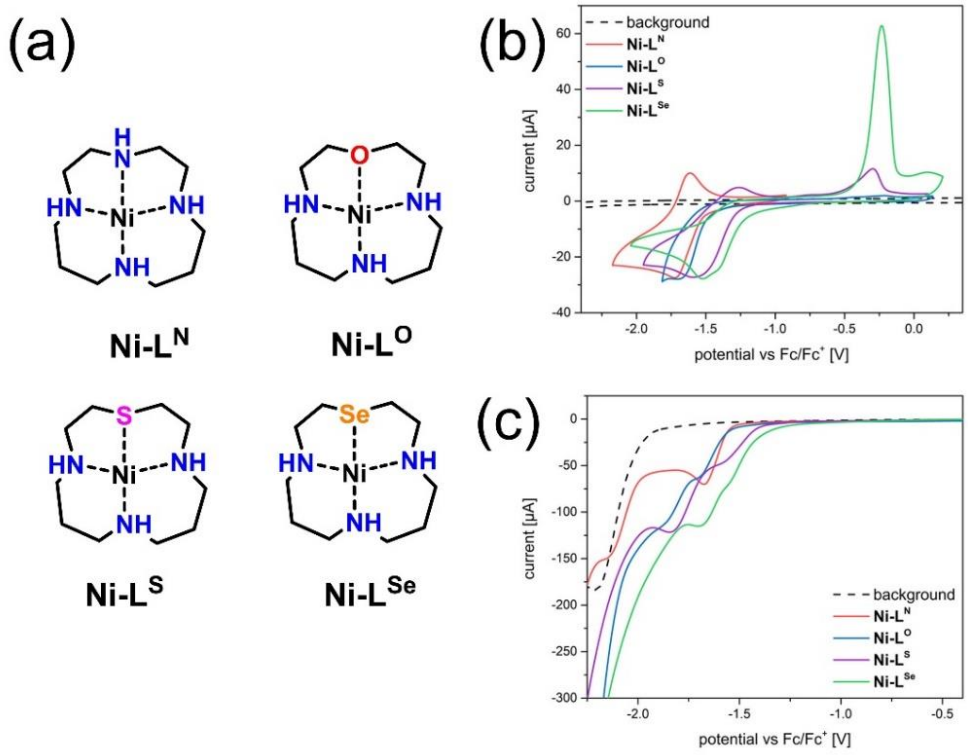

Figure 8 (a) Molecular structure of $[Ni(isocyclam)]^{2+}$ and chalcogenide-containing isocyclam-based nickel complexes. (b) Cyclic voltammograms of Ni-L^N, Ni-L^O, Ni-L^S and Ni-L^{Se} in 0.1 M Bu_4NPF_6/CH_3CN at 0.1 V/s. (c) Linear sweep voltammograms of Ni-L^N, Ni-L^O, Ni-L^S and Ni-L^{Se} in CO_2-saturated CH_3CN:H_2O (4:1) with 0.1 M Bu_4NPF_6.[38]

Along this line, $[Ni(isocyclam)]^{2+}$ (isocyclam = 1,4,7,11-tetraazacylotetradecane) was first investigated toward CO_2-to-CO conversion by Smith and co-workers.[40] It has been found that $[Ni(isocyclam)]^{2+}$ exhibited anodically shifted potential of ca. 160 mV for CO_2 conversion with concomitant lower activity in comparison to $[Ni(cyclam)]^{2+}$. Later, in 2020, Gerschel et. al. modified $[Ni(isocyclam)]^{2+}$ by incorporating the effect of chalcogenide donors.[38] The objective of this study was to investigate the effect of chalcogens in supporting ligands to the electrochemical properties (**Figure 8a**). With increasing electron density of chalcogens, the reduction event of Ni^{II}/Ni^{I} appears at slightly more positive potential (**Figure 8b**). Moreover, the reduction of CO_2 became more feasible at milder potentials of ca. 0.3 V in comparison to $[Ni(isocyclam)]^{2+}$ with nitrogen as a heteroatom, albeit lower in faradaic efficiency for CO_2-to-CO reduction. Importantly, the chalcogen-containing complexes does not behave as homogeneous catalysts but rather act as precursor that produce an electrodeposited catalytically active species as evidenced by scanning transmission electron microscopy (STEM) coupled with energy dispersive X-ray spectroscopy (EDX).

Interestingly, a number of Schiff-base metal complexes have been reported for efficient electrocatalysts for ECR, of which products can be CO, formate, oxalate, etc.[41-45] In 2000, Jäger *et. al.* found that a series of imine-functionalized nickel macrocycles, of which ligand skeleton is similar to cyclam, is capable of catalyzing CO_2-to-oxalate reduction (**Figure 9a**).[41] The complexes with the substituent group of CO_2Et and COMe exhibited the remarkable selectivity with the FE($C_2O_4^{2-}$) up to 90%, and excellent stability as homogeneous ECR catalysts. It was proposed that the catalytic route of CO_2 reduction with these Schiff-base nickel macrocycles follows a dimerization of two $CO_2^{\bullet-}$ radical anions to generate oxalate. In 2014, the cobalt complex with a redox non-innocent pyridyldiimine moiety ($[Co^{III}N_4H(Br)_2]^+$, N_4H = 2,12-dimethyl-3,7,11,17-tetraazabicyclo-[11.3.1]-heptadeca-1(7),2,11,13,15-pentaene) was studied by Peters and co-workers.[42] In the presence of CO_2, cyclic voltammograms of

$[Co^{III}N_4H(Br)_2]^+$ illustrated the substantial current enhancement near the $Co^{I/0}$ redox couple, suggesting that the CO_2 reduction involves the Co^0 species, *i.e.*, $[CoN_4H]$ (**Figure 9b**).

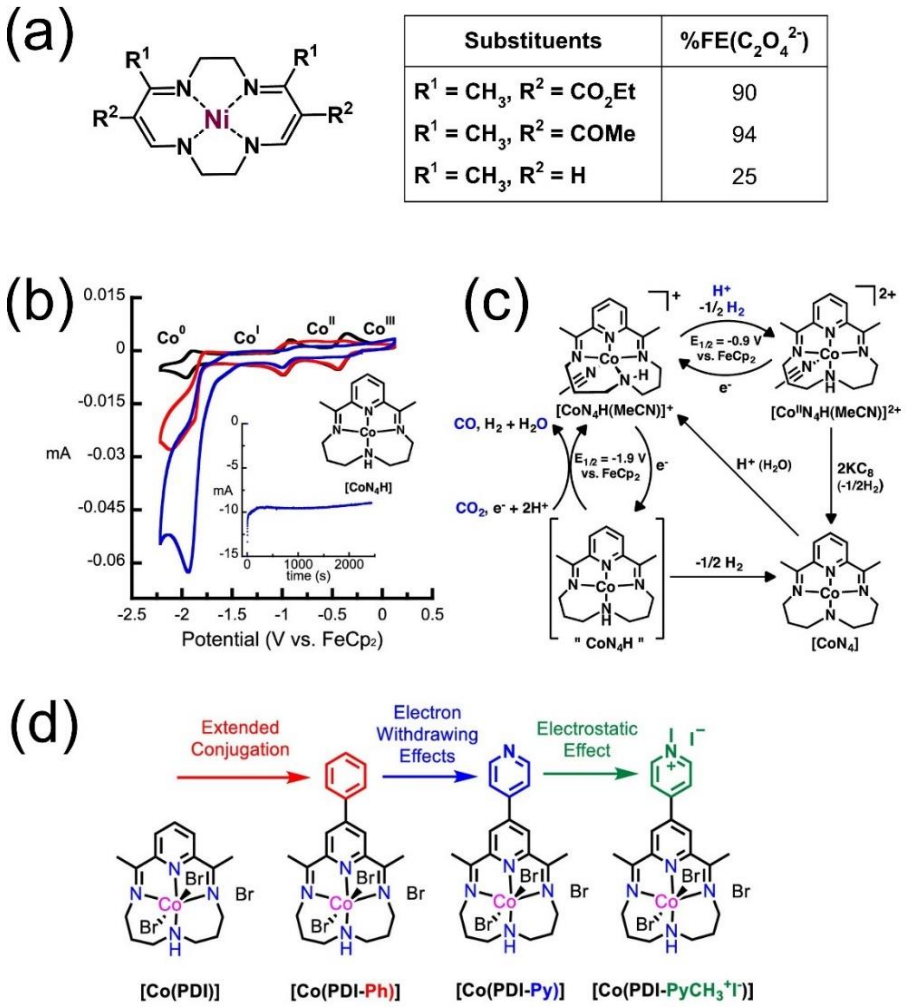

Figure 9 (a) Imine-functionalized nickel macrocycles for CO_2-to-oxalate reduction (b) Cyclic voltammograms of $[Co^{III}N_4H(Br)_2]^+$ in CH_3CN (black), with CO_2 (red), and with CO_2 and H_2O (blue). (c) Plausible outline for CO_2 involving putative $[CoN_4H]$. (d) Stepwise modification of PDI ligand through extended conjugation, electron-withdrawing effect and electrostatic effects.[43]

Owing to the non-innocence of ligand, the electrogenerated [CoN_4H] intermediate is unstable as it can undergo the deleterious side reaction – the loss of bimolecular $H^{\bullet}$ to generate H_2 and [$Co^{I}N_4$] intermediates. However, the stability of [CoN_4H] is adequate to enable CO_2 to be assimilated under electrocatalytic conditions (**Figure 9c**). Later, in 2021, McCrory *et. al.* developed the cobalt pyridyldiimine complex, [Co(PDI)], by modifying substituents on the PDI ligand: extended conjugation, electron-withdrawing and electrostatic effects (**Figure 9d**).[43] The combined three effects of modulations ultimately rendered [Co(PDI-$PyCH_3^+I^-$)] complex, resulted in decreased effective onset potential of *ca.* 0.2 V (E_{onset} = -1.52 V vs. $Fc^{+/0}$) and higher ECR activity (TOF_{cat} of 4.1 x 10^4 s^{-1} when compared to the parent Co(PDI) complex. These outstanding works could demonstrate that Schiff-base metal complexes are potential contenders for ECR electrocatalysts.

1.6 Secondary-sphere effects in electrochemical CO_2 reduction

1.6.1 Enzymatic catalysis of CO_2 reduction

In nature, there are enzymes found in anaerobic bacteria and archaea, which known to catalyze the reversible transformation of CO_2 to CO (*i.e.*, CO dehydrogenase, CODH) and formate (*i.e.*, formate dehydrogenase, FDH).[46, 47] One of attractive CO dehydrogenases is [NiFe]-CODH of which CO_2 reduction reactivity was reported with the turnover frequency (TOF) of up to 45 s^{-1}.[48] The active site of [NiFe]-CODH composes [$NiFe_4S_4$]-cluster (C-cluster) in which the distorted $NiFe_3S_4$ cubane is exogenously linked to the ferrous Fe(II) center holding hydroxyl (**-**OH) ligand at the ready state to react with CO_2.[49] For the reaction mechanism, CO_2 binds to Ni center *via* the C atom and one of carboxylate O atoms bound to the dangling Fe_1 center after depleting the hydroxyl ligand (**Figure 10**). Notably, in this enzymatic catalysis, oxygen atoms from CO_2 have been proposed to get involved in hydrogen-bonding interaction with the N-H groups from lysine and histidine residues.

จุฬาลงกรณ์มหาวิทยาลัย
CHULALONGKORN UNIVERSITY

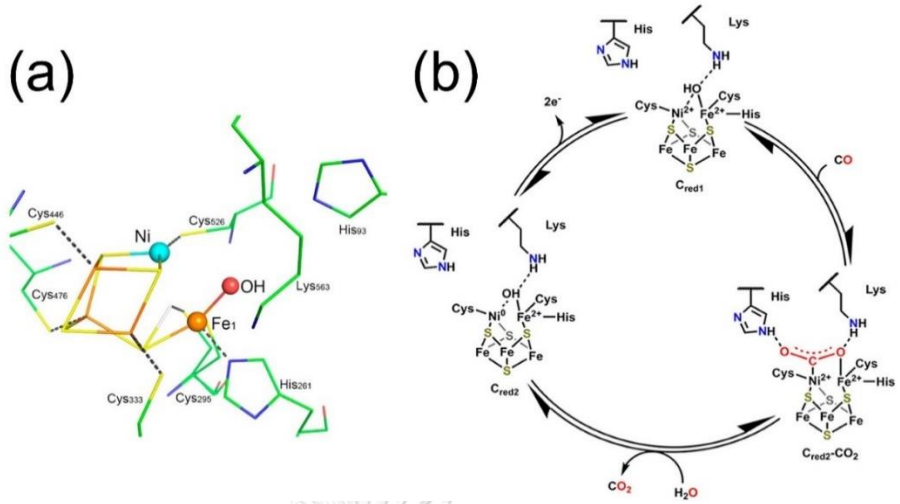

Figure 10 (a) Active site of [NiFe] carbon monoxide dehydrogenase (CODH) represented in ball-stick model.[46] (b) Proposed reaction mechanism of CO_2-to-CO reduction by [NiFe]-CODH.[50]

Lesson from this biological redox system suggests that the key components to design synthesized ECR catalysts is (1) to apply the effect of secondary coordination sphere effect such as hydrogen-bonding interactions and proton relays in CO_2 reduction (2) to involve the bifunctional activation of CO_2 *via* two catalytic metal centers. Therefore, the inspiration to implement hydrogen-bond donor groups proton relay groups (*e.g.*, N-H and O-H) on the ligand frameworks as well as bimetallic active sites has been received attention for improving ECR performance.[50, 51]

1.6.2 Synthetic molecular ECR catalysts based on the secondary sphere effects

So far, the reaction rate and efficiency of CO_2 reduction can be directly improved by the electronic properties of ECR catalysts. This leads to a broad consensus in catalyst design which has largely focused on the modulation of primary coordination environment. Alternatively, the improvement of CO_2 reduction can be carried out by modulating the secondary-sphere coordination. As exemplified by natural bioinorganic system, [NiFe]-CODH employs the secondary-sphere coordination for CO_2 capture and activation (*vide supra*). This bio-inspired model offers an

intriguing approach for the rational design of catalysts by mimicking their chemistry *via* the secondary-sphere effects – to incorporate pendant hydrogen-bond donors, Brønsted acid/base sites, charged residues, and bimetallic metal active sites.[50, 51]

For example, in 2018, Chang and co-workers developed a series of iron tetraphenylporphyrin (Fe-TPP) complexes by introducing amide pendants at various *ortho*- and *para*- positions (**Figure 11a**).[52] All Fe-TPP catalysts showed the catalytic response in cyclic voltammograms under CO_2 and phenol as a proton source but higher for Fe-*ortho*-1-amide and Fe-*ortho*-2-amide (**Figure 11b**).[52] The superior catalytic performances of *ortho*-functionalized positional congeners in terms of current enhancements, faradaic efficiencies and TOF were attributed to the through-space hydrogen-bonding effects. A consequential work of urea-functionalized iron porphyrins also demonstrated that urea pendants can be used to template bicarbonate and resulted in highly boosted catalytic rates.[53] These works could emphasize that the reaction rate and efficiency can be improved with the properly positioned hydrogen-bond donors. In the same year, Nocera *et. al.* found that pK_a of proton donor groups has an important effect to stabilize the intermediates in CO_2 reduction chemistry.[54] In that work, the Fe hangman porphyrins equipped with three different pendant proton relay groups on 2,6-dihydroxylphenyl moiety was investigated their ECR reactivity (**Figure 11c**). Computational studies suggested that intramolecular hydrogen bonding from phenol and guanidium contributes to the stabilization of CO_2 binding within the hangman cleft of 2.1-6.6 kcal/mol. In contrast, the sulfonate counterparts resulted in destabilization of CO_2 adduct due to the deprotonation of sulfonate group which is turned into the electrostatic repulsion.

The implementation of secondary sphere effects is not restricted to the single-point hydrogen-bond stabilization. In fact, CO_2-converting enzymes like [NiFe]-CODH use the multi-point hydrogen-bond interaction for capturing and stabilizing CO_2 adducts. As such features, Aukauloo and co-workers employed the biomimetic model of second-sphere multipoint hydrogen bonding to boost CO_2 reduction. The

Fe porphyrin catalytic units were modified by introducing four urea pendants at *meso*-position.[55] Likewise, they found that such modification facilitates the ECR through remarkably lowering the overpotential of catalysis and increasing the rate of CO_2 binding. Importantly, they also found that the modified Fe porphyrins can capture water molecules within the molecular clefts, and the entrapped water molecules were sufficiently exploited as proton source. Interestingly, Chang and co-workers presented the concept of multifunctional secondary coordination sphere groups by which the Fe porphyrins were decorated with imidazolium pendant units.[56] Since imidazolium hold the positive charge and hydrogen-bond donors in their moieties, the stabilization of CO_2 adducts can be achieved *via* both through-space electrostatic and hydrogen bonding interaction. With this synergistic effect, the-functionalized Fe porphyrins revealed the exceptional rate enhancements of *ca.* 2000-fold higher than the parent Fe-TPP complex.

Besides the direct installation of hydrogen-bond donors onto ligand periphery, the utilization of external additives is a facile and promising development aspect for ECR. Chang *et. al.* developed the merging concept of organo- and electrocatalysis in which $[Ni(cyclam)]^{2+}$ was used as ECR catalysts and bis(aryl)urea additives were introduced as cocatalyst (**Figure 12**).[57] In fact, urea additives contain N-H functionalities in their molecules, which could facilitate the CO_2 activation *via* intermolecular hydrogen-bonding interaction. The estimated TOF of $[Ni(cyclam)]^{2+}$ with urea additives (TOF_{CO} = 460 min^{-1}) is virtually 8-fold higher than that of the absence of additives (TOF_{CO} = 67 min^{-1}), reflecting that homogeneous electrochemical CO_2 reduction could be promoted using hydrogen-bond donor additives. This study offers the starting point for developing electrocatalysts without altering the ligand scaffold and emphasizes the importance of hydrogen-bond stabilization.

จุฬาลงกรณ์มหาวิทยาลัย
Chulalongkorn University

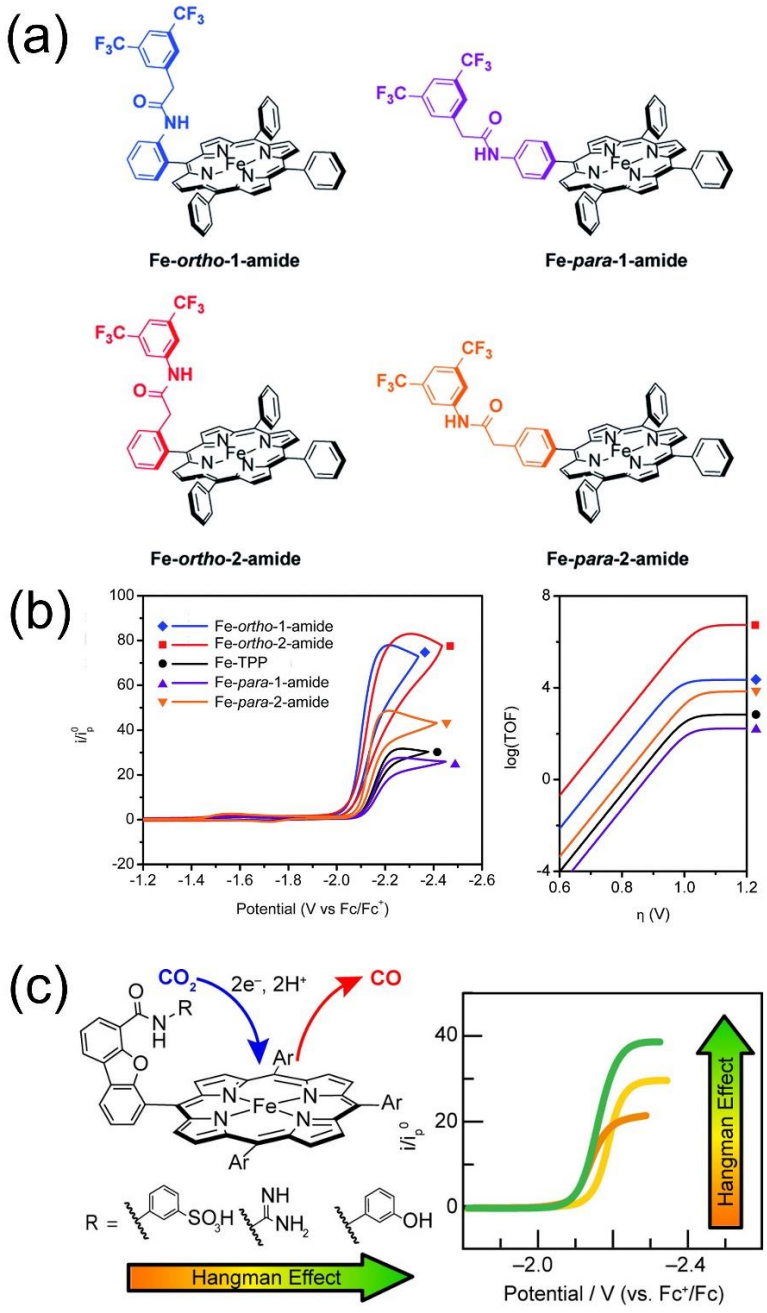

Figure 11 (a) Isomeric structure of positional amide-functionalized iron porphyrins.[52] (b) Catalytic current response and Tafel plots for amide-functionalized iron porphyrins.[52] (c) Effect of pK_a in CO_2 reduction using iron hangman porphyrins.[54]

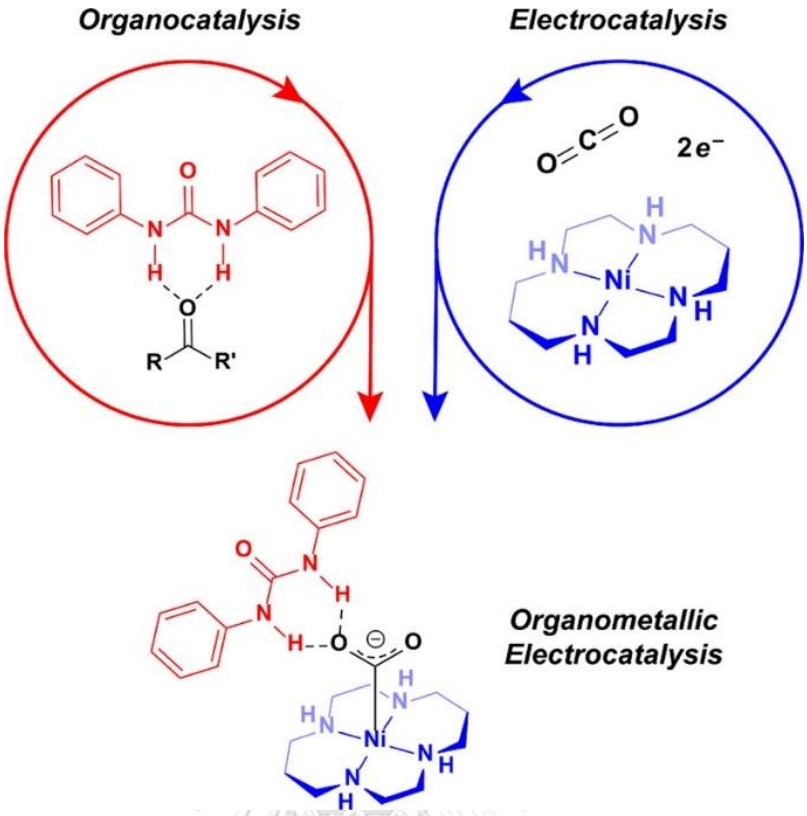

Figure 12 Merging concept of organocatalysis and electrocatalysis for enhancing activity and tuning selectivity.[57]

1.7 Carbon-supported molecular catalysts – trend for modern heterogenous catalysis

Though transition metal complexes manifested excellent efficiency in ECR, they have still been restricted by nonconductive nature in heterogeneous ECR, leading to slow reaction kinetic and low current densities.[58, 59] Hence, to overcome these limitations, later researches have been devoted to molecularly dispersed active sites in which molecular catalysts are deposited onto the solid supports through immobilization, being accomplished by covalent and non-covalent fashion.

Recently, a heterogenization of molecular catalysts onto carbon-based supports have rapidly drawn an attention since it combines the beneficial features of solid materials (*i.e.*, facile product and catalysts isolation, improved conductivity and electron passageway) with those of molecular catalysts (*i.e.*, precisely controlled

coordination environment).[60-65] From the standpoint of heterogenization, it is attainable to execute ECR in heterogenous aqueous environment using water-insoluble molecular catalysts, which could advance sustainable development and practical application. A straightforward and facile heterogenization can be accomplished by exploiting the strategy of non-covalent immobilization by which the molecular catalysts are grafted on carbon supports. The carbon supports can be utilized for the uncomplicated immobilization of molecular catalysts through a straightforward process of sonication, relying on the hydrophobic interaction as the vital interaction (**Figure 13a**).[66-69] By means of this method, highly **π**-conjugated and water-insoluble complexes such as metal tetraphenylporphyrin (MTPP) and metal phthalocyanine (MPc) exhibit a high level of practicality due to their capacity to establish a strong **π-π** stacking interaction with carbon substrates.[61, 67, 69] Nevertheless, planar conjugated molecules may encounter aggregation issues at high concentrations, hindering the accessibility of electrons and substrates to the catalytically active centers.[59, 70] This implies that the catalytic efficiency of these molecules would be impacted by the extent of molecular aggregation on the electrode surface. However, steric modification offers a viable approach to alleviate the problem of catalyst aggregation. Officer and coworkers reported that introducing octa-alkoxy substitution to phthalocyanine ligands can help suppressing the aggregation on chemically converted graphene (CCG) (**Figure 13b**).[70] By introducing the steric modification on ligand scaffold, the octalkoxylated cobalt phthalocyanine on CCG, namely as CoPc-A/CCG, illustrated the improvement of ECR activity with TOF of 5 s^{-1} when compared to that of the unmodified counterpart (TOF of 2 s^{-1}) at the overpotential of 0.48 V *vs.* RHE. The superior activity is reasoned with the lower degree of aggregation, facilitating electron delivery and substrate accessibility to the active catalytic species.

จุฬาลงกรณ์มหาวิทยาลัย
Chulalongkorn University

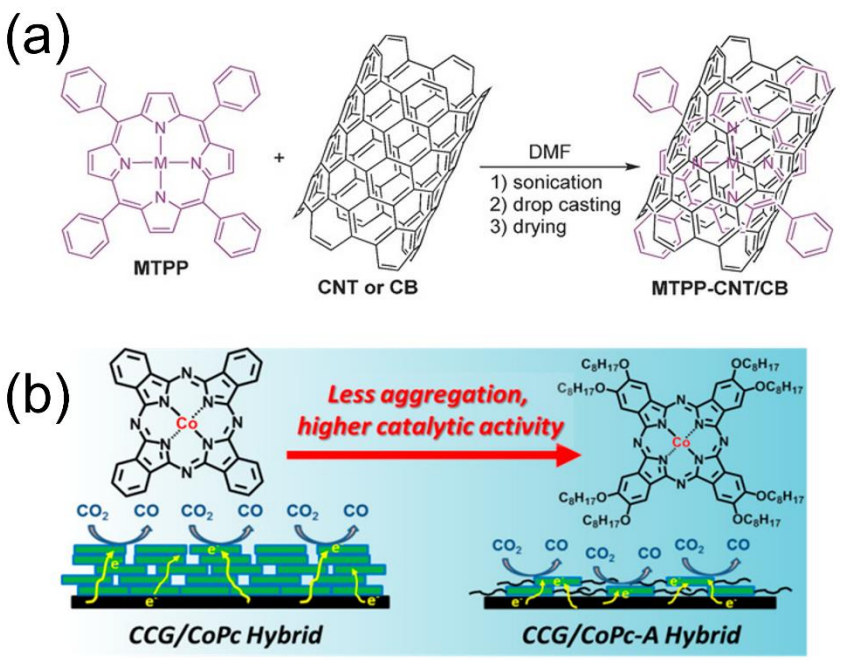

Figure 13 (a) Immobilization of MTPP onto carbon nanotube (CNT) and carbon black (CB) using simple sonication method.[66] (b) Steric modification of cobalt phthalocyanine (CoPc) for suppressing aggregation.[70]

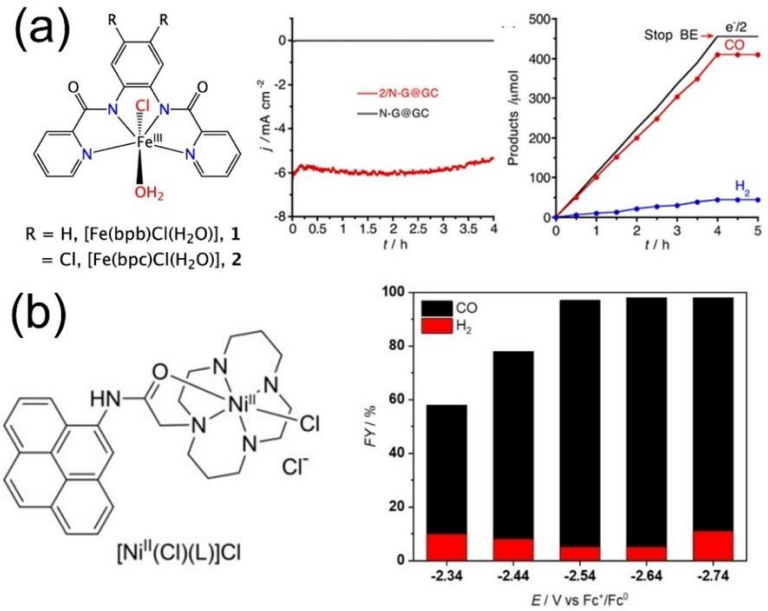

Figure 14 (a) Non-heme Fe complexes with in-plane N_4 dicarboxamide ligand and catalytic performance toward CO_2-to-CO reduction.[71] (b) Pyrene-functionalized Ni(cyclam)$^{2+}$ and its faradaic efficiency of CO production at various potential.[72]

Besides the well-established MTPP and MPc, other macrocyclic complexes have been modified to carbon-supported catalysts such as salen and cyclam ligand.[71-74] In particular, Yagi *et. al.* reported the immobilization of non-heme Fe complexes with tetradentate N_4 dicarboxamide ligand, *i.e.*, Fe(bpb)Cl(H_2O) onto nitrogen-doped graphene (NG) (**Figure 14a**).[71] With the immobilization of Fe(bpb)Cl(H_2O) onto NG support, the catalyst exhibited the CO_2-to-CO conversion in heterogenous aqueous media with the faradaic efficiency of 90% and the current density of 6 mA cm^{-2} at the overpotential of 0.47 V. While, Fe(bpb)Cl(H_2O) without NG only showed the inferior homogeneous ECR activity with a little current density of *ca.* 0.25 mA cm^{-2} at the overpotential of 0.41 V. For cyclam-based nickel complexes, the saturated primordial skeletons preclude non-covalent grafting on carbon substrates. To heterogenize this class of compounds *via* non-covalent attachment, the inclusion of a **π**-contributing group, such as pyrene substitution, is necessary.[72, 74] Indeed, Fontecave *et. al.* reported the exploitation of pyrene-functionalized nickel cyclam onto carbon nanotubes (**Figure 14b**), showing an excellent catalytic activity of CO_2-to-CO reduction (TOF = 4.27 s^{-1}, FE_{CO} = 90%).

1.8 Nickel(II) complexes featuring N_4-Schiff base macrocycles derived from diphenylamine-2,2'-dicarboxaldehyde

Despite numerous aza-macrocycle-based ECR catalysts, nickel(II) complexes featuring N_4-Schiff base macrocycles derived from diphenylamine-2,2'-dicarboxaldehyde, 1-Ni and 2-Ni, have drawn our interest since the structural motif of them is similar to cyclam and isocyclam ligands with the additional **π**-conjugation. Such features offer the possibility to explore their reactivity on carbon-based supports, and their peripheral modification is amenable to study the effect of N-H functionality and ligand flexibility toward ECR activity. It is important to highlight that these nickel complexes were reported by Black and Brooker group.[75-77] Yet, to the

best of our knowledge, these nickel complexes have not been studied and reported as ECR catalysts.

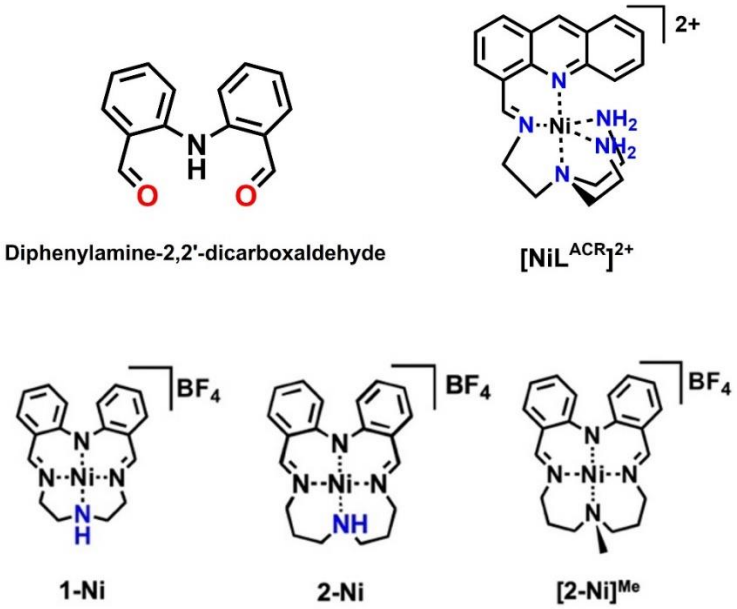

Figure 15 Chemical structures of diphenylamine-2,2'-dicarboxaldehyde and nickel complexes used in this study.

จุฬาลงกรณ์มหาวิทยาลัย
Chulalongkorn University

Herein, we synthesized three nickel(II) complexes with a new structure containing an N_4-Schiff base macrocycles (*i.e.*, 1-Ni, 2-Ni, $[2\text{-Ni}]^{Me}$) and explored their homogeneous and heterogeneous ECR behavior.[78] In terms of structural comparison, both 1-Ni and 2-Ni consist of tetradentate nitrogen-based macrocycles with varying sizes, allowing for the examination of the impact of ligand rigidity. Furthermore, we introduced a novel $[2\text{-Ni}]^{Me}$ compound, which possesses a similar structure to 2-Ni except the replacement of N-H functionality with a methyl group. This modification was made to investigate the significance of the N-H functionality in relation to ECR in homogeneous aprotic solvent versus heterogeneous aqueous system. Thereafter, these complexes were attached onto N-doped graphene, and evaluated their heterogeneous ECR activities in aqueous condition.

By changing the peripheral unit to tris(2-aminoethylamine), we unexpectedly synthesized the pentadentate acridine-based Schiff-base nickel complexes, *i.e.*, $[NiL^{ACR}]^{2+}$, of which the ligand scaffold is formed *via* the rearrangement of diphenylamine head unit during the templated [1+1] imine condensation (**Figure 15**). Also, $[NiL^{ACR}]^{2+}$ complexes were preliminary investigated the electrochemical properties toward electrochemical H_2 evolution.

Thesis objectives

1. To prepare Schiff base nickel(II) complexes derived from diphenylamine-2,2'-dicarboxaldehyde
2. To investigate the structure-reactivity relationship of the nickel macrocycles toward ECR.
3. To immobilize Schiff base nickel(II) complexes onto carbon supports for heterogeneous aqueous ECR.

จุฬาลงกรณ์มหาวิทยาลัย
Chulalongkorn University

CHAPTER 2

IMMOBILIZATION OF NICKEL(II) COMPLEXES CONTAINING N_4-SCHIFF BASE MACROCYCLES ON N-DOPED GRAPHENE FOR ELECTROCHEMICAL CO_2 REDUCTION

In this work, three nickel complexes containing N_4-Schiff base macrocycles (*i.e.*, 1-Ni, 2-Ni and [2-Ni]^{Me}) immobilized on N-doped graphene (Ni@NG) were developed based on molecularly dispersed nickel catalysts; in addition, their ECR performances were investigated in heterogeneous aqueous system.[78] It was found that three Ni@NG hybrid catalysts exhibited satisfactory ECR in bicarbonate solution with the faradaic efficiency 60-80% and the current density of 2-3 mA cm^{-2} at the overpotential of 0.56 V *vs.* RHE. Interestingly, the ECR activity of Ni@NG catalysts showed that the necessity of N-H functionality on ligand periphery has less pronounced effect to ECR in heterogeneous aqueous system whereby plenty of viable hydrogen-bond donors and proton sources (*i.e.*, water and bicarbonate ions) are available.

จุฬาลงกรณ์มหาวิทยาลัย
Chulalongkorn University

2.1 Materials and method

All reactions were conducted in the air unless otherwise stated. Manipulations involving air-sensitive reactions were carried out using standard Schlenk techniques under N_2. In all the reactions, solvents were purchased with a high purity grade and used either without purification or dried over 4 Å molecular sieves before use unless otherwise noted. Commercially available reagents were used as received without any further purification. 1-Ni, 2-Ni, diphenylamine-2,2'-dicarboxaldehyde were synthesized according to modified published procedure.[75, 76] 2 ,2'-iminodibenzoic acid (95%), lithium aluminium hydride (reagent grade, 95%), manganese(IV) dioxide (activated ~85%, particle size < 10 μm), N-doped graphene (>4wt%), Nafion solution (5wt%), tetrabutylammonium hexafluorophosphate

(NBu_4PF_6, electrochemical grade, >99%) and $NaHCO_3$ (99.7%) were purchased from Sigma-Aldrich. Diethylenetriamine (>99%), bis(3-aminopropyl) amine (>98%) and *N,N'*-diamino-*N*-methyl dipropylamine (98%) were obtained from Sigma-Aldrich and used as received. Milli-Q water (18.2 M Ω·cm) was used for preparation of aqueous solution. Carbon paper (TGP-H-60) was obtained from Alfa Aesar. Nafion polymeric membrane was received from Fuel Cell Store and activated in concentrated HNO_3 (65%, Merck) under gentle heat for 2 h prior to use for electrochemical measurements. N-doped graphene was treated in concentrated HNO_3 and washed with Milli-Q water until the pH was neutral.

2.2 Instrumentation

^1H NMR spectra were recorded at 298 K on a JEOL 500 MHz spectrometer. High-resolution electrospray ionization mass spectrometry (HR-ESI-MS) was employed using a Bruker MicrOTOFQ spectrometer to collect the mass spectra. UV-vis absorption spectra were obtained at room temperature on a Varian Cary 50 Probe using a quartz cuvette with an optical path length of 1 cm. Scanning electron microscopy (SEM) and energy dispersive X-ray spectroscopy (EDX) were conducted on a JEOL JSM-IT100. Inductively coupled plasma optical emission spectroscopy (ICP-OES) was Thermo Scientific ICAP 6500 model. Electrochemical measurements were performed on a Metrohm Autolab PGSTAT101 model.

จุฬาลงกรณ์มหาวิทยาลัย
Chulalongkorn University

2.3 Electrochemical measurements

2.3.1 Electrochemical measurements in non-aqueous electrolyte

Cyclic voltammetry (CV) of nickel complexes in 0.1 M N_4BuPF_6/CH_3CN (10 mL) was conducted at 25 °C in a one-compartment electrochemical cell. The electrochemical cell was equipped with a three-electrode configuration. The working electrode was glassy carbon electrode (Ø = 3.0 mm, A = 0.071 cm^2, BASI®). Before conducting the measurements, the glassy carbon electrode underwent polishing using an aqueous suspension of alumina powder. Subsequently, it was rinsed with Milli-Q water to remove any surface-adsorbed materials. (except for the scan-rate dependent experiment). The counter electrode was platinum coil whereas the reference electrode was a 0.01 M $AgNO_3/Ag$ (CH Instrument). All potentials are

referenced relative to an Ag/Ag^+ reference electrode and further subjected to external calibration with the ferrocene couple ($E_{Fc/Fc}^+$ = 0.09 V ± 0.01 V, ΔE_p = 65 mV).

2.3.2 Electrochemical measurements in aqueous electrolyte

The electrochemical measurements were carried out at a temperature of 25 °C using a two-compartment H-shaped cell. The cell was compartmentalized by a proton-exchange membrane, specifically Nafion 117, to separate two chambers. Likewise, three-electrode configuration was employed, which comprised of carbon paper (TGP-H-60) with and without the hybrid Ni/NG catalysts as the working electrode (1 cm^2), silver/silver chloride (Ag/AgCl, 3 M KCl, BASI®) as the reference electrode and platinum wire as the counter electrode. Platinum wire was subjected to flame annealing prior to use for measurements. In a typical experiment, 0.5 M $NaHCO_3$ solution was pre-saturated with N_2 (pH = 8.7) and CO_2 (pH = 7.4) gas and used as electrolytes (45 mL of electrolyte in cathodic and anodic chambers with *ca.* 28 mL of gas-headspace volume). To maintain a tightly sealed system, each chamber was outfitted with a silicone-PTFE septum and sealed with a Schott® screw cap (Aperture GL32). Before conducting the measurements, high-purity CO_2 (99.999%) and N_2 (99.999%) gases were introduced into the catholyte and anolyte chambers, respectively, for a duration of approximately 20 minutes. The measured potentials were quoted with reference to the Ag/AgCl electrode in a 3 M KCl electrolyte. Subsequently, the potentials were converted to the RHE (Reversible Hydrogen Electrode) scale by employing the Nernst equation:

จุฬาลงกรณ์มหาวิทยาลัย
CHULALONGKORN UNIVERSITY

$$E\ (V\ vs.\ RHE) = E\ (V\ vs.\ Ag/AgCl) + E^0\ (V\ vs.\ Ag/AgCl) + 0.0591pH \quad \textbf{(eq. 13)}$$

where E (V *vs.* Ag/AgCl) is the measured potential versus Ag/AgCl (3 M KCl) reference electrode and E^0 (V vs. Ag/AgCl) is the standard potential of Ag/AgCl (3 M KCl) reference electrode, E^0 (V *vs.* Ag/AgCl = 0.1976 V.

Controlled potential electrolysis (CPE) was conducted as a batch experiment, employing continuous stirring at a rate of 400 rpm throughout the electrolysis period.

To quantitatively analyze the gas products, a 4 mL portion of the headspace gas in the cathodic chamber was collected using a gas-tight syringe through the septa. The collected gas samples were then analyzed using gas chromatography (Agilent 8890 GC system) equipped with a thermal conductivity detector. The GC column was a select permanent gases column (CP7429, Agilent), consisting of two parallel columns: CP-Molseive 5 Å for the analysis of permanent gases and CP-PoraBOND Q for the analysis of CO_2. In terms of the temperature and pressure programming profiles, the GC system was operated at 150 °C for the thermal conductivity detector (TCD) and 35 °C for the oven during the separation of gas products, which lasted for 6 minutes. Subsequently, the oven temperature was raised to 200 °C at a ramp rate of 120 °C per minute for a duration of 5 minutes to clean the column. Ultra-high purity helium (He) gas was utilized as the carrier gas and introduced into the column at a pressure of 8 psi for 3 minutes, followed by an increase to 25 psi at a ramp rate of 100 psi min^{-1}, which was maintained for 8 minutes. For the detection of liquid products, an aliquot of electrolyte solution (0.5 mL) was mixed with deuterium oxide (1 mL) and taken to analysis with ^1H NMR spectroscopy. In the case of online experiments, the controlled potential electrolysis (CPE) was performed by integrating the electrochemical apparatus with a gas tube, which connected the headspace of the cathodic chamber to a gas-sampling loop in the GC instrument. Continuous delivery of CO_2 into the catholyte was maintained at a flow rate of 5 mL min^{-1}, regulated by a mass-flow meter (KOFLOC Kyoto, Model 3810DSII Series). Meanwhile, the electrolyte solution was constantly stirred at 400 rpm during the entire electrocatalytic process. Quantitative analysis of gas products was periodically investigated every 20 minutes by GC instrument. The Faradaic efficiencies of the products were calculated by comparing the number of generated gas molecules to the charge passed through the electrochemical cell during electrolysis. It was assumed that the production of one molecule of both CO and H_2 gases required the consumption of two electrons.

จุฬาลงกรณ์มหาวิทยาลัย
Chulalongkorn University

$$\%\text{Faradaic Efficiency (FE)} = (Q_{output}/Q_{input}) \times 100 \quad \textbf{(eq. 14)}$$

$$Q_{output} = z \times n \times F \quad \textbf{(eq. 15)}$$

$$Q_{input} = \frac{\int i\,dt}{F} \quad \textbf{(eq. 16)}$$

Turnover Frequency (TOF) = turnover Number (TON) / unit of time **(eq. 17)**

Turnover Number = mole of products / mole of catalysts **(eq. 18)**

where z is the number of electrons required to produce the products, n is the moles of products produced throughout the electrolysis, F is the Faraday's constant (96485 C mol^{-1}), and Q_{input} is the total amount of charge built-up during the electrolysis.

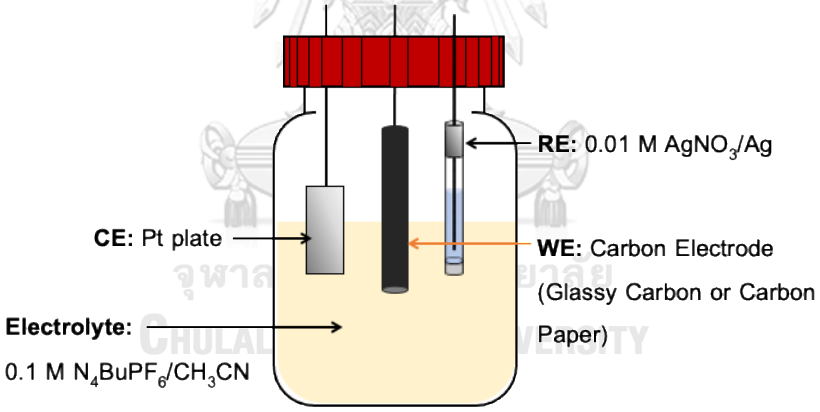

Figure 16 Schematic illustration of one-compartment electrochemical cell for electrochemical measurements in non-aqueous electrolyte

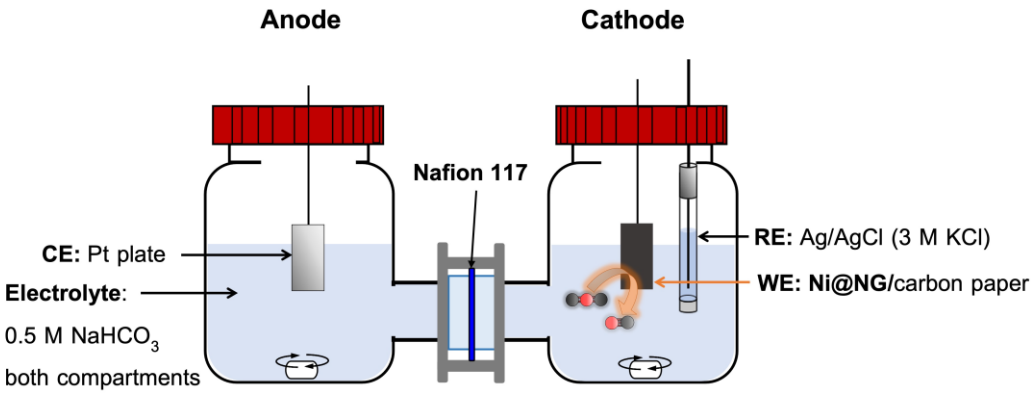

Figure 17 Schematic illustration of two-compartment H-shaped electrochemical cell for electrochemical measurements in aqueous electrolyte.

2.4 Synthetic Procedure for nickel(II) complexes containing N_4-Schiff base macrocycles

2.4.1 Synthesis of 2,2'-iminobis(methyl benzoate)

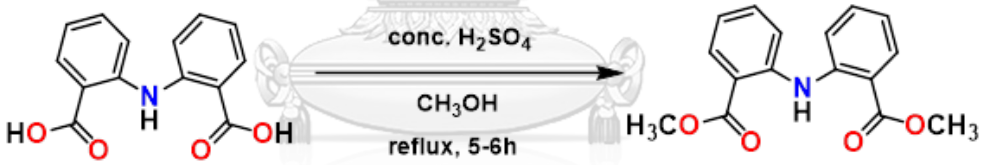

จุฬาลงกรณ์มหาวิทยาลัย
Chulalongkorn University

A two-neck round-bottom flask was charged with 2,2'-iminodibenzoic acid (500 mg, 1.94 mmol) and methanol (20 mL), then concentrated H_2SO_4 (1 mL) was slowly added into. The reaction mixture was refluxed for 5 hours and monitored by thin layer chromatography (TLC) using 1:4 ethyl acetate: hexane as a solvent system. After methanol was removed, the reaction flask was slowly added 10 mL solution of Na_2CO_3 (2.40 g). It is noted that the CO_2 bubbling occurs upon the addition of Na_2CO_3. After the bubbling subsided, the solution was extracted with 5 mL of 15% NaCl solution, followed by CH_2Cl_2 (3 x 10 mL). The combined organic layer was then washed with 10 mL of saturated NaCl solution, after which the CH_2Cl_2 was

removed by reduced pressure to afford the pale-yellow solid (477 mg, 86%). ^{1}H NMR (400 MHz, $CDCl_3$, 298 K): **δ**(ppm) = 3.94 (s, 6H, C*H*$_3$), 6.90 (t, *J* = 7.5 Hz, 2H, Ar*H*), 7.37 (t, *J* = 7.3 Hz, 2H, Ar*H*), 7.55 (d, *J* = 8.5 Hz, 2H, Ar*H*), 7.99 (d, *J* = 6.9 Hz, 2H, Ar*H*), 11.05 (s, 1H, N*H*).

2.4.2 Synthesis of 2,2'-iminobis(hydroxymethyl benzene)

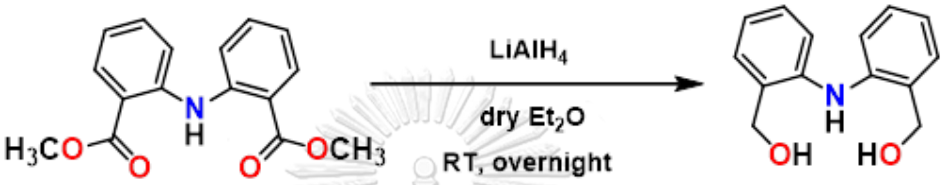

To a suspension of $LiAlH_4$ (151 mg, 3.97 mmol) in dry diethyl ether (40 mL) was cautiously added 2,2'-iminobis(methyl benzoate) (453 mg, 1.59 mmol) over a 15-minute period. The resulting mixture was stirred overnight, after which was quenched sequentially in ice bath by ethyl acetate (3 mL), water (3 mL), 15% NaOH (3 mL) and water (20 mL), and then the white solid was filtered off. The diethyl ether layer was collected, and the aqueous layer was extracted with CH_2Cl_2 (3 x 10 mL). The combined organic layer was removed under reduced pressure, resulting in the cream-colored solid which was further purified by precipitating in CH_2Cl_2/hexane to afford the white solid (255 mg, 70%). ^{1}H NMR (400 MHz, DMSO-d_6, 298 K): **δ**(ppm) = 4.48 (d, *J* = 5.0 Hz, 4H, C*H*$_2$), 5.26 (t, *J* = 5.1 Hz, 2H, O*H*), 6.87 (t, *J* = 7.2 Hz, 2H, Ar*H*), 7.04 (d, *J* = 7.9 Hz, 2H, Ar*H*), 7.15 (t, *J* = 7.4 Hz, 2H, Ar*H*), 7.31 (d, *J* = 7.3 Hz, 2H, Ar*H*), 7.40 (s, 1H, N*H*).

2.4.3 Synthesis of diphenylamine-2,2'-dicarboxaldehyde

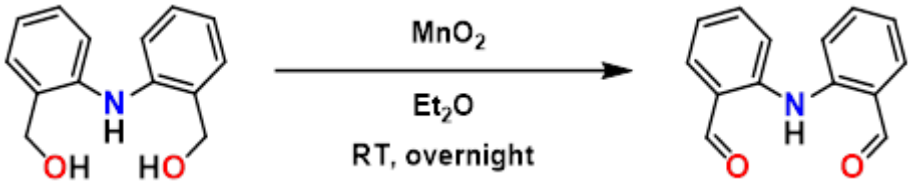

To a colourless solution of 2,2'-iminobis(hydroxymethyl benzene) (230 mg, 1.00 mmol) in dry diethyl ether (30 mL) was added an activated MnO_2 (1.75 g). The resulting black suspension was stirred at room temperature overnight. The MnO_2 was then filtered off and extracted with boiling chloroform (3 x 10 mL). The combined extracts and filtrate were concentrated to yield a yellow solid. This crude yellow solid was purified by chromatography on silica gel with 1:4 ethyl acetate: Hexane (R_f = 0.2), giving the title product as a bright yellow crystalline solid (138 mg, 62%). ^{1}H NMR (400 MHz, $CDCl_3$, 298 K): **δ**(ppm) = 7.08 (t, *J* = 7.3 Hz, 2H, Ar*H*), 7.47 (t, *J* = 7.6 Hz, 2H, Ar*H*), 7.55 (d, *J* = 8.0 Hz, Ar*H*), 7.71 (d, *J* = 7.7 Hz, 2H, Ar*H*), 10.03 (s, 2H, C*H*O), 11.36 (s, 1H, N*H*).

2.4.4 Preparation of N_4-Schiff base nickel(II) complexes

2.4.4.1 Preparation of [1-Ni](BF_4)

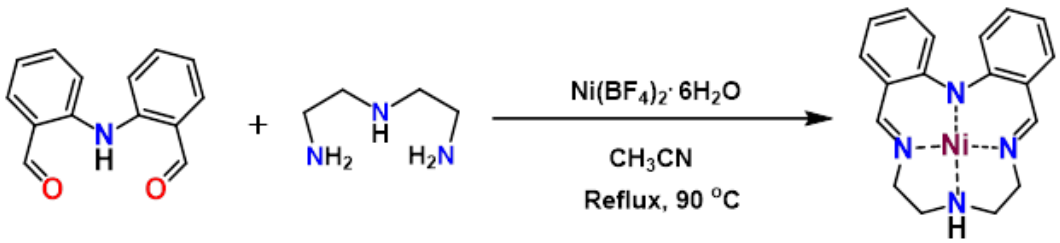

To a bright yellow refluxing solution of diphenylamine-2,2'-dicarboxaldehyde (102 mg, 0. 45 mmol) in acetonitrile (30 mL) was added a solution of nickel(II)tetrafluoroborate hexahydrate (159 mg, 0.45 mmol) in acetonitrile (5 mL). The solution immediately turned crimson in color. Then, a solution of diethylenetriamine (47.5 mg, 0.45 mmol) in acetonitrile (10 mL) was added dropwise,

causing a dark red color. The resulting solution was subsequently subjected to reflux at 90 °C overnight. Following reflux, the solution was concentrated under reduced pressure and subjected to diethyl ether diffusion. Dark red crystalline solid was collected and dried *in vacuo* (122 mg, 60%). ESI(+) MS(*m/z*) (MeCN): $[Ni^{II}L^{Et}]^+$ calculated 349.0965, experiment 349.0958. UV-Vis (MeCN): λ_{max}/nm = 320, 410sh, 455, 545.

2.4.4.2 Preparation of [2-Ni](BF_4)

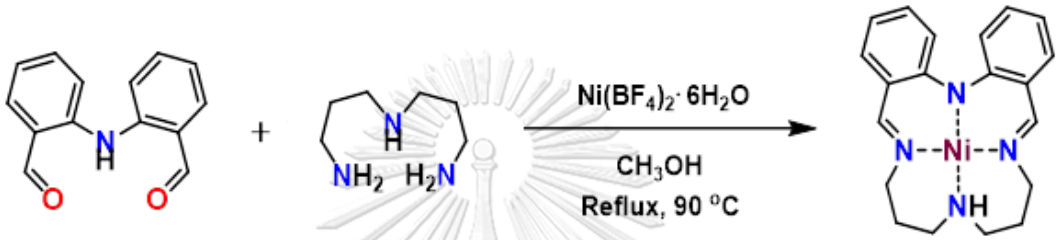

Nickel(II)tetrafluoroborate hexahydrate (78.5 mg, 0.231 mmol) in methanol (2 mL) was added to a bright yellow solution of diphenylamine-2,2'-dicarboxaldehyde (52 mg, 0.231 mmol) in methanol (25 mL) under reflux conditions. The solution slowly turned orange in color. A solution of bis(3-aminopropyl)amine (30 mg, 0.231 mmol) in methanol (10 mL) was added dropwise to the reaction mixture, resulting in the formation of a dark red solution. The resulting solution was then refluxed at 90 °C for 2 h, during which the color of the solution changed to dark green. This dark green solution was concentrated under reduced pressure and subjected to diethyl ether diffusion. Dark green block-shaped crystals were collected and dried *in vacuo* (47 mg, 43%) ESI(+) MS(*m/z*) (MeCN): $[Ni^{II}L^{Pr}]^+$ calculated 377.1267, experiment 377.1267. UV-Vis (MeCN): λ_{max}/nm = 326, 409, 480, 615.

จุฬาลงกรณ์มหาวิทยาลัย
CHULALONGKORN UNIVERSITY

2.4.4.3 Preparation of [2-Ni]^{Me}(BF_4)

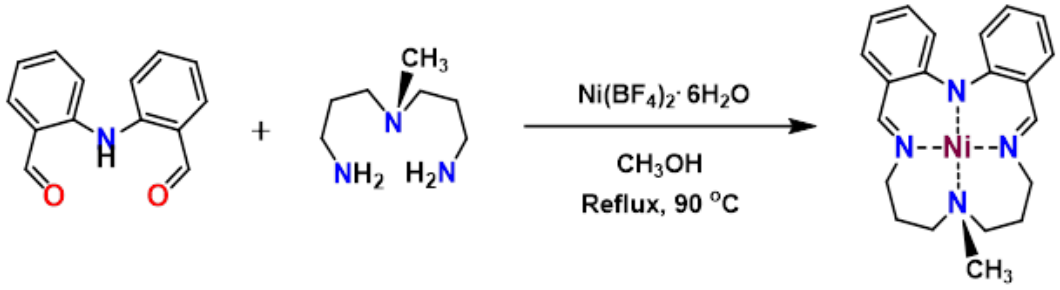

A bright yellow refluxing solution of diphenylamine-2,2'-dicarboxaldehyde (105 mg, 0.466 mmol) in methanol (25 mL) was prepared. To this solution, nickel(II)tetrafluoroborate hexahydrate (159 mg, 0.466 mmol) in methanol (5 mL) was added, resulting in a slow change of the solution color to orange. Subsequently, a solution of N,N'-diamino-N-methyl dipropylamine (68 mg, 0.466 mmol) in methanol (10 mL) was added dropwise, causing an immediate transformation of the solution to a dark red color. The resulting solution was refluxed at 90 °C for 2 h. Afterward, the solution was concentrated under reduced pressure and subjected to diethyl ether diffusion. Dark green block-shaped crystals were collected and dried *in vacuo* (125 mg, 56%) ESI(+) MS(*m/z*) (MeCN): [2-Ni^{Me}]$^+$ calculated 391.1496, experiment 391.1569 UV-Vis (MeCN): λ_{max}/nm = 328, 409, 490, 627.

2.4.5 Preparation of Ni@NG hybrid catalysts

N-doped graphene (20 mg) was dispersed and sonicated in Milli-Q water (10 ml) for 1 h. Subsequently, a solution of the nickel complex (20 mg), namely 1-Ni, 2-Ni, or [2-Ni]^{Me}, in CH_3CN (10 ml) was added to the N-doped graphene suspension and further sonicated for 1 h. The resulting mixture was then stirred under reflux conditions at 90 °C for 24 h. The hybrid Ni@NG catalyst was isolated by centrifugation for 30 min, washed with Milli-Q water (20 mL), and finally subjected to lyophilization to obtain a solid black powder

2.4.6 Preparation of catalyst ink and fabrication of electrode

The catalyst ink was prepared by dispersing 5 mg of the hybrid catalyst (1-Ni@NG, 2-Ni@NG, and [2-Ni]^{Me}@NG) in a mixture comprising 0.05 mL of Nafion 117

solution (5wt%), 0.30 mL of propan-2-ol, and 0.65 mL of Milli-Q water. This dispersion process involved high-power sonication for a duration of 5 min. The working electrode was prepared by applying 0.1 mL of the catalyst ink onto a carbon paper, covering an area of 1 cm^2, resulting in a total mass loading of 0.5 mg cm^{-2}. Subsequently, the prepared electrodes were left to dry overnight on the bench top

2.4.7 Determination of Ni content in hybrid catalysts

The quantity of nickel (Ni) in the hybrid catalysts was determined using inductively coupled plasma optical emission spectroscopy (ICP-OES) with the Thermo Scientific ICAP 6500 Model. Before conducting the measurements, the hybrid Ni@NG catalysts were subjected to digestion in concentrated HNO_3 (1 mL). Subsequently, the resulting solid suspension was filtered using a syringe filter (Nylon, Ø = 0.45 μm), and the filtrate was collected. To create a diluted solution, the collected filtrate was mixed with 1%v/v HNO_3 solution

2.5 Structural comparison of the N_4-Schiff base nickel complexes

To begin with, nickel complexes, 1-Ni and 2-Ni, which contain N_4-Schiff base macrocycles, were synthesized using a nickel-templated [1+1] imine condensation method. This involved the reaction between 2,2'-iminobisbenzaldehyde and their respective polyamine counterparts, following the procedure described in previous literature.[75, 76] The synthetic route to preparation of diphenylamine-2,2'-dicarboxaldehyde was achieved by using 2,2'-iminodibenzoic acid as the starting precursors. The preparation of diphenylamine-2,2'-dicarboxaldehyde consists of three chemical reaction steps: (i) acid-catalyzed esterification, (ii) reduction of ester using $LiAlH_4$ and (iii) oxidation of alcohol using activated MnO_2. It should be noted that X-ray structures of 1-Ni and 2-Ni were previously reported by Brooker and coworkers.[75, 76] To investigate the role of N-H in the ECR activity, a newly synthesized $[2\text{-Ni}]^{Me}$ complex was prepared using a similar procedure as before. However, in this case, N,N'-diamino-N-methyl dipropylamine was used as the polyamine instead. This

จุฬาลงกรณ์มหาวิทยาลัย
Chulalongkorn University

modification allowed for the examination of the impact of N-H functionality on the ECR activity.

The [2-Ni]^{Me} complex was isolated by slowly introducing diethyl ether into the CH_3OH layer, resulting in the formation of dark green block-shaped crystals those is suitable for X-ray analysis. Single X-ray diffraction analysis was conducted, revealing that [2-Ni]^{Me} crystallizes in the monoclinic system with the space group $P2_1/n$. The unit cell of the crystal structure consists of one crystallographic unique nickel ion and one hexafluorophosphate counter ion. The molecular structure of cationic species of the complex is illustrated in **Figure 18**. The central nickel(II) ion in the [2-Ni]^{Me} complex exhibits distorted square planar geometry, where it is coordinated by four nitrogen atoms from the ligand. All the nitrogen atoms occupy the equatorial positions around the nickel ion. The Ni-N lengths are in the range of 1.880(4) - 2.015(4) Å (**Table 3**).

The three complexes (1-Ni, 2-Ni, and [2-Ni]^{Me}) exhibit a distorted square planar geometry, where the nickel(II) centers are coordinated by four nitrogen atoms in the equatorial plane. However, there are notable differences between 1-Ni and 2-Ni in terms of the size of their macrocyclic ligands, resulting in differences in rigidity and twist angles of the diphenylamine unit. The more rigid complex, 1-Ni, has a twist angle of 47.3°, while the more flexible complex, 2-Ni, has a twist angle of 63.4°. Interestingly, the twist angle of [2-Ni]^{Me} is 60.9°, which is comparable to that of 2-Ni. This suggests that the presence of the methyl group does not significantly influence the macrocyclic flexibility. A detailed comparison of bond lengths, bond angles, and twist angles for the nickel complexes can be found in **Table 2** and **Table 3**. With these structural features, it is expected that the nickel complexes will exhibit different electronic properties along with catalytic activities in the electrocatalytic reduction of CO_2.

จุฬาลงกรณ์มหาวิทยาลัย
Chulalongkorn University

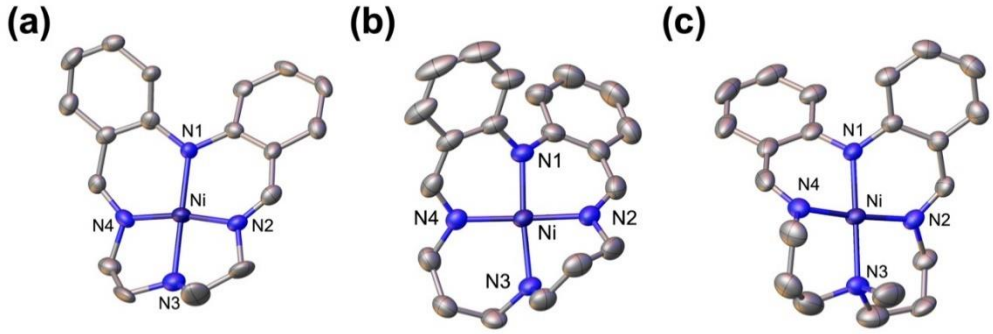

Figure 18 Perspective views of cationic complexes (a) 1-Ni, (b) 2-Ni, and (c) $[2\text{-Ni}]^{Me}$, showing the coordination environment of the nickel(II) atom. Anions and hydrogen atoms are omitted for clarity. The X-ray structure of 1-Ni and 2-Ni was obtained from ref. 76 and 75

Table 2 Crystal data and structural refinement for 1-Ni, 2-Ni, and $[2\text{-Ni}]^{Me}$

Compound	1-Ni[a]	2-Ni[b]	$[2\text{-Ni}]^{Me}$
Empirical Formula	$C_{18}H_{19}BF_4N_4Ni$	$C_{20}H_{23}BF_4N_4Ni$	$C_{21}H_{25}BF_4N_4Ni$
Formula Weight	436.89	464.94	478.98
Temperature (K)	90(2)	90(2)	296(2)
Crystal System	monoclinic	monoclinic	monoclinic
Space Group	*Pn*	$P2_1/n$	$P2_1/n$
a (Å)	7.2737(15)	6.2103(3)	9.7951(14)
b (Å)	10.6471(18)	28.8447(18)	9.4102(13)
c (Å)	11.3778(15)	11.4023(7)	22.736(3)
α (°)	90	90	90
β (°)	94.181(3)	103.148(10)	98.096(5)
γ (°)	90	90	90
V (Å^3)	878.8(3)	1989.0(2)	2083.8(5)
Z	2	4	2
ρ_{calc} (g/cm^3)	1.651	1.553	1.527

จุฬาลงกรณ์มหาวิทยาลัย
Chulalongkorn University

μ (mm^{-1})	1.156	1.027	0.982
Reflns collected/unique	11732/3339	13331/4059	35463/5173
GOF on F^2	1.014	1.116	1.111
R_{int}, R_{sigma}	0.0574,0.0737	0.0464, 0.0472	0.0796, 0.0469
R_1, wR_2 [$I > 2\sigma(I)$]	0.0504, 0.1048	0.0398, 0.0983	0.0879, 0.2227
R_1, wR_2 (all data)	0.0828, 0.1169	0.0531,0.1184	0.1085, 0.2360
Max./min. residual (e $Å^{-3}$)	-0.37/-0.29	0.46/-0.34	1.05/−0.81
CCDC	804221	913820	2215460

[a] and [b] crystallographic data was obtained from reference 76 and 75, respectively.

Table 3 Comparison of selected bond lengths (Å), angles (°) and twist of diphenylamine unit for 1-Ni, 2-Ni and $[2\text{-Ni}]^{Me}$.

	1-Ni[a]	2-Ni[b]	$[2\text{-Ni}]^{Me}$
Bond lengths [Å]			
Ni1–N1	1.869(3)	1.867(2)	1.907(5)
Ni1–N2	1.861(7)	1.894(2)	1.914(4)
Ni1–N3	1.924(4)	1.942(2)	2.115(2)
Ni1–N4	1.830(7)	1.899(2)	2.014(4)
Bond angles [°]			
N1–Ni1–N2	94.9(3)	89.48(10)	87.4(2)
N1–Ni1–N3	179.3(4)	174.78(10)	175.12(2)
N1–Ni1–N4	95.3(3)	90.51(10)	92.0(2)
N2–Ni1–N3	85.2(3)	85.98(10)	88.34(2)
N2–Ni1–N4	169.83(19)	174.32(9)	179.5(2)
N3–Ni1–N4	84.6(3)	94.26(10)	92.2(2)
Twist of phenyl rings [°]	47.3	63.4	60.9

[a] and [b] crystallographic data was obtained from reference 76 and 75, respectively.

จุฬาลงกรณ์มหาวิทยาลัย
CHULALONGKORN UNIVERSITY

2.6 Electrochemical studies of nickel complexes in NBu_4PF_6/CH_3CN

The electrochemical properties of the nickel complexes (1-Ni, 2-Ni, and [2-Ni]^{Me}) were investigated in CH_3CN with 0.1 M Bu_4NPF_6 as the supporting electrolyte. A glassy carbon working electrode was employed for the experiments. The reference electrode used was a 0.01 M $AgNO_3/Ag$ electrode. It is important to note that all potentials in non-aqueous conditions were externally referenced to the ferrocenium/ferrocene couple ($Fc^{+/0}$). Under these experimental conditions, the half potential of the ferrocenium/ferrocene couple ($Fc^{+/0}$) was determined to be 0.09 V ± 0.01 V, with a separation between the anodic and cathodic peak potentials (ΔE_p) of 65 mV

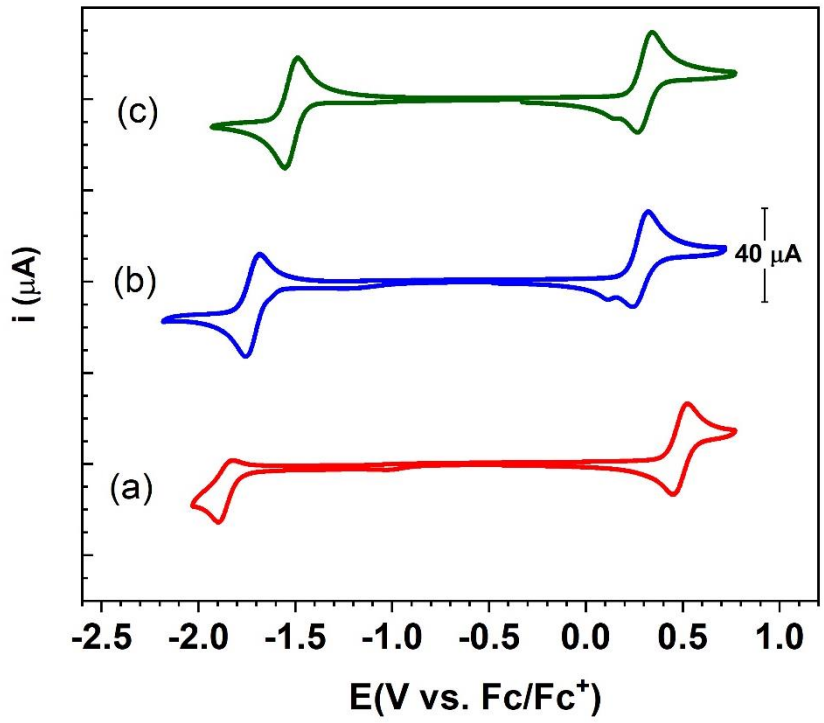

Figure 19 CVs of 1 mM (a) 1-Ni, (b) 2-Ni and (c) [2-Ni]^{Me} recorded in N_2-saturated CH_3CN/ 0.1 M NBu_4PF_6/CH_3CN solution (**ν** = 0.1 V/s, glassy carbon electrode: A = 0.071 cm^2).

Table 4 Summarized electrochemical data of N_4-Schiff base nickel macrocycles.

Complex	E_{pc1} (V)	E_{pa1} (V)	$E_{1/2}$ (V)[b] [ΔE_p (mV)][c]	E_{pc2} (V)	E_{pa2} (V)	$E_{1/2}$ (V)[b] [ΔE_p (mV)][c]
1-Ni	+0.45	+0.52	+0.49 [73]	-1.89	-1.82	-1.86 [80]
2-Ni	+0.25	+0.33	+0.29 [82]	-1.75	-1.68	-1.72 [71]
$[2\text{-Ni}]^{Me}$	+0.27	+0.34	+0.31 [76]	-1.56	-1.49	-1.52 [66]

[a] All voltammograms were recorded in CH_3CN; the potentials are reported *vs*. the $Fc^{+/0}$ couple. Conditions: scan rate = 0.1 V/ s, compound (1 mM), Bu_4NPF_6 (0.1 M), glassy carbon working electrode. Under these conditions we found ΔE_p ($Fc^{+/0}$) = 65 mV. [b] $E_{1/2} = (E_{pc} + E_{pa})/ 2$, when E_{pc} = cathodic peak potential and E_{pa} = anodic peak potential. [C] $\Delta E_p = |E_{pc} - E_{pa}|$.

The cyclic voltammogram of 1-Ni displayed a quasi-reversible reduction process when scanning towards negative potentials. This reduction process occurred at the half potential ($E_{1/2}$) of -1.86 V, with ΔEp of 80 mV. This reduction process is attributed to the Ni^{II}-to-Ni^{I} reduction process (**Figure 19a**). The redox event exhibited a smaller return wave, indicating some degree of irreversibility. However, it was observed that the ratio of the anodic peak current (i_{pa}) to the cathodic peak current (i_{pc}) increased with the expedition of the scan rate (**Figure 20**). This suggested that the event is competitive and complies with E_rC_i mechanism (*i.e.*, reversible electron transfer followed by an irreversible homogeneous chemical reaction).[79] It is important to note that the irreversibility of the reduction process of 1-Ni may be attributed to the structural rigidity of the ethylene linkages in the peripheral units of the complex. This rigidity can hinder the formation of a square planar Ni(I) species and proceed subsequent chemical reactions.[80] Interestingly, the enlargement of macrocycles leads to reversible reduction event at $E_{1/2}$ = -1.72 V with ΔE_p = 71 mV for 2-Ni, and $E_{1/2}$ = -1.52 V with ΔE_p = 66 mV for $[2\text{-Ni}]^{Me}$ (**Figure 19b-c**). The larger macrocyclic size (*i.e.*, 2-Ni and $[2\text{-Ni}]^{Me}$) causes an anodic shift in the reduction potentzial compared to that

จุฬาลงกรณ์มหาวิทยาลัย
CHULALONGKORN UNIVERSITY

of 1-Ni. This can be attributed to the increased flexibility of the ligand scaffolds, which enables easier reduction of these nickel complexes into a distorted tetrahedral conformation.

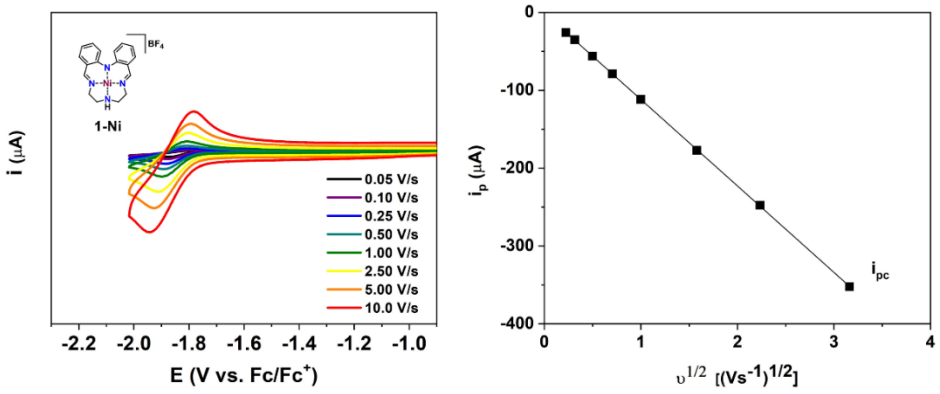

Figure 20 CVs of 1-Ni in CH_3CN at different scan rate and plots of reductive current vs. the square root of the scan rate of 1-Ni in CH_3CN at E = -1.86 V vs. $Fc^{+/0}$.

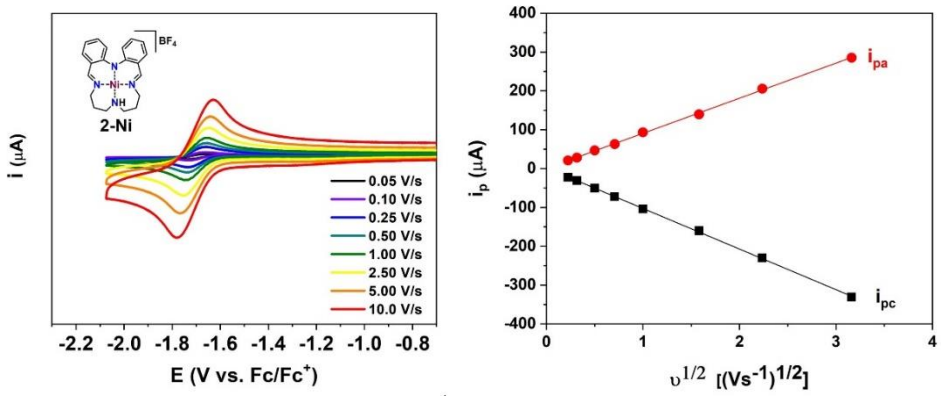

Figure 21 CVs of 2-Ni in CH_3CN at different scan rate and plots of reductive and oxidative currents vs. the square root of the scan rate of 2-Ni in CH_3CN at E = -1.72 V vs. $Fc^{+/0}$.

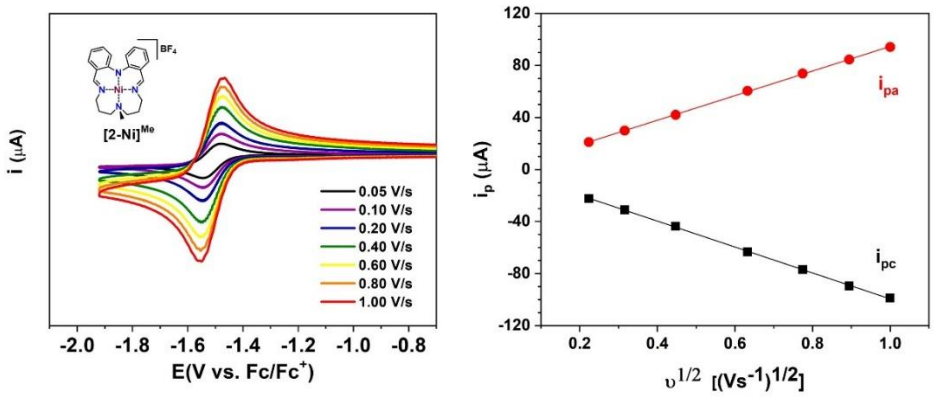

Figure 22 CVs of $[2\text{-Ni}]^{Me}$ in CH_3CN at different scan rate and plots of reductive and oxidative currents vs. the square root of the scan rate of $[2\text{-Ni}]^{Me}$ in CH_3CN at E = -1.52 V vs. $Fc^{+/0}$.

On scanning to positive potentials, 1-Ni, 2-Ni and $[2\text{-Ni}]^{Me}$ have an oxidation process at $E_{1/2}$ = +0.49 V with ΔE_p = 73 mV, $E_{1/2}$ = +0.29 V with ΔE_p = 82 mV, and $E_{1/2}$ = +0.31 V with ΔE_p = 76 mV, respectively (**Figure 19**). CVs of each Ni complex at different scan rates illustrate that the anodic and cathodic peak currents exhibit a linear relationship with the square root of the scan rate ($\nu^{1/2}$) from 0.05 to 10 V/s (**Figure 20**-**Figure *22***), complied with freely diffused process. Redox potentials of 1-Ni, 2-Ni and $[2\text{-Ni}]^{Me}$ are summarized in **Table 4**.

จุฬาลงกรณ์มหาวิทยาลัย
CHULALONGKORN UNIVERSITY

To explore the ECR activities, CVs of three nickel complexes were investigated in the CO_2-saturated N_4BuPF_6/CH_3CN electrolyte. After exposure to CO_2 atmosphere, CVs of 1-Ni exhibited an increase in current at the reduction potential of the Ni^{II}/Ni^{I} redution (*ca.* -1.90 V vs. Fc/Fc^+) This was followed by a catalytic response signal, indicating the occurrence ECR which was likely to the involvement of the Ni^{I} centers in the catalytic reaction (**Figure 23a**). In comparison, the peak current observed under catalytic conditions (i_c) was higher than the peak current observed in the absence of the CO_2 substrate (i_p). This difference in peak currents provides a comparative measure of the electrocatalytic activity for CO_2 reduction (i_c / i_p). The

values of i_c and i_p were recorded as -1.40 mA and -0.87 mA for 1-Ni and 2-Ni, respectively. The higher value of i_c / i_p implies a better catalytic performance toward the reduction of CO_2. For 2-Ni, the peak shape became irreversible in the presence of CO_2 together with the current enhancement (**Figure 23b**). It was observed that the transition from reversible to irreversible peaks was not clearly observed in the case of 1-Ni, primarily due to the inherent irreversibility of the Ni^{II}/Ni^{I} reduction process. Furthermore, 2-Ni exhibited a slight cathodic shift of approximately 30 mV and a modest increase in current density, with a value of i_c / i_p = 1.28. In comparison, the relatively lower ECR activity, as indicated by the i_c / i_p ratio, could be attributed to the increased flexibility of the macrocyclic ligand. This increased flexibility leads to a more distorted configuration, which may interact less favorably with CO_2 molecules during the catalytic process. The introduction of a methyl substituent on the peripheral units resulted in $[2\text{-Ni}]^{Me}$, and its CV remained largely unchanged when CO_2 was sparged into the solution, suggesting that the N-H functionality present in the ligand framework plays an important role in ECR process (**Figure 23c**). The presence of the N-H functionality is likely responsible for facilitating the interaction between the catalyst and CO_2, leading to enhanced ECR activity.

จุฬาลงกรณ์มหาวิทยาลัย
Chulalongkorn University

To promote the proton-coupled electron transfer process, a small amount of water was introduced as a proton source. In the presence of CO_2 and 1 M H_2O, CVs of 1-Ni and 2-Ni exhibited further enhancements in current. However, $[2\text{-Ni}]^{Me}$ showed a relatively smaller change in current enhancement and a reduced wave return at the oxidative peak current. These results suggest that $[2\text{-Ni}]^{Me}$ may function as an electrocatalyst for the ECR process to some extent, although its performance is inferior to its counterpart, 2-Ni. It is worth noting that the lower activity of $[2\text{-Ni}]^{Me}$ can be attributed to its lower $E_{1/2}$ value for the generation process of the active Ni species. This lower $E_{1/2}$ indicates a reduced driving force for the ECR process. As a

result, $[2\text{-Ni}]^{Me}$ exhibits lesser activity compared to its counterparts in facilitating the ECR. Addition of water at the same level (1 M H_2O) under N_2 atmosphere illustrated no significant current enhancement in CVs, implying that these nickel complexes are preferentially catalyzing ECR rather than HER (**Figure S11**). Moreover, increasing concentrations of H_2O in the presence of CO_2 contributed to the current response, which gradually increased at the peak potential and shifted the onset potential. This suggests that ECR can be facilitated by the presence of a proton source, enabling proton-coupled electron transfer (PCET) processes. Therefore, all nickel complexes show promising activity as competent catalysts for ECR, particularly 1-Ni and 2-Ni. The minimal change observed in CVs of $[2\text{-Ni}]^{Me}$ indicates that the N-H functional groups play an important role in facilitating ECR activity in an aprotic solvent like CH_3CN.

จุฬาลงกรณ์มหาวิทยาลัย
CHULALONGKORN UNIVERSITY

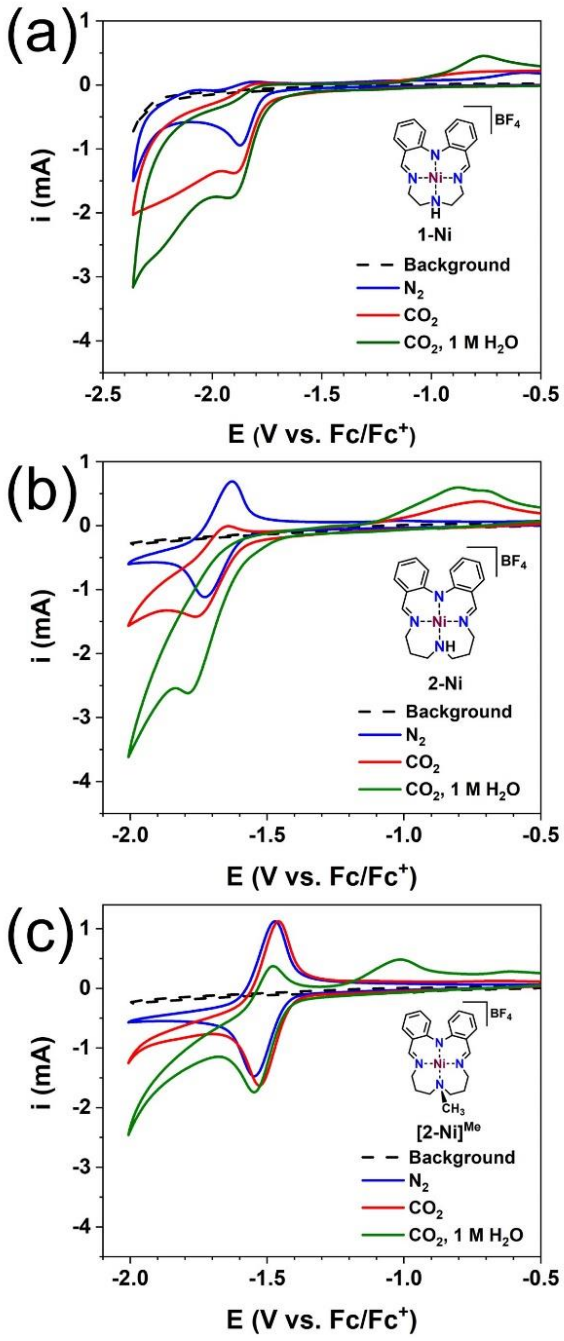

Figure 23 Cyclic voltammograms of (a) 1-Ni, (b) 2-Ni, and (c) $[2\text{-Ni}]^{Me}$ at 1 mM concentration in 0.1 M NBu_4PF_6/CH_3CN (**ν** = 0.1 V/s) under N_2 (blue); under CO_2 without 1 M H_2O (red), and with 1 M H_2O (green). Background signals under CO_2 were collected and illustrated in black dashed line. Carbon paper (A = 1 cm^2) was used as working electrode.

2.7 Immobilization of nickel complexes onto N-doped graphene

Based on the results obtained from CV studies in a CO_2 atmosphere, it was observed that 1-Ni and 2-Ni exhibited enhanced current responses, indicating promising activity for ECR. Building on these findings, further investigations were conducted to develop these nickel complexes for heterogeneous ECR in water. Water was chosen as the medium due to its advantages in terms of product separation and practical application. In order to achieve electrochemical CO_2 reduction in water, the concept of non-covalent immobilization onto carbon supports was employed. Among the various options for carbon-supported materials, nitrogen-doped graphene (NG) was selected as the support in this study. NG possesses nitrogen dopants and N-containing functional groups on its matrix, which are expected to enhance the ability of CO_2 capture near the electrode surface.[81-83] For our nickel complexes, the establishment of **π-π** stacking interaction between diphenylamine moieties in nickel complexes and graphene motifs in NG as well as ligation of N donors from NG to the Ni centers in nickel complexes are considered as important interactions. The adsorption of Ni complexes on N-doped graphene supports was investigated by using UV-visible spectra (**Figure S13**). In this experiment, a solution of Ni complexes was prepared at 1 mM in CH_3CN: H_2O (1:1) as stock solution and diluted to 0.1 mM solution (10 mL) which is the appropriate concentration to observe under UV-visible spectroscopy. Thereafter, a tiny amount of NG (1 mg) was added into 0.1 mM solution of nickel complexes and was sonicated for 5 min. The solid suspension was filtered out through syringe filter (Nylon, Ø = 0.45 μm), while the filtrate solution was taken to measure UV-visible adsorption. From results, the absorbance of charge transfer bands and d-d bands of nickel complexes was slightly decreased when NG was added, and the solution was briefly sonicated. This could suggest the feasible absorption of Ni complexes on the NG surfaces to some extent. Therefore, three nickel complexes were immobilized on N-doped graphene, denoted as Ni@NG, with assistance of sonication and refluxing in the

จุฬาลงกรณ์มหาวิทยาลัย
Chulalongkorn University

CH_3CN: H_2O solution to give Ni@NG catalysts. The Ni@NG catalysts were characterized using scanning electron microscopy (SEM), energy dispersive X-ray spectroscopy (EDS), and inductively coupled plasma-optical emission spectroscopy (ICP-OES). The SEM images of 1-Ni@NG, 2-Ni@NG, and $[2\text{-Ni}]^{Me}$@NG at high magnification revealed the micro-platelet structure of the NG phase, with the surface of Ni@NG remaining unchanged after immobilization. Furthermore, the Ni element was evenly distributed on the surface of NG without significant aggregation. The EDS spectrum of Ni@NG exhibited peaks corresponding to carbon (C) from NG, nitrogen (N) from both the nickel complexes and NG, and nickel (Ni) peaks originating from the nickel complexes (**Figure S16-19**). It is important to note that the obscured N peaks observed in the EDS spectrum were attributed to the overlapping of C peaks. However, the peak intensity of the Ni element in the Ni@NG catalysts was relatively low. This can be attributed to the weak interaction between the nickel complexes and NG, which is likely caused by the inherent twist of the ligands. The pristine NG, on the other hand, did not exhibit any Ni peaks in the EDS spectrum, confirming that the source of the Ni species originated from the immobilization of the nickel complexes. To estimate the quantity of Ni species onto NG, the number of Ni coverage ($\Gamma_{coverage,\ Ni}$) for 1-Ni@NG, 2-Ni@NG, and $[2\text{-Ni}]^{Me}$@NG was obtained and calculated by ICP-OES to be 3.9, 2.6, and 2.0×10^{-7} mol cm^{-2} respectively. The highest amount of Ni coverage for 1-Ni@NG was likely to the most rigidity of 1-Ni framework which is more favorable to establish a **π-π** stacking interaction and lead to the adsorption on NG supports. Meanwhile, 2-Ni and $[2\text{-Ni}]^{Me}$ possess more flexibility in their framework, resulting in the more twisted structure and the less number of Ni coverage

จุฬาลงกรณ์มหาวิทยาลัย
Chulalongkorn University

2.8 Electrochemical studies of Ni@NG catalysts in aqueous electrolyte

Prior to electrochemical investigation in aqueous solution, the working electrodes were fabricated by drop-casting catalyst inks comprised of Ni@NG as catalyst and Nafion as binder in a mixture of H_2O: propan-2-ol with a total mass loading of 0.5 mg cm^{-2} onto carbon papers. In this study, the H-shaped cell

containing anodic and cathodic chambers was compartmentalized by Nafion 117 membrane – a proton-exchange membrane – to prevent the re-oxidation of reduced products at the anode. The electrochemical reduction of CO_2 was performed in a CO_2-saturated 0.5 M $NaHCO_3$ solution with a pH of 7.4. Initially, we compared the ECR reactivity of 1-Ni@NG to control samples, including NG and carbon paper (CP), using CVs and controlled potential electrolyses (CPEs). Subsequently, CV and CPE results were also obtained for 2-Ni@NG and $[2\text{-Ni}]^{Me}$@NG. During the CV measurements, the potential was swept at a scan rate of 0.05 V/s, ranging from 0.73 V to -0.97 V *vs.* RHE. The CVs of 1-Ni@NG under CO_2 saturation exhibited a similar pattern, with a higher current density observed at a slightly lower onset potential (approximately -0.57 V *vs*. RHE) compared to those obtained under N_2 environment (**Figure 24a**). However, it should be noted that the distinct peaks of the nickel complexes were not observed once they were immobilized on the NG supports, making it difficult to determine the value of the electrochemically active species (**Γ**ea). As a control experiment, NG electrodes showed a lower enhancement of current density at more negative potentials. Furthermore, carbon paper electrodes exhibited no significant catalytic activity under CO_2 conditions. This suggests the potential catalytic activity of 1-Ni@NG electrodes at the operational potential.

จุฬาลงกรณ์มหาวิทยาลัย
Chulalongkorn University

2.8.1 Controlled potential electrolysis (CPE)

Chronoamperometric measurements were conducted for a duration of an hour at -0.67 V vs. RHE in both N_2- and CO_2-saturated 0.5 M $NaHCO_3$ solutions to investigate the product distribution, specifically in terms of faradaic efficiency (FE). In the presence of CO_2, the chronoamperometric response of 1-Ni@NG displayed a relatively stable current density of approximately 2.3 mA cm^{-2} throughout the one-hour electrolysis period. On the other hand, a lower current density of 1.5 mA cm^{-2} was observed during bulk electrolysis under N_2-saturated conditions. This indicates that the presence of CO_2 had a positive effect on the current density (**Figure 24b**). Likewise, the constant current-time profiles were observed in the case of NG and

carbon paper electrodes both under N_2 and CO_2 atmosphere, albeit lower in the current density (**Figure 24b**). According to the GC quantitative analysis, CPE of 1-Ni@NG in CO_2-saturated 0.5 M $NaHCO_3$ for 1 h yielded CO as a major product with the FE of 81 ± 3% and the CO quantities of 37.8 ± 6 μmol (**Figure 24c-24d**), whereas the control NG electrode showed a minimal activity of CO production with the FE of 20 ± 2% concomitant with H_2 evolution with the FE of 47 ± 4%. The observed H_2 evolution was caused by the competent water reduction near the electrode surface.

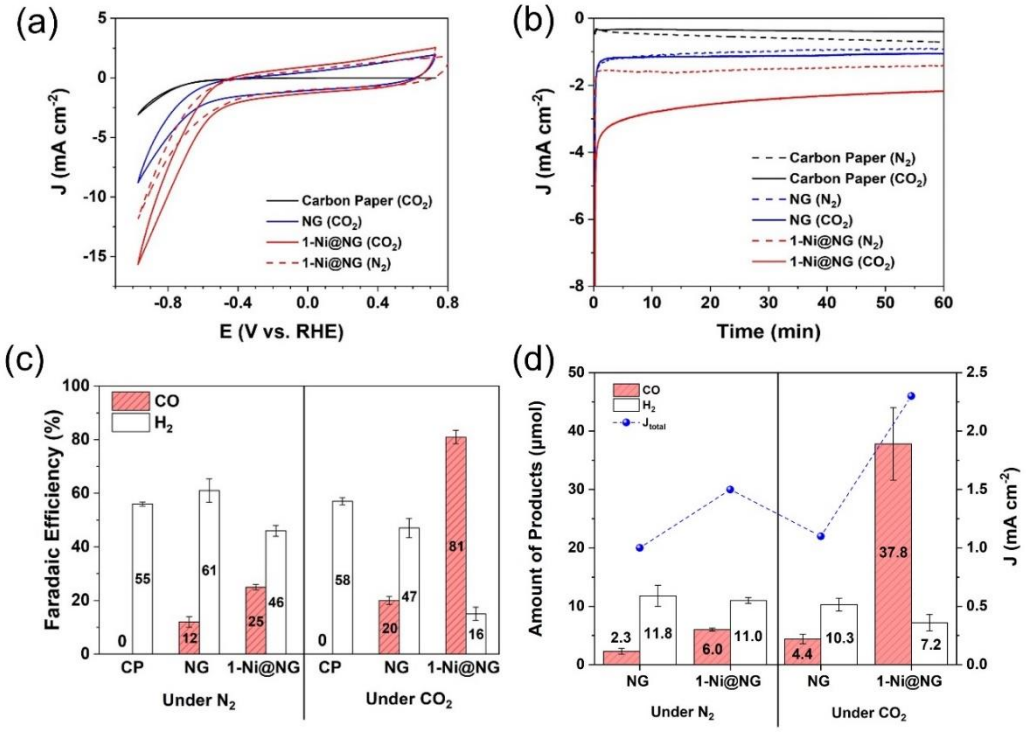

Figure 24 (a) Cyclic voltammograms of carbon paper (black trace) and NG (blue trace) under CO_2-saturated condition, and 1-Ni@NG under N_2- (red dotted line) and CO_2-saturated condition (red trace) recorded in 0.5 M $NaHCO_3$ solution at the scan rate of 0.05 V/s. (b) Current-time responses for controlled potential electrolysis at -0.67 V vs. RHE for 1 h using carbon paper, NG, and 1-Ni@NG in N_2- and CO_2-containing 0.5 M $NaHCO_3$. (c) Faradaic efficiencies of CO and H_2 and (d) Quantitative analysis of gas products for controlled potential electrolysis for 1 h at -0.67 V vs. RHE in N_2- and CO_2-saturated 0.5 M $NaHCO_3$ solution. Note: CP stands for carbon paper (TGP-H-60) and NG is an abbreviation of nitrogen-doped graphene.

Next, we would like to investigate the control experiment whereby there was no input source of CO_2 in electrochemical setup. Therefore, CPEs were performed in N_2-saturated 0.5 M $NaHCO_3$ solution. Interestingly, we observed the nominal formation of CO with the FE of 25 ± 1% and the primary production of H_2 with the FE of 46 ± 2%. NG itself produced H_2 as the major product and CO as minor product with the FE of 61% and 12%, respectively. The observed small amount of CO production (up to 6 μmol CO) can be attributed to the possible involvement of the HCO_3^-/CO_2 equilibrium as a source of CO_2 for ECR process. It is likely that the HCO_3^- ions present in the electrolyte can serve as an indirect source of CO_2 without the requirement of external supply of CO_2 gas. The observation is consistent with the previous ECR studies using bicarbonate solution as the supporting electrolyte. To subtract the involvement of HCO_3^-/CO_2 equilibrium, bulk electrolysis was tested under N_2-saturated 0.1 M K_2HPO_4/KH_2PO_4 electrolyte. The product quantification in phosphate buffer manifested that only H_2 was produced for NG and 1-Ni@NG electrodes. The control, bare carbon paper electrodes, showed only H_2 production both under N_2- and CO_2-containing 0.5 M $NaHCO_3$ with the comparable FE of 55% and 58%, respectively (**Figure 24c**).

2.8.2 KSCN poisoning experiment – elucidation of active site for ECR

There were previous studies, showing that SCN^- is capable of poisoning most of metal active sites and gave diminishment in their catalytic activity.[84, 85] Thus, in ECR regime, the suppressed ECR activity would be expected once exposed to a plenty of SCN^- in the solution. To investigate that the improved ECR activities in 1-Ni@NG was originally attributed to the Ni active sites, the SCN^- poisoning experiment were experimentally performed in 10 mM KSCN-containing CO_2-saturated 0.5 M $NaHCO_3$ solution (**Figure 25**). Upon addition of KSCN, cyclic voltammograms illustrated that the onset potential was negatively shifted by approximately 60 mV (from -0.57 V to -0.63 V *vs.* RHE)**.** The current times-profiles showed the significant decrease in the total current density from 2.3 to 1.4 mA cm^{-2} during CPE for 1 h in

agreement with the applicable decrease in CO production from 37.8 to 17.6 μmol and the FE from 81% to 69%**.** This result suggested that some of Ni active sites might be debilitated by the binding of SCN^-. With these data in hand, we believed that the superior ECR activities likely originated from the presence of Ni active sites on the surface of electrodes.

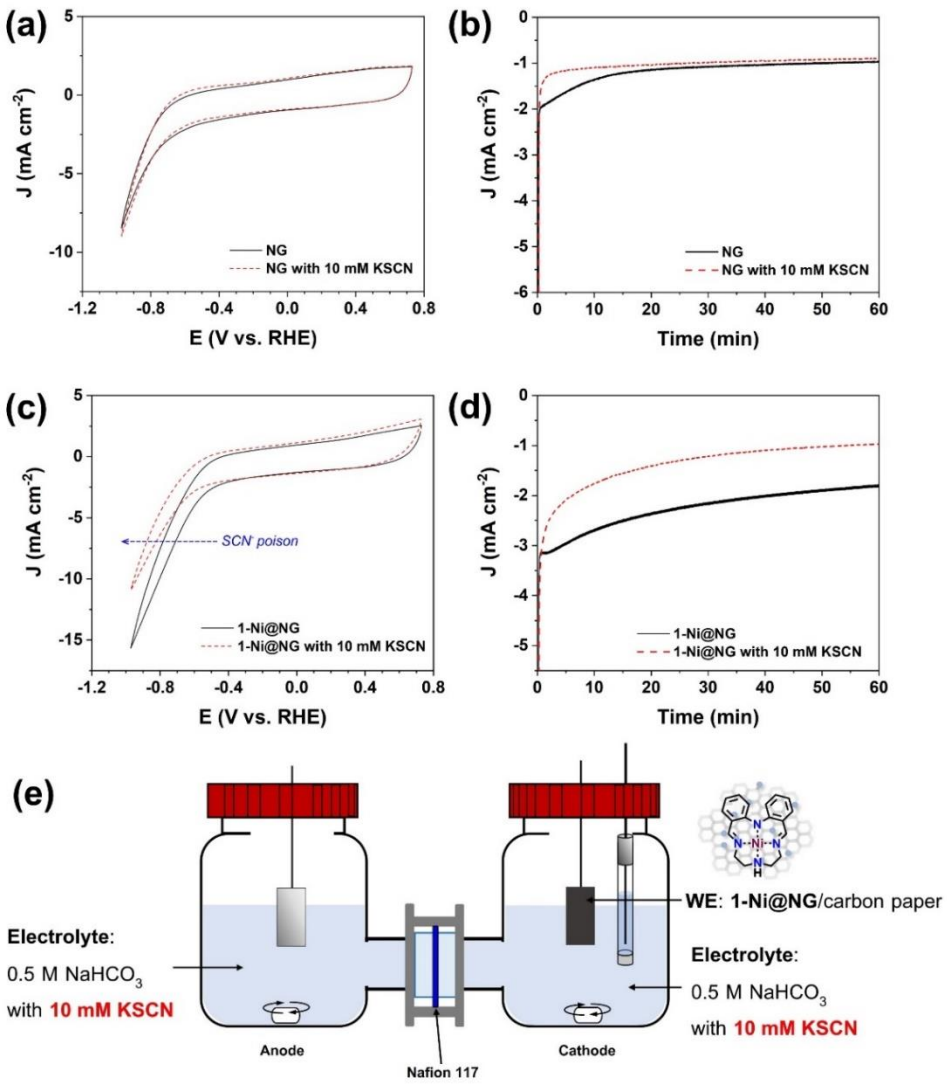

Figure 25 KSCN poisoning experiment. (a) and (c) Cyclic voltammograms of NG and 1-Ni@NG with (red broken line) and without 10 mM KSCN (black solid line) in 0.5 M $NaHCO_3$. (b) and (d) Current-time profiles of NG and 1-Ni@NG with (red dotted line) and without 10 mM KSCN (black dotted line) in 0.5 M $NaHCO_3$. (e) Electrochemical setup for KSCN poison experiment.

2.8.3 Comparison studies of ECR

For this study, the 1-Ni@NG, 2-Ni@NG and $[2\text{-Ni}]^{Me}$@NG were fabricated onto carbon paper electrodes and their constant-potential electrolysis were also carried out at various applied potential ranging from -0.57 V to -0.87 V *vs.* RHE (**Figure 26 and Table 5**). In terms of product selectivity toward ECR, the faradaic efficiency of CO production (FE_{CO}) was used as benchmarking criteria. Over the entire range of applied bias, 1-Ni@NG illustrated the superior reactivity of CO_2-to-CO conversion, of which FE_{CO} is slightly higher than those of 2-Ni@NG. At the peak ECR performance, the faradaic efficiency for CO (FE_{CO}) was measured to be 82% for 1-Ni@NG and 75% for 2-Ni@NG, with an applied potential of -0.67 V vs. RHE and overpotential **(η)** of 0.56 V. While a comparable FE_{CO} could be achieved at -0.77 V vs. RHE, it required a higher overpotential of 0.1 V. Interestingly, performing CPE at -0.87 V vs. RHE resulted in a decrease in FE_{CO} and an increase in FE_{H2}, suggesting that water reduction predominantly occurs at higher overpotential conditions. In the case of $[2\text{-Ni}]^{Me}$@NG, although it displayed a slightly lower activity compared to 1-Ni@NG and 2-Ni@NG, it still exhibited ECR performance. This can be attributed to the absence of N-H functionalities on the ligand, which are important for providing internal H-bonding stabilization of Ni-CO_2 intermediates. These results are supported by CV studies conducted in homogeneous solution, where $[2\text{-Ni}]^{Me}$ showed minimal current enhancement in the presence of CO_2 and H_2O, indicating the significance of N-H functionalities. However, in the aqueous electrolyte, we believe that the effect of N-H functionalities was less pronounced owing to the enriched vicinity of viable hydrogen-bond donors (*i.e.,* H_2O and HCO_3^-) near the electrode surface.[53, 86, 87] The slight drop in ECR activities of $[2\text{-Ni}]^{Me}$@NG compared to 2-Ni@NG was primarily owing to the steric constraint of the methyl substitution. From this observation, we assumed that the N-H functionality is not an absolute requirement for the heterogeneous ECR system. This finding therefore opens an opportunity to

จุฬาลงกรณ์มหาวิทยาลัย
Chulalongkorn University

functionalize at N-H position for future improvement of these nickel complexes as potent ECR electrocatalysts.

In term of product quantification, the amount of CO produced using NG and Ni@NG catalysts was investigated during the constant potential electrolysis for 1 h (**Figure 26**). Specific current density for CO evolution (J_{CO}) is considered as an important marker for justifying the amount of CO produced with respect to the charge passed by during electrolysis. Thus, the higher J_{CO} we observed, the higher ECR products obtained. From results, it was notable that the J_{CO} of 2-Ni@NG was higher than that of 1-Ni@NG and [2-Ni]^{Me}@NG over the range of operational potential. Although the 2-Ni@NG possessed the highest J_{CO}, the lower FE_{CO} was observed when compared to 1-Ni@NG electrode. The ECR performance of Ni@NG catalysts was summarized in **Table 5**.

จุฬาลงกรณ์มหาวิทยาลัย
CHULALONGKORN UNIVERSITY

Table 5 Summary of data in bulk electrolysis for 1 h in a CO_2-saturated 0.5 M $NaHCO_3$ solution (pH 7.4) using Ni@NG catalysts at various applied potential.

Electrode	$E_{applied}$ (V vs. RHE)	Charge (C)	CO (μmol)	%FE(CO)	H_2 (μmol)	%FE(H_2)
1-Ni@NG/CP	-0.57	3.4	11.0	62	5.9	33
	-0.67	8.8	37.8	81	7.2	16
	-0.77	11.6	50.7	84	9.8	16
	-0.87	14.5	53.4	71	18.9	25
2-Ni@NG/CP	-0.57	3.3	10.7	63	6.1	36
	-0.67	10.3	40.6	76	13.7	25
	-0.77	14.7	58.6	77	35.0	23
	-0.87	24.0	77.3	62	44.1	36
[2-Ni]^{Me}@NG/CP	-0.57	2.0	6.2	60	2.5	24
	-0.67	5.4	19.2	68	4.9	18
	-0.77	8.6	29.8	67	9.0	20
	-0.87	14.1	58.2	78	14.2	19

จุฬาลงกรณ์มหาวิทยาลัย
Chulalongkorn University

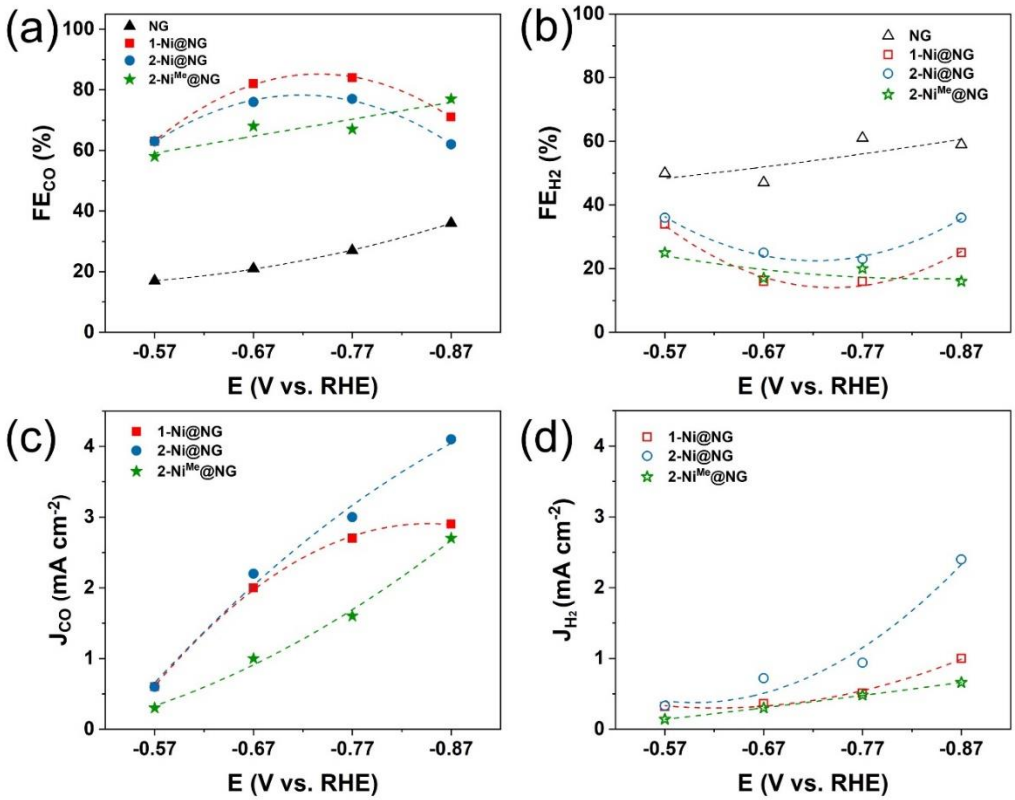

Figure 26 Faradaic efficiencies of (a) CO and (b) H_2, and specific current density of (c) CO production and (d) H_2 evolution at various applied potential from -0.57 V to -0.87 V vs. RHE for 1h-bulk electrolysis in CO_2-saturated 0.5 M $NaHCO_3$.

จุฬาลงกรณ์มหาวิทยาลัย
Chulalongkorn University

2.8.4 Prolonged electrolysis – the stability performance

The prolonged electrolysis experiment was conducted to evaluate the catalytic performance of Ni@NG catalysts at the long-term stability (**Figure 27**). To investigate the prolonged electrolysis of Ni@NG, the electrochemical process was carried out for 4 hours at a potential of -0.67 V vs. RHE. An online gas chromatography (GC) system was utilized to monitor the gas products generated in the headspace of the cathodic chamber. Periodic injections of the gas samples were made every 20 minutes to quantify the time-course production of CO and H_2. The corresponding %FE of CO and H_2 were determined to assess the efficiency of the electrochemical reduction process. During the prolonged electrolysis of 1-Ni@NG, the

chronoamperometric response exhibited a decrease in current density within the first hour, followed by constant current profiles thereafter. Additionally, the FE_{CO} decreased by approximately 10% from 82% to 70% over the course of the electrolysis. Similar behavior was observed for both 2-Ni@NG and $[2\text{-Ni}]^{Me}$@NG catalysts, with a gradual decay in FE_{CO}. For 2-Ni@NG, the FECO decreased from 75% to 60%, while for $[2\text{-Ni}]^{Me}$@NG, it decreased from 67% to 55% during the prolonged electrolysis. These observations suggest that there may be changes in the catalyst or reaction conditions over time, leading to a decrease in the efficiency of CO production. Further investigation is needed to understand the underlying factors contributing to this decrease in faradaic efficiency during prolonged electrolysis. The FE of H_2 production in all cases was increased over time, consistent with the slow drop in FE_{CO}. The cyclic voltammogram before and after electrolysis illustrated the decrease in current density after the catalysts were exposed to the applied potential for 4 h (**Figure S26**). We assumed that the decrease in current density and faradaic efficiency of CO production could be ascribed to catalyst leaching or deactivation during prolonged electrolysis.[74, 88, 89] The imine moieties on our ligand scaffold was assumed to be potentially hydrogenated in the presence of proton source. This may result in the decomposition of metal complexes, and lead to the deposition of nanoparticles that is more favorable for H_2 production.[88, 89] However, we cannot clearly observe the evidence of nanoparticle formation after electrolysis. In addition, the decrease in current density and faradaic efficiency of CO production could be ascribed to catalyst leaching during prolonged electrolysis.[74]

จุฬาลงกรณ์มหาวิทยาลัย
Chulalongkorn University

During the electrolysis process, the amount of CO production increased along with a minor evolution of H_2. This increase in CO production was observed with the accumulation of charge required during the electrolysis. For 1-Ni@NG, the accumulated quantity of CO evolved over 4 hours of electrolysis was 123 μmol. Similarly, for 2-Ni@NG, the accumulated quantity of CO evolved reached 139 μmol over the same duration**.** Turnover frequency (TOF) of 1-Ni@NG was calculated to be

79.2 h^{-1} (or 0.022 s^{-1}) on the basis of the amount of CO produced (123 μmol) and the $\Gamma_{coverage,Ni}$ value (3.9 × 10^{-7} mol cm^{-2}) while TOF of 2-Ni@NG was 133.2 h^{-1} (or 0.037 s^{-1}) (the amount of CO evolved = 139 μmol and the $\Gamma_{coverage,Ni}$ value = 2.6 × 10^{-7} mol cm^{-2}). It should be noted that we calculated our TOF based on $\Gamma_{coverage}$ instead of the typical Γ_{ea} because no distinct peaks of complexes were observed in cyclic voltammetry. This may result in a lower TOF than the number it should be. Even though the Ni@NG catalysts showedd the satisfactory faradaic efficiency for ECR, the current density and TOF were inferior to those of pyrene-functionalized Ni cyclam on carbon nanotubes (J = ~5 mA cm^{-2}, TOF = 4.27 s^{-1}, Γ_{ea} = 5× 10^{-9} mol cm^{-2}).[72]

Although our nickel complexes have demonstrated promising potential for ECR applications, there is still room for improvement. Future efforts in developing these nickel complexes will involve a combination of experimental and computational studies with a focus on structural modifications to enhance their reactivity. Some specific approaches that can be explored include:

1. Studying the effects of different donor atoms on the peripheral unit of the complexes. By varying the donor atoms in the ligand structure, the electronic and steric properties can be tuned to optimize the ECR activity.
2. Introducing substitutions on either the head or peripheral unit of the complexes. Substituents can alter the electronic and steric properties of the complexes, potentially enhancing their catalytic performance.
3. Constructing a rigid head unit, such as a carbazole-based compound, to improve the electronic communication between the metal complexes and carbon supports. This can facilitate efficient charge transfer and enhance the catalytic activity.

These future research directions will contribute to a deeper understanding of the structure-function relationships in these nickel complexes and pave the way for the development of highly efficient electrocatalysts for CO_2 reduction.

จุฬาลงกรณ์มหาวิทยาลัย
Chulalongkorn University

Table 6 Summarized catalytic activity of Ni@NG catalysts for ECR at -0.67 V *vs.* RHE.

Catalysts	Electrolysis Time (h)	Average Current Density (mA cm^{-2})	%FE(CO)	CO (μmol)	TOF (h^{-1})
1-Ni@NG	1[a]	2.2	81	37.8	97.2
	4[b]	2.0	70-82[c]	123.0	79.2
2-Ni@NG	1[a]	3.0	75	40.8	151.2
	4[b]	3.1	62-76[c]	139.0	133.2
$[2\text{-Ni}]^{Me}$@NG	1[a]	1.5	68	19.2	93.6
	4[b]	1.7	55-67[c]	67.8	86.4

[a]Batch experiment. [b]Online experiment. [c]Owing to the change in faradaic efficiency, a range of this value was reported.

จุฬาลงกรณ์มหาวิทยาลัย
Chulalongkorn University

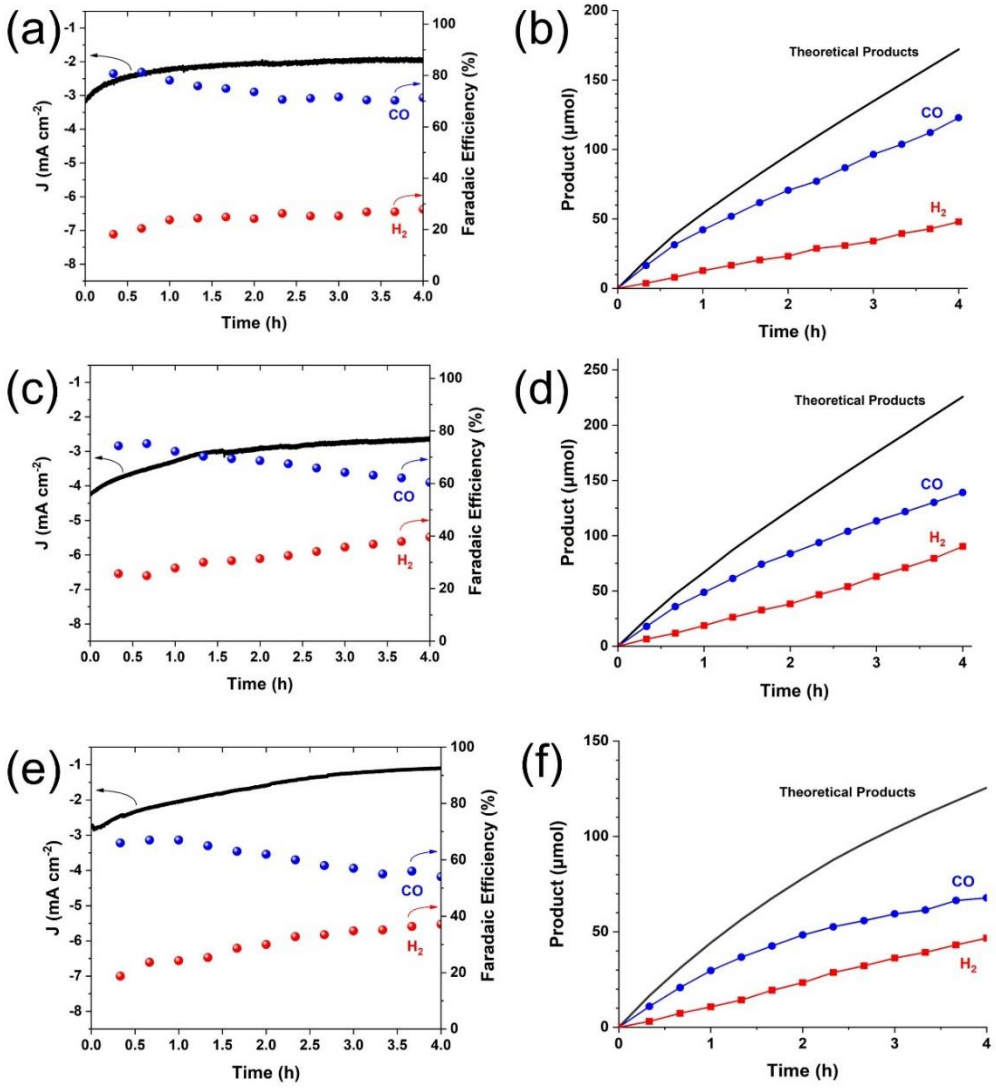

Figure 27 Current-density time profiles and faradaic efficiencies of CO (blue) and H_2 (red) evolution in controlled potential electrolysis at -0.67 V vs. RHE in CO_2-saturated 0.5 M $NaHCO_3$ using (a) 1-Ni@NG, (c) 2-Ni@NG and (e) $[2\text{-Ni}]^{Me}$@NG. Time courses of the moles of CO (blue) and H_2 (red) production from bulk electrolysis and theoretical product yields (black) calculated from $e^-/2$ of charge required during the bulk electrolysis for (b) 1-Ni@NG, (d) 2-Ni@NG and (f) $[2\text{-Ni}]^{Me}$@NG.

CHAPTER 3

AN UNEXPECTED FORMATION OF PENTADENTATE NICKEL(II) COMPLEXES BEARING ACRIDINE-BASED SCHIFF-BASE LIGAND THROUGH THE REARRANGEMENT OF DIPHENYLAMINE

Two isomorphic nickel(II) complexes bearing acridine-based Schiff-base ligand $[NiL^{ACR}](X)_2 \cdot CH_3CN$ (X = BF_4, ClO_4, L^{ACR} = (E)-N^1-(2-((acridin-4-ylmethylene)amino)ethyl)-N^1-(2-aminoethyl)ethane-1,2-diamine) were synthesized through the rearrangement of diphenylamine-2,2'-dicarboxaldehyde head unit. Single crystals of the nickel complexes were achieved after the nickel-mediated condensation in acetonitrile solution with *ca.* 60% yield. X-ray crystallographic analysis reveals that the solid-state structures of these complexes consist of discrete monomeric units $[NiL^{ACR}]^{2+}$, two counter anions, and one lattice acetonitrile molecule. The central Ni(II) ions in each complex adopt a distorted trigonal-bipyramidal geometry with five nitrogen atoms from the L^{ACR} ligand. A pair of symmetry-related $[NiL^{ACR}]^{2+}$ complexes are stacked through face-to-face **π**-**π** interactions exist between acridine moieties of the L^{ACR} ligands to form a supramolecular dimeric structure. The dimers are assembled into a one-dimensional column structure by N–H···F/O hydrogen bonds between the amine groups of the ligands and the counter anions. The columns are interconnected with counter anions and lattice acetonitrile molecules through complementary hydrogen bonding interactions, giving rise to a three-dimensional supramolecular architecture. Furthermore, the electrochemical properties of $[NiL^{ACR}]^{2+}$ complex was preliminary investigated, showing the possibility to utilize this complex for hydrogen evolution reaction (HER).

3.1 Materials and Reagents

All reagents were used as received without further purification unless otherwise stated. Solvents used for syntheses were reagent grade except acetonitrile, which was HPLC grade. 2,2'-iminodibenzoic acid (95%), manganese(IV) oxide (activated, 85%), nickel(II) perchlorate hexahydrate (99%), tris(2-aminoethyl)amine (96%), tetrabutylammonium hexafluorophosphate (98%), and Celite® filter cel (filter aid, slightly calcined) were obtained from Sigma Aldrich. Lithium aluminum hydride (95%) was purchased from TCI. Nickel(II) tetrafluoroborate hexahydrate (99%) were obtained from ACROS. Glassy carbon electrode and non-aqueous $Ag/AgNO_3$ reference electrode were purchased from CH Instrument Inc.

3.2 Instrumentation

Nuclear magnetic resonance (NMR) spectra were recorded on a 500 MHz JEOL at 298 K. UV-vis spectra were recorded on a Varian Cary 50 probe UV-vis spectrophotometer. Elemental analyses (C, H, N) were determined by THERMO FLASH 2000 CHNS/O analyzers. Thermogravimetric analyses (TGA) were carried out with a TGA 55 TA Instrument in the temperature range of 30–800 °C under a nitrogen atmosphere flow with a heating rate of 10 °C min^{-1}. Powder X-ray diffraction (PXRD) measurements were performed on a Bruker D2 Phaser X-ray diffractometer equipped with graphite monochromatized Cu-K_α radiation (λ =1.54056 Å) at 30 kV and 10 mA. Cyclic voltametric measurements were conducted using Metrohm-Autolab (Model PGSTAT101). Conventional three-electrode configuration was used as a standard electrochemical setup where working electrode and reference electrode were glassy carbon electrode (diameter = 0.3 cm, A = 0.071 cm^2) and $Ag/AgNO_3$ (10 mM) electrode, respectively, and platinum wire was used as a counter electrode. The measured potentials were quoted with respect to $AgNO_3/Ag$ electrode and externally calibrated to Fc/Fc^+ redox couple.

3.3 Synthesis of acridine-based Schiff-base Ni(II) complexes

3.3.1 Synthesis of $[NiL^{ACR}](BF_4)_2$

To a bright yellow refluxing solution of diphenylamine-2,2'-dicarboxaldehyde (135 mg, 0.60 mmol) in CH_3CN (10 mL) was added $Ni(BF_4)_2{\cdot}6H_2O$ (204 mg, 0.60 mmol) in CH_3CN (10 mL). Thereafter, a solution of tris(2-aminoethyl)amine (88 mg, 0.60 mmol) in CH_3CN (10 mL) was added dropwise over 20 min. The resulting dark red solution was refluxed for 3 h and ultimately turned to dark brown. The reaction was concentrated under reduced pressure and diethyl ether was diffused to the reaction to yield dark brown block-shaped crystals (205 mg, 56%). Anal. Calc. for $[C_{20}H_{25}B_2F_8N_5Ni]$: C 42.31, H 4.44, N 12.34%. Found: C 42.32, H 4.59, N 12.56%. λ_{max}/nm (ε_{max}/ M^{-1} cm^{-1}) = 291 (8800), 344 (6800), 360 (11000), 387 (6800), 403 (7250).

3.3.2 Synthesis of $[NiL^{ACR}](ClO_4)_2$

To a bright yellow refluxing solution of diphenylamine-2,2'-dicarboxaldehyde (103 mg, 0.46 mmol) in CH_3CN (10 mL) was added $Ni(ClO_4)_2{\cdot}6H_2O$ (167 mg, 0.46 mmol) in CH_3CN (10 mL). (*Caution: perchlorate is potentially explosive, the experiment should be carefully handled*) Thereafter, a solution of tris(2-aminoethyl)amine (57 mg, 0.46 mmol) in CH_3CN (10 mL) was added dropwise over 20 min. The resulting dark red solution was refluxed for 3 h and ultimately turned to dark brown. The reaction was concentrated under reduced pressure and diethyl ether was diffused to the reaction to yield dark brown block-shaped crystals. (176 mg, 61%). Anal. Calc. for $[C_{20}H_{25}Cl_2N_5NiO_8]$: C 40.51, H 4.25, N 11.81%. Found: C 40.55, H 4.33, N 12.12%. λ_{max}/nm (ε_{max}/ M^{-1} cm^{-1}) = 291 (9100), 344 (7000), 360 (11500), 387 (7100), 403 (7500).

3.4 X-ray crystallography

Suitable crystals of complexes $[NiL^{ACR}](BF_4)_2$ and $[NiL^{ACR}](ClO_4)_2$ were mounted on MiTeGen micromounts using paratone oil. X-ray diffraction data were collected using a Bruker D8 Quest Cmos Photon II operating at T = 296(2) K. Data were collected using **ω** and **φ** scans and using Mo-K**α** radiation (**λ** = 0.71073 Å). The total number of runs and images was based on strategy calculation from the program APEX3 and unit cell indexing was refined using SAINT. Data reduction was performed using SAINT and SADABS were used for absorption correction. The integrity of the symmetry was checked by using PLATON.[90] The structure was solved with the ShelXT structure solution program using combined Patterson and dual-space recycling methods.[91] The structure was refined with a full-matrix least squares on F^2 using ShelXL[92] and OLEX2.[93] In the final refinement cycles, all non-hydrogen atoms were refined anisotropically. The hydrogen atoms were introduced in calculated positions and refined with fixed geometry and riding thermal parameters with respect to the carrier atoms. A summary of the crystal data and relevant refinement parameters is presented in **Table 7** Crystal data and structural refinement for $[NiL^{ACR}](BF_4)_2$ and $[NiL^{ACR}](ClO_4)_2$. CCDC 2130819 ($[NiL^{ACR}](BF_4)_2$) and 2130820 ($[NiL^{ACR}](ClO_4)_2$), contain the supplementary crystallographic data for this study. These data can be obtained free of charge from Cambridge Crystallographic Data Centre via www.ccdc.cam.ac.uk/data_request/cif.

จุฬาลงกรณ์มหาวิทยาลัย
CHULALONGKORN UNIVERSITY

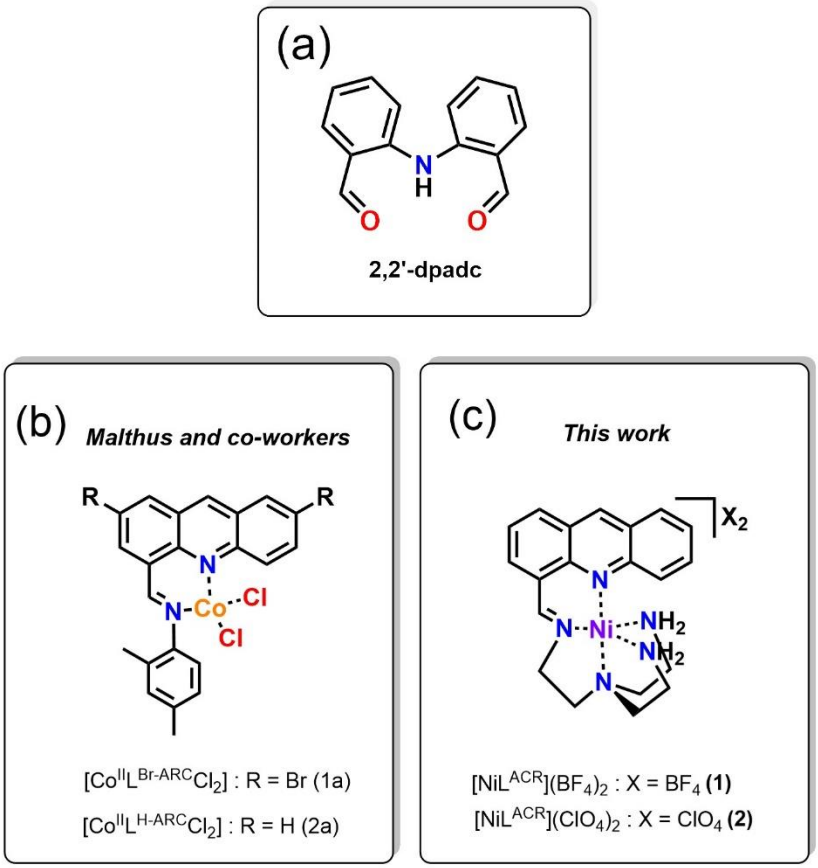

Figure 28 (a) Structural motif of diphenylamine-2,2'-dicarboxaldehyde, and (b) acridine-based cobalt (II) complexes rearranged from diphenylamine-based precursor.[94] (c) Nickel (II) complexes bearing Schiff-base acridine-based ligand in this work.

จุฬาลงกรณ์มหาวิทยาลัย
Chulalongkorn University

3.5 Structural descriptions and properties of acridine-based nickel(II) complexes

The nickel(II) complexes were synthesized by templated [1+1] Schiff base condensation between 2,2'-iminobisbenzaldehyde and tris(2-aminoethyl)amine in the presence of hydrated perchlorate or tetrafluoroborate salts of nickel(II). To begin with, the thermal properties of $[NiL^{ACR}](BF_4)_2$ was investigated and exhibited quite high thermal stability up to 400 °C as a representative example (**Figure 29**). It is noted that $[NiL^{ACR}](ClO_4)_2$ was not subjected to thermal stability test owing to the

harmfulness of perchlorate salt – potentially explosive under heating at high temperature. X-ray quality crystals were obtained by slow diffusion of diethyl ether into the solution of complexes in acetonitrile. The single crystal X-ray diffraction analyses revealed that $[NiL^{ACR}](BF_4)_2$ and $[NiL^{ACR}](ClO_4)_2$ are isostructural and crystallize in the centrosymmetric triclinic system with space group *P*-1. The asymmetric unit consists of one crystallographic unique nickel(II) ion, two counter anions, and one lattice acetonitrile molecule. The molecular structure of cationic species of the complex is shown in **Figure 30**. The central nickel(II) ion is five-coordinated with a distorted trigonal bipyramidal geometry surrounded by five nitrogen atoms from the ligand, in which N1 and N3 atoms occupy the axial positions, while three basal positions being taken up by N2, N4, and N5 atoms. The Ni–N bond lengths are in the range of 1.957(2)-2.110(2) for $[NiL^{ACR}](BF_4)_2$ and 1.967(2)-2.115(2) Å for $[NiL^{ACR}](ClO_4)_2$ (**Table S11**), which are comparable to those reported in other related nickel(II) complexes.[95-97]

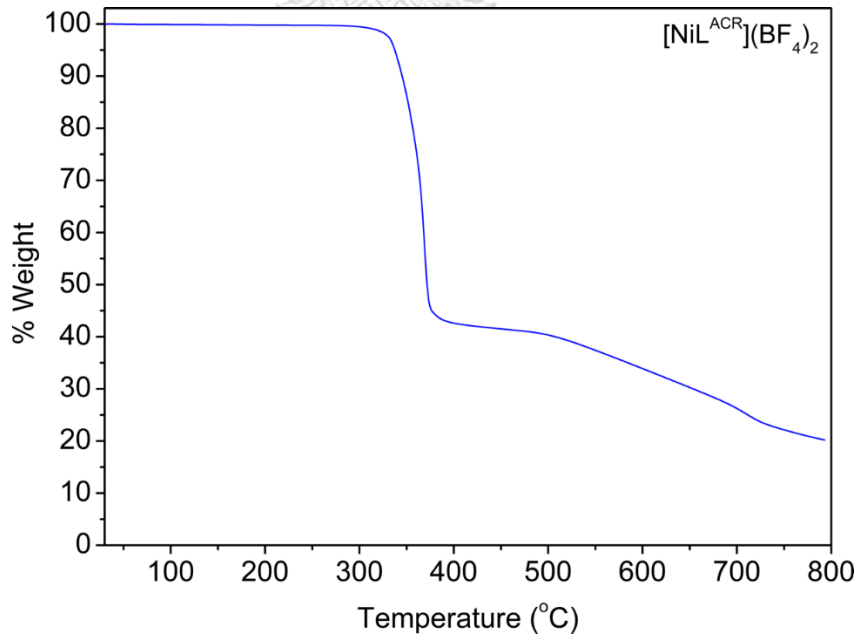

Figure 29 Thermogravimetric analysis curve of $[NiL^{ACR}](BF_4)_2$

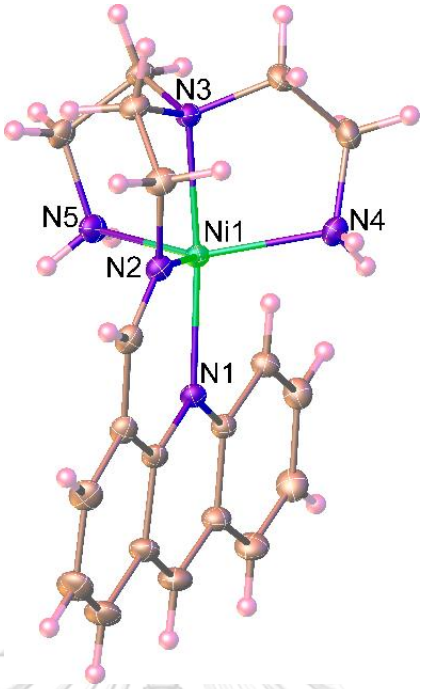

Figure 30 ORTEP diagram of $[NiL^{ACR}]^{2+}$ showing the coordination environment for nickel(II) atom. The atoms are represented by 50% probability thermal ellipsoids.

A close inspection of the crystal structure discloses that a pair of symmetry-related $[NiL^{ACR}]^{2+}$ complexes are stacked through face-to-face **π-π** interactions exist between acridine moieties of the L^{ACR} ligands to from a supramolecular dimeric structure (centroid-to-centroid distances = 3.865(3)–3.924(3) Å for $[NiL^{ACR}](BF_4)_2$, 3.866(2)–3.921(2) Å for $[NiL^{ACR}](ClO_4)_2$). The dimers are assembled into a one-dimensional column structure by N–H···F/O hydrogen bonds between the amine groups of the ligands and the counter anions (**Figure 31**). Ultimately, the columns are interconnected with counter anions and lattice acetonitrile molecules through complementary N–H···F/O and C–H···F/O hydrogen bonding interactions, giving rise to a three-dimensional supramolecular architecture. Details of the hydrogen bonding geometry for the complexes $[NiL^{ACR}](BF_4)_2$ and $[NiL^{ACR}](ClO_4)_2$ are given in **Table S11-S13**.

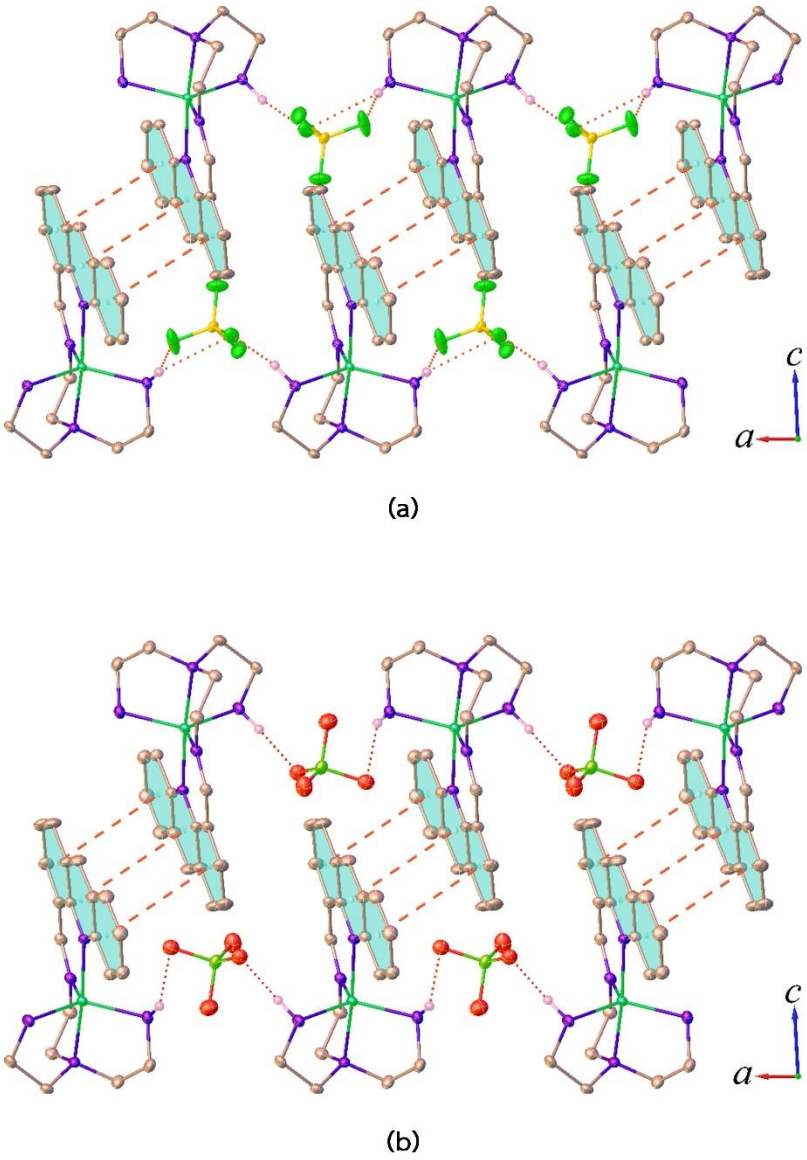

Figure 31 Perspective views of the one-dimensional column structures forming by the complementary hydrogen bonding and **π-π** stacking interactions in (a) $[NiL^{ACR}](BF_4)_2$ and (b) $[NiL^{ACR}](ClO_4)_2$.

Table 7 Crystal data and structural refinement for $[NiL^{ACR}](BF_4)_2$ and $[NiL^{ACR}](ClO_4)_2$

Compound	**$[NiL^{ACR}](BF_4)_2$**	**$[NiL^{ACR}](ClO_4)_2$**
Empirical Formula	$C_{22}H_{28}N_6B_2F_8Ni$	$C_{22}H_{25}Cl_2N_6NiO_8$
Formula Weight	608.83	634.11
Temperature (K)	296(2)	296(2)
Wavelength (Å)	0.71073	0.71073
Crystal System	triclinic	Triclinic
Space Group	*P*-1	*P*-1
a (Å)	8.2720(3)	8.3309(3)
b (Å)	10.0320(3)	10.1513(3)
c (Å)	16.1128(5)	16.2660(5)
α (°)	86.663(1)	86.568(1)
β (°)	87.204(1)	86.593(1)
γ (°)	84.311(1)	83.398(1)
V (Å^3)	1327.03(7)	1362.12(8)
Z	2	2
ρ_{calc} (g/cm^3)	1.524	1.546
μ (mm^{-1})	0.81	0.965
Reflns collected/unique	46995/6601	37998/6762
GOF on F^2	1.017	1.049
R_{int}, R_{sigma}	0.078, 0.0457	0.0269, 0.0175
R_1, wR_2 [$I > 2\sigma(I)$]	0.0451, 0.0909	0.0501, 0.1446
R_1, wR_2 (all data)	0.0770, 0.1047	0.0561, 0.1512
Max./min. residual (e Å^{-3})	0.49/−0.29	0.89/−0.68
CCDC No.	2130820	2130819

จุฬาลงกรณ์มหาวิทยาลัย
Chulalongkorn University

3.6 Plausible Mechanism of Acridine-Based Complex Formation

It was previously reported that the diphenylamine-based Schiff-based Ni(II) macrocycles could be synthesized by nickel-templated [1+1] Schiff-base condensation.[75, 76] With the similar head motif (*i.e.*, 2,2'-dpadc), we thus initially expected to obtain penta-coordinated Schiff-base Ni(II) macrocycles through this synthetic strategy. However, the crystallographic data disclosed that the structure of complexes was sterically favorable for the rearrangement of 2,2'-dpadc unit to achieve acridine-based Schiff-base complexes. An unexpected formation of acridine-based nickel Schiff-base complex was achieved through nickel-promoted condensation (**Figure 32**). Our proposed mechanism was that the acridine formation was proceeded after the imine condensation of one arm of 2,2'-dpadc. Firstly, 2,2'-dpadc was reacted with tris(2-aminoethyl) amine *via* Schiff base condensation, resulting in one imine arm. Secondly, the imine arm was activated by nickel, providing more electrophilicity of carbon atoms in the imine functional group which hereafter underwent a 6-membered cyclization. Thereafter, a couple of deprotonations took place to rearomatize and provided acridine moiety with a pendant carbonyl arm meanwhile releasing nickel salt and tris(2-aminoethyl) amine back into the solution. The carbonyl-dangling acridine and tris(2-aminoethyl) were further subjected to nickel-templated Schiff base condensation to ultimately produce acridine-based Schiff-base Ni(II) complexes. Our attempts toward the choice of nickel precursors (*i.e.*, $Ni(BF_4)_2$ and $Ni(ClO_4)_2$) showed similar structural configuration once formed in complexes. This directly indicates that the different anions in metal precursors do not influence the geometry of complexes. Likewise, Malthus and co-workers suggested that the diphenylamine-based Co(II) complex, the diphenylamine motif of which was preserved, could be synthesized through two steps: 1)

preparation of Schiff base ligand followed by 2) complexation with $CoCl_2$ in the presence of *tert*-butoxide base.[94] Since our nickel complexes comprise of the identical head unit, they potentially could be also synthesized through the similar chemistry of which previously reported by Malthus to obtain the penta-coordinated Schiff-based Ni(II) macrocycles with 2-aminoethyl pendant arms.

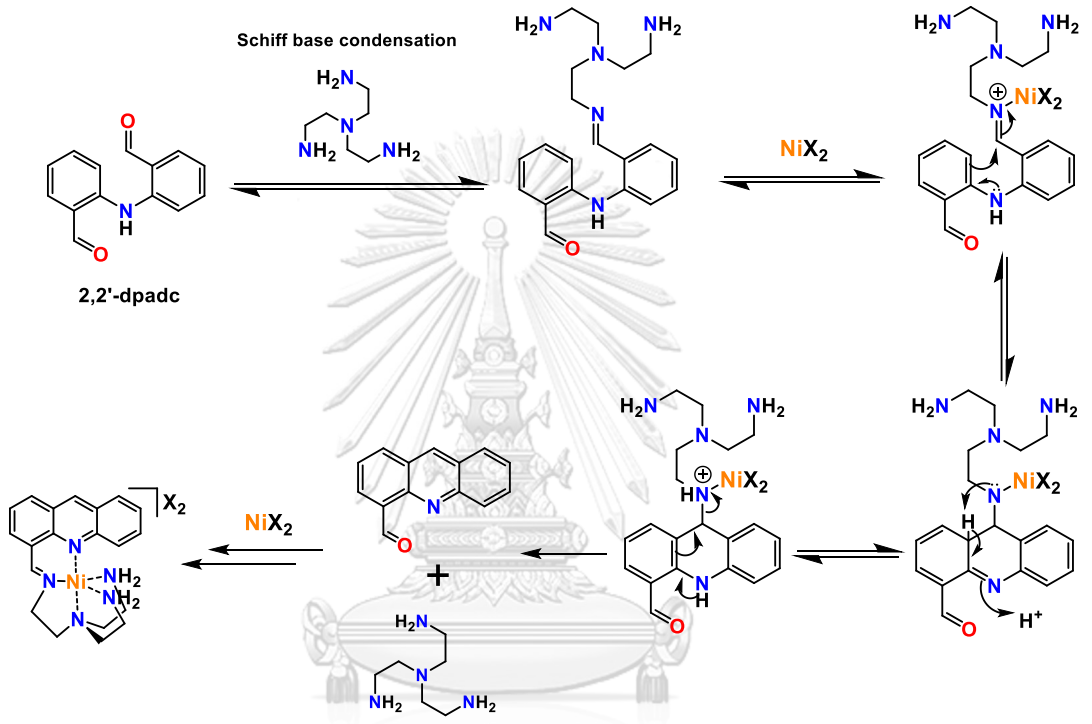

Figure 32 Plausible mechanism of nickel-mediated acridine-based ligand formation

จุฬาลงกรณ์มหาวิทยาลัย
Chulalongkorn University

3.7 UV-visible adsorption profiles of acridine-based nickel(II) complexes

UV-vis spectroscopy of two nickel complexes illustrated the identical absorption consistent with their similar structure in the solid state (**Figure 33**). The existence of acridine moiety was confirmed by the absorption band featured at *ca.* 360 nm which was assigned to the adsorption of the acridine moiety in the complexes.[98] $[NiL^{ACR}](BF_4)_2$ and $[NiL^{ACR}](ClO_4)_2$ exhibited the identical absorption peaks at 291, 344, 360, 387, and 403, corresponding to n-to-**π*** and **π**-to-**π*** transition. It was noted that no d-d transition hump was clearly observed in the visible region, probably could be either masked by the intense absorption of the ligand or

attributed to much lower absorptivity with respect to that of the ligand. UV-vis spectrum of 2,2'-dpadc revealed the absorption peaks at 230, 251, 296, 343, and 403 nm. Obviously, no strong absorption band featured at *ca.* 360 nm owing to the lack of the acridine moiety in the original motif. This confirmed that the peak at 360 nm in the complexes has arisen according to the acridine formation.

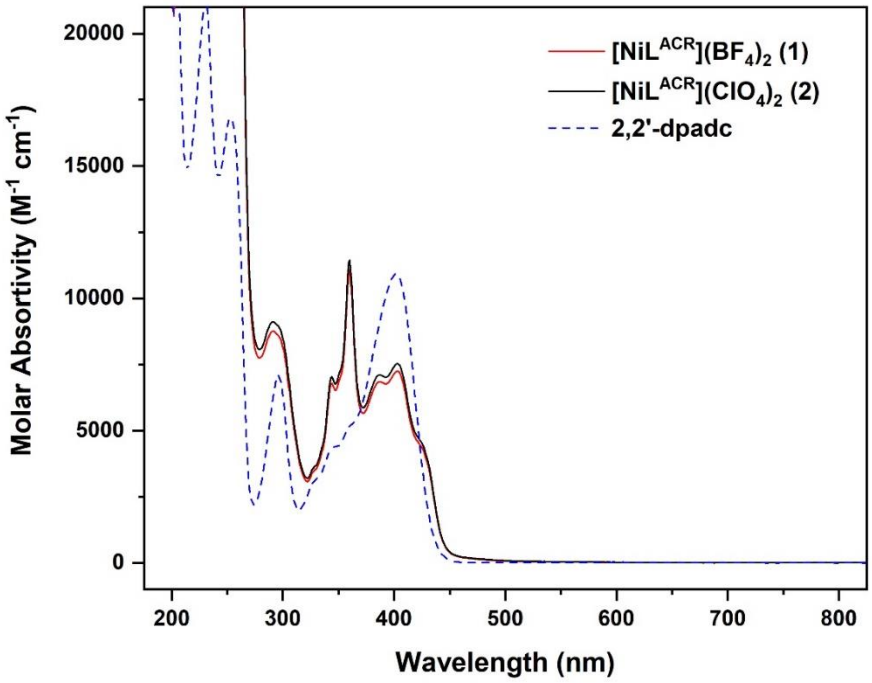

CHULALONGKORN UNIVERSITY

Figure 33 UV-vis spectroscopic characterization of 0.1 mM $[NiL^{ACR}](BF_4)_2$ (red trace) $[NiL^{ACR}](ClO_4)_2$ (black trace), and 2,2'-dpadc in acetonitrile solution (dashed blue trace).

3.8 Electronic properties and preliminary observation toward electrocatalytic H_2 production

Cyclic voltametric measurements of nickel complexes were conducted in N_2-saturated acetonitrile solution containing 0.1 M tetrabutylammonium hexafluorophosphate (**Figure 34a**). The cyclic voltammogram of $[NiL^{ACR}](BF_4)_2$ exhibits

an irreversible process at E = -1.28 V vs. $Fc^{0/+}$ and a quasi-reversible process at $E_{1/2}$ = *ca.* -2.05 V vs. $Fc^{0/+}$ for reduction events ($E_{red,1}$ and $E_{red,2}$), respectively. Moreover, increasing the scan rate resulted in higher observed current density (**Figure 34b**).

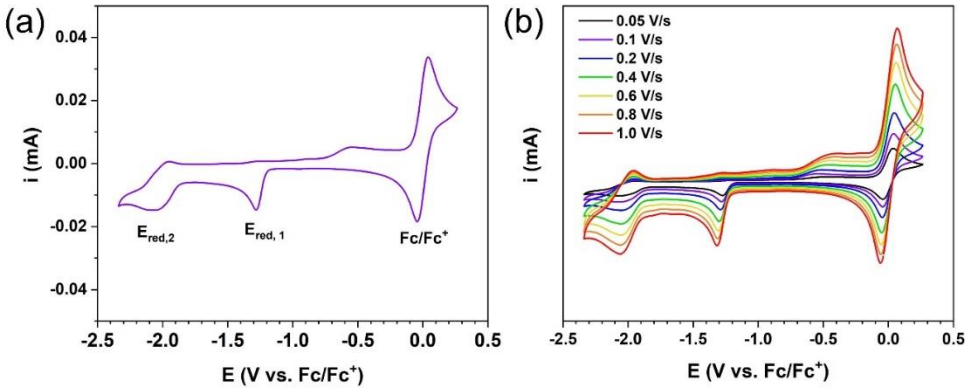

Figure 34 (a) CVs of $[NiL^{ACR}](BF_4)_2$ in N_2-saturated 0.1 M NBu_4PF_6/DMF at scan rate of 0.1 V/s and (b) at different scan rate. Ferrocene (Fc) was used as internal redox standard ($E_{1/2}$ = 0.09 V ± 0.01 V vs. 0.01 M $AgNO_3$/Ag).

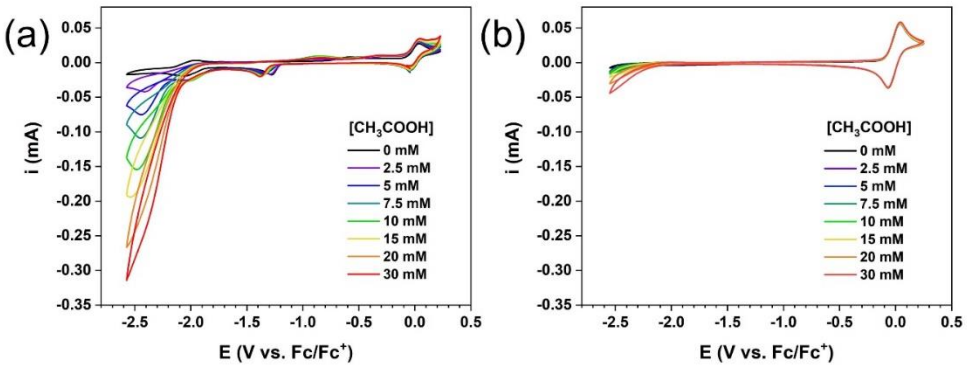

Figure 35 CVs of (a) $[NiL^{ACR}](BF_4)_2$ and (b) blank in N_2-saturated 0.1 M NBu_4PF_6/DMF in the presence of 0-30 mM CH_3COOH.

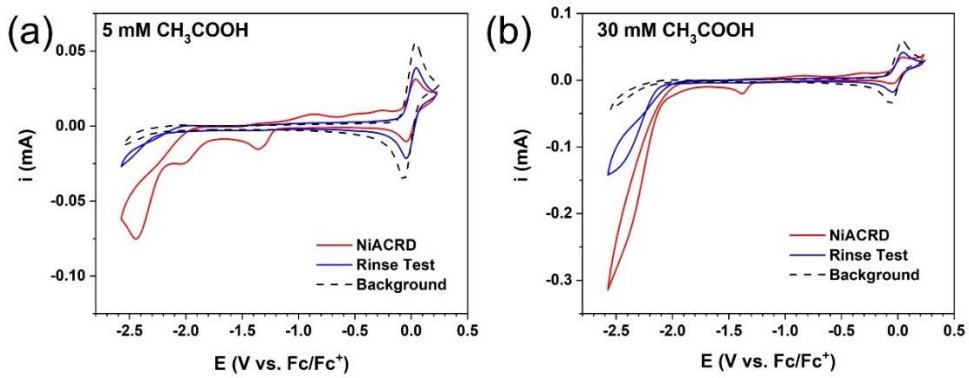

Figure 36 CVs of $[NiL^{ACR}](BF_4)_2$ in N_2-saturated 0.1 M NBu_4PF_6/DMF in the presence of CH_3COOH (red trace) and after rinse test (blue trace) and blank signal (dashed line)

To preliminary investigate electrocatalytic hydrogen production, CVs were conducted in N_2-saturated 0.1 M NBu_4PF_6/DMF. Upon the addition of CH_3COOH, the current enhancement was observed. Interestingly, onset potential and pre-wave peaks were observed at more positive potential, followed by catalytic response at $E_{1/2}$ = -2.46 V vs. Fc/Fc^+ upon addition of acid in the electrolyte. For the control experiment, the blank without catalyst showed a much lower current enhancement (**Figure 35**). This could suggest that 0.1 M NBu_4PF_6/DMF electrolyte is an appropriate solvent choice for HER. Owing to the presence of pre-wave, we performed the rinse test experiment to investigate if heterogeneous species evolved upon addition of acid. The result showed that after rinsing the electrode with fresh DMF solvent, there are no pre-wave peaks though observed current enhancement (**Figure 36**). The current enhancement after rinse test was lower than that of the presence of catalyst, $[NiL^{ACR}](BF_4)_2$; however, higher than background signal. This result implies the heterogeneous catalysis should be involved by the surface-adsorbed species.

Controlled potential electrolysis was performed under N_2-saturated 0.1 M NBu_4PF_6/DMF electrolyte with the additive of 30 mM CH_3COOH to investigate

จุฬาลงกรณ์มหาวิทยาลัย
CHULALONGKORN UNIVERSITY

hydrogen production. The electrochemical performance of $[NiL^{ACR}](BF_4)_2$ was evaluated in comparison to the control experiment: $Ni(BF_4)_2{\cdot}6H_2O$ and without catalysts. The results showed that $[NiL^{ACR}](BF_4)_2$ has the faradaic efficiency for H_2 evolution (FE_{H2}) of 40% at the applied potential of -2.3 V vs. $Fc^{+/0}$. $Ni(BF_4)_2{\cdot}6H_2O$ and blank condition were investigated as control, showing slightly lower FE_{H2} of 35% and 32%, respectively. However, $[NiL^{ACR}](BF_4)_2$ has higher charge and amount of H_2 (*i.e.*, 7.6 C and 16.0 μmol) in comparison to those of $Ni(BF_4)_2{\cdot}6H_2O$ and blank. At the applied potential of -2.1 V vs. $Fc^{+/0}$, the FE_{H2} was not significantly different from -2.3 V vs. $Fc^{+/0}$. However, the charge accumulation and the amount of H_2 production was quite different, those at -2.1 V vs. $Fc^{+/0}$ illustrated lower compared to at -2.3 V vs. $Fc^{+/0}$. The data of electrochemical H_2 evolution was summarized in **Table 8** and the charge build-up profiles at two different applied potentials were illustrated in **Figure 37**.

จุฬาลงกรณ์มหาวิทยาลัย
CHULALONGKORN UNIVERSITY

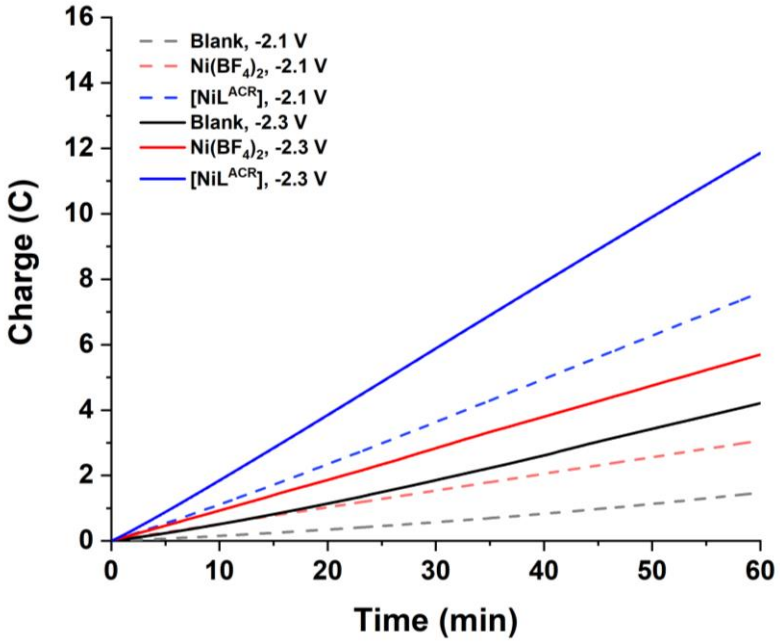

Figure 37 Charge build-up profiles during bulk electrocatalysis for 1 h at -2.1 V (broken line) and -2.3 V vs. $Fc^{+/0}$ (solid line).

Table 8 Summarized data for electrochemical hydrogen production using $[NiL^{ACR}](BF_4)_2$

Condition	$E_{applied}$	%FE(H_2)	Charge / C	H_2 / μmol
Blank	-2.1 V vs. Fc/Fc^+	32	1.5	2.5
$Ni(BF_4)_2$		30	3.1	4.5
$[NiL^{ACR}](BF_4)_2$		40	7.6	16.0
Blank	-2.3 V vs. Fc/Fc^+	32	4.2	7.8
$Ni(BF_4)_2$		35	5.9	11.0
$[NiL^{ACR}](BF_4)_2$		40	11.8	24.4

จุฬาลงกรณ์มหาวิทยาลัย
Chulalongkorn University

CHAPTER 4

CONCLUSION

Three nickel complexes containing N_4-Schiff base macrocycles (1-Ni, 2-Ni, and [2-Ni]^{Me}) derived from diphenylamine-2,2'-dicarboxaldehyde were synthesized and electrochemically investigated to examine the electrochemical CO_2 reduction (ECR) activity. The catalytic response of 1-Ni and 2-Ni was observed upon sparging CO_2 into solution, suggesting that the complexes are potentially active toward CO_2 reduction. In contrast, [2-Ni]^{Me} virtually remain peak-shaped in the exposure of CO_2. For heterogeneous ECR in aqueous electrolyte, three synthesized nickel complexes were immobilized onto nitrogen-doped graphene (Ni@NG) *via* non-covalent **π-π** interaction using the assistance of sonication. The as-prepared Ni@NG were characterized by SEM-EDS, ICP-OES, and electrochemical measurements. In CO_2-saturated bicarbonate solution, three hybrid Ni@NG catalysts showed satisfactory ECR reactivity with the faradaic efficiency of CO production up to 80% and the modest current density of 2-3 mA cm^{-2} at the overpotential of 0.56 V *vs.* RHE. Interestingly, the methyl substitution in [2-Ni]^{Me} did not significantly influence the ECR activities compared to its counterpart, highlighting that these nickel complexes are allowed to modification on their peripheral unit at the N-H position to further fine-tune their electrochemical properties and ECR activities. All in all, our new materials Ni@NG have been demonstrated to be a promising candidate for ECR which being active toward CO_2 reduction over water reduction. Future prospects for development of these nickel complexes could be as follows: (1) to study the effect of donor atoms on the peripheral moiety (2) to introduce the substitution on either the head or peripheral unit (3) to render the more rigid carbazole-based head unit for improved electron passageway of metal complexes and carbon-based supports.

จุฬาลงกรณ์มหาวิทยาลัย
Chulalongkorn University

A parallel work demonstrated that an unexpected formation of pentadentate nickel(II) complexes bearing acridine-based Schiff-base ligand, named as $[NiL^{ACR}](X)_2 \cdot CH_3CN$ where X = BF_4^- and ClO_4^- were synthesized *via* a nickel-templated [1+1] imine condensation between diphenylamine-2,2'-dicarboxaldehyde and tris(2-aminoethyl)amine. Single crystals of $[NiL^{ACR}](X)_2 \cdot CH_3CN$ could be obtained by slowly diffusing diethyl ether to CH_3CN layer, giving *ca.* 60% yield of the complexes. The nickel(II) complexes were examined for their electrochemical properties and catalytic H_2 evolution activity in tetrabutylammonium hexafluorophosphate (Bu_4NPF_6)/dimethyl formamide (DMF). The catalytic H_2 evolution when using $[NiL^{ACR}]^{2+}$ as catalysts illustrated a slightly higher faradaic efficiency and amount of H_2 production when compared to the control – $Ni(BF_4)_2 \cdot 6H_2O$ and blank solution. Though the electrochemical performance of $[NiL^{ACR}]^{2+}$ complex was preliminary investigated toward H_2 evolution reaction, yet the catalytic performance can be further improved and optimized in many other aspects including the choice of proton sources and metal active centers. Alternatively, studying the nature of active Ni species of H_2 evolution for this class of Ni complex would help to understand how to improve their reaction kinetics. In another aspect, although the electrochemical setup might be more complicated, pairing up H_2 evolution at cathode with the appropriate oxidation reaction at anodic compartment may enhance the rate of H_2 evolution to the certain extent as well.

จุฬาลงกรณ์มหาวิทยาลัย
CHULALONGKORN UNIVERSITY

APPENDIX

จุฬาลงกรณ์มหาวิทยาลัย
Chulalongkorn University

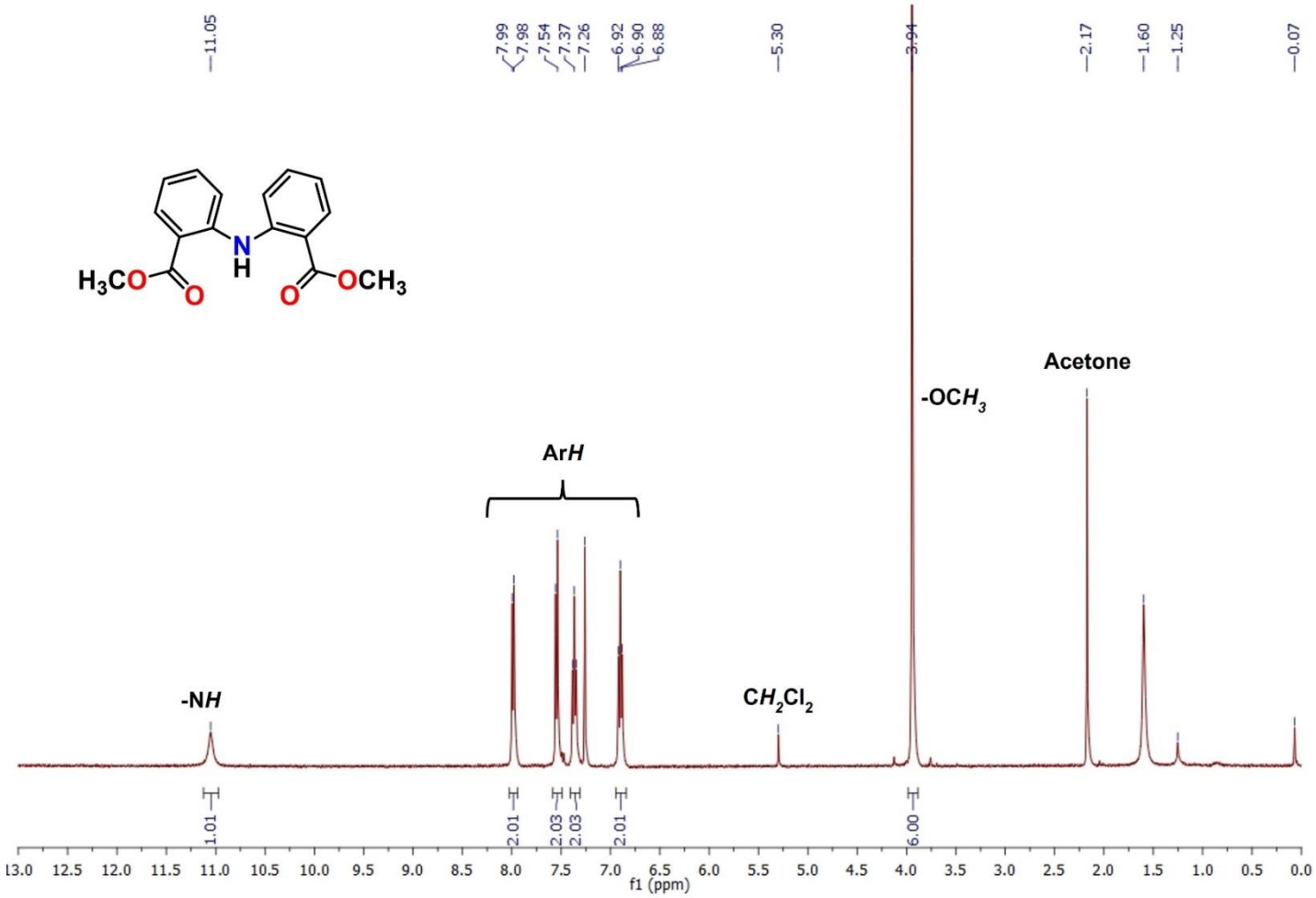

Figure S1 ^{1}H NMR spectrum of 2,2'-iminobis(methyl benzoate) in $CDCl_3$.

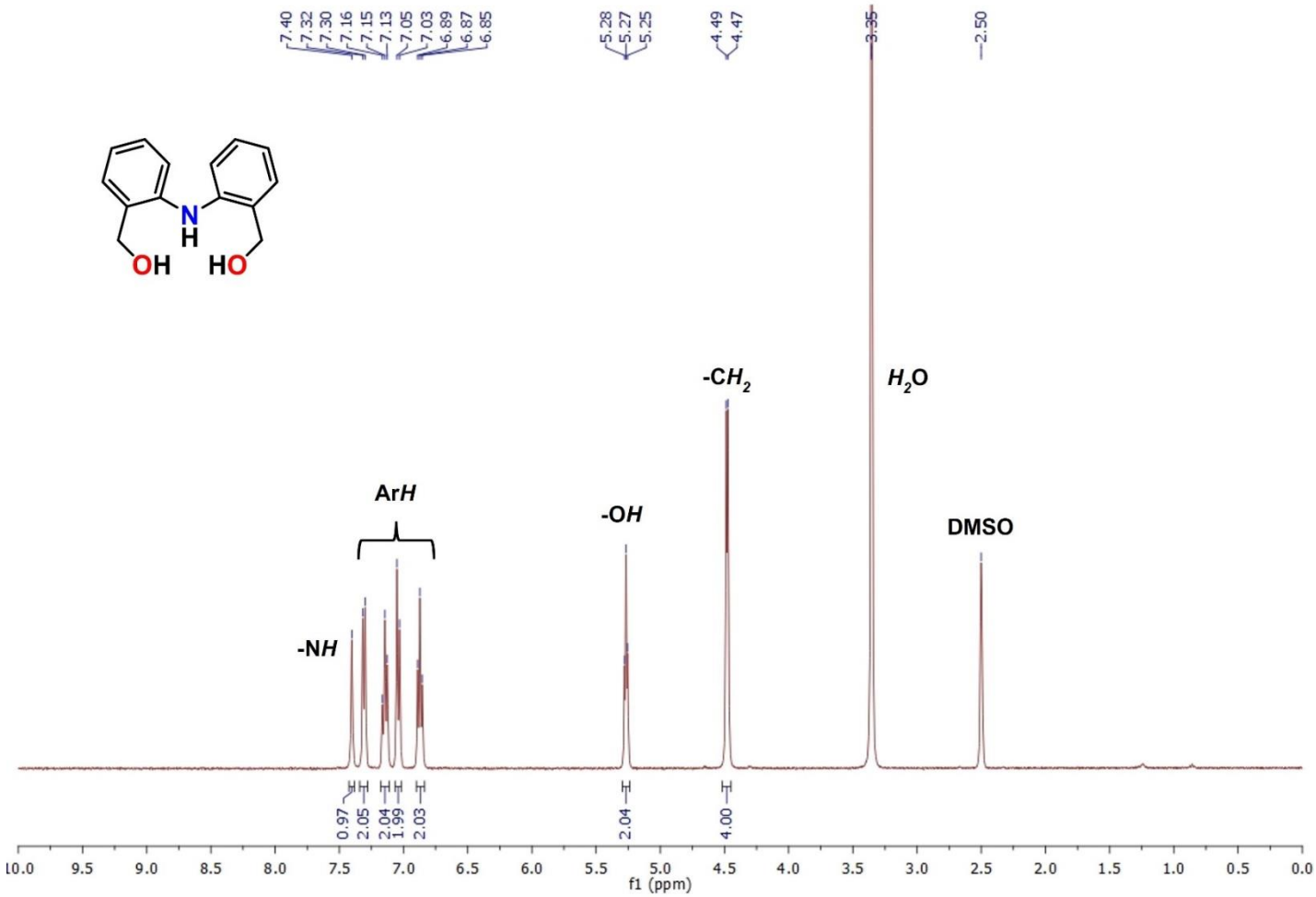

Figure S2 ^{1}H NMR spectrum of 2,2'-iminobis(hydroxymethyl benzene) in DMSO-d_6.

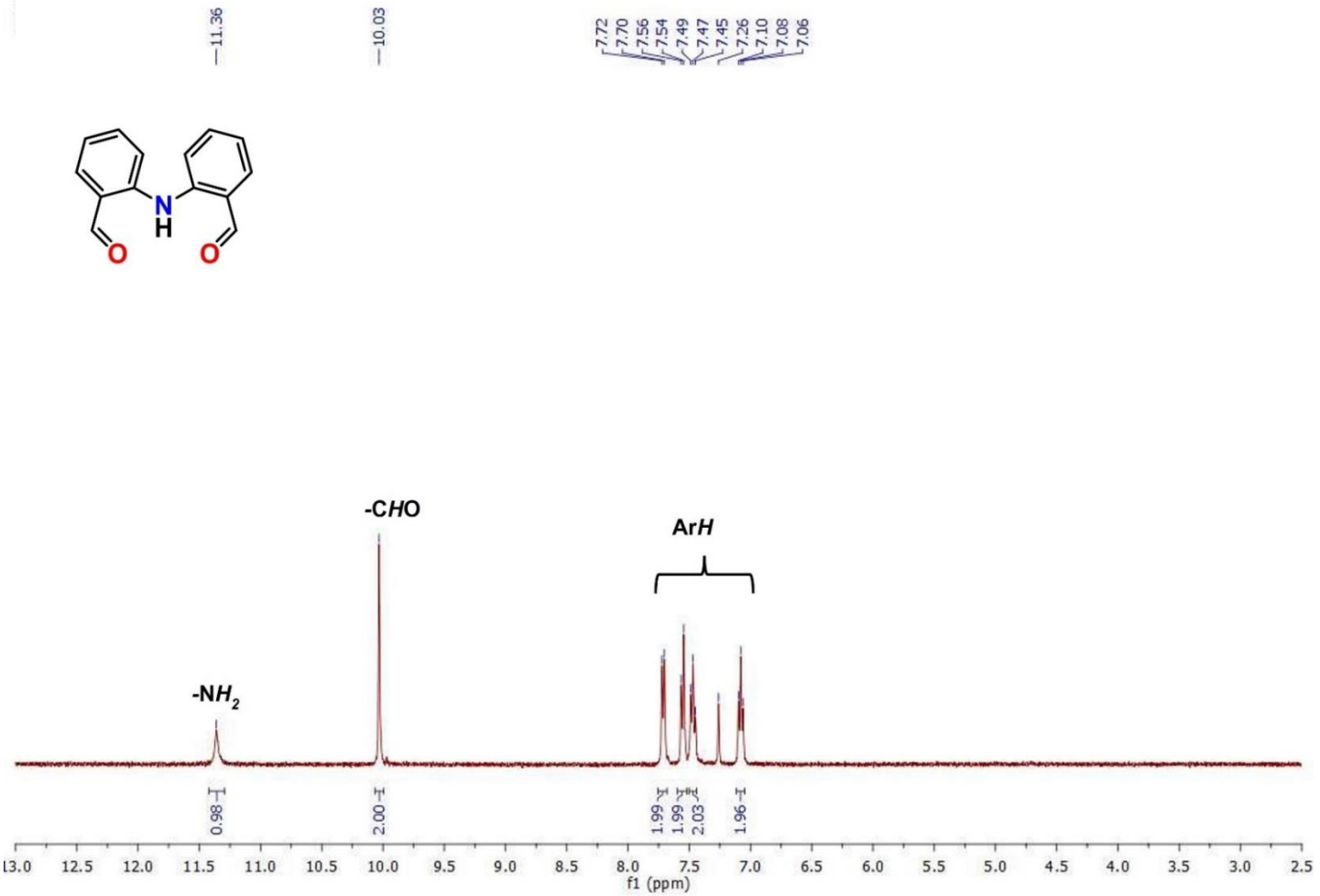

Figure S3 ^{1}H NMR spectrum of diphenylamine-2,2'-dicarboxaldehyde in $CDCl_3$.

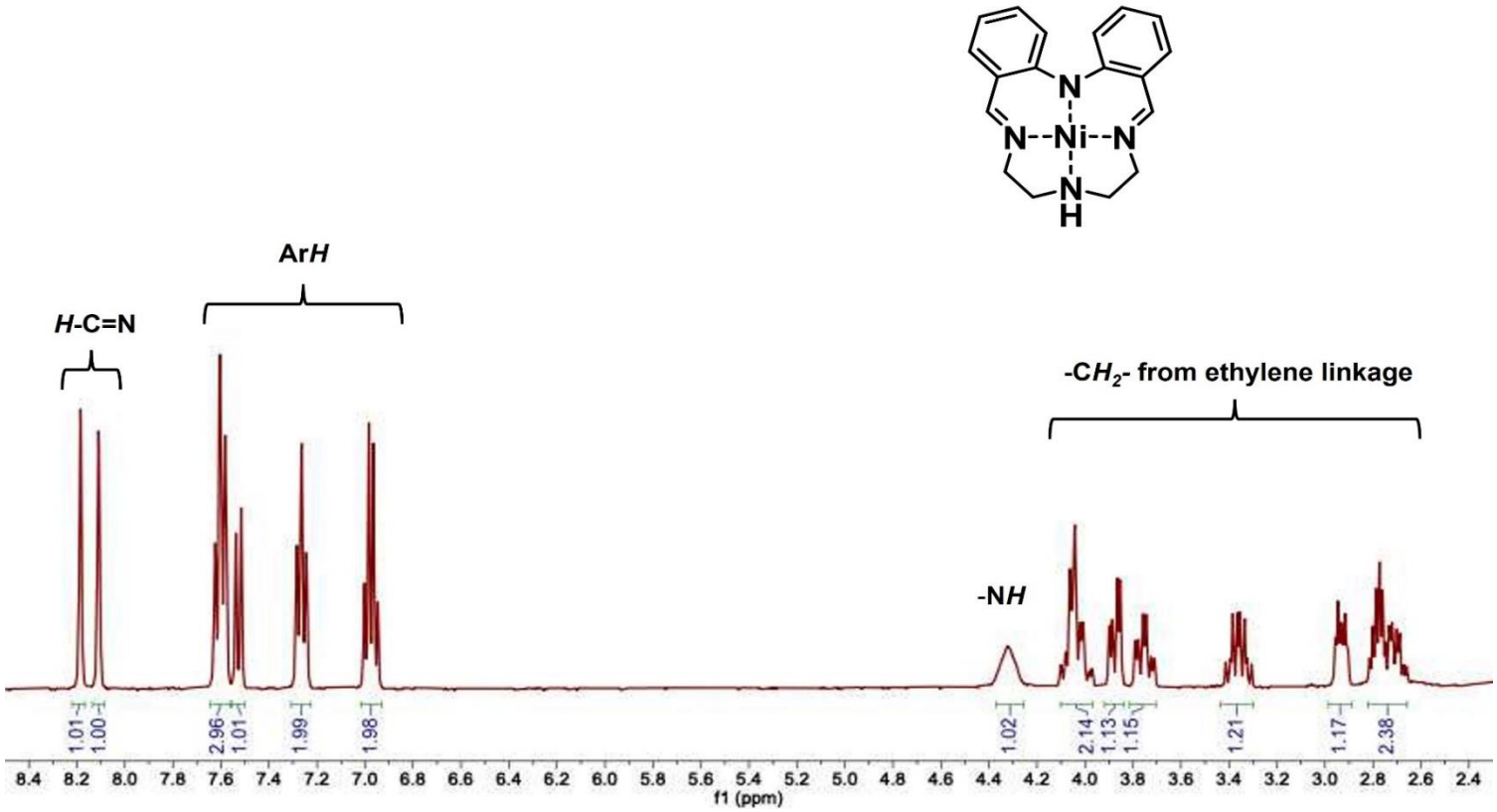

Figure S4 ^{1}H NMR spectrum of [1-Ni](BF$_4$)

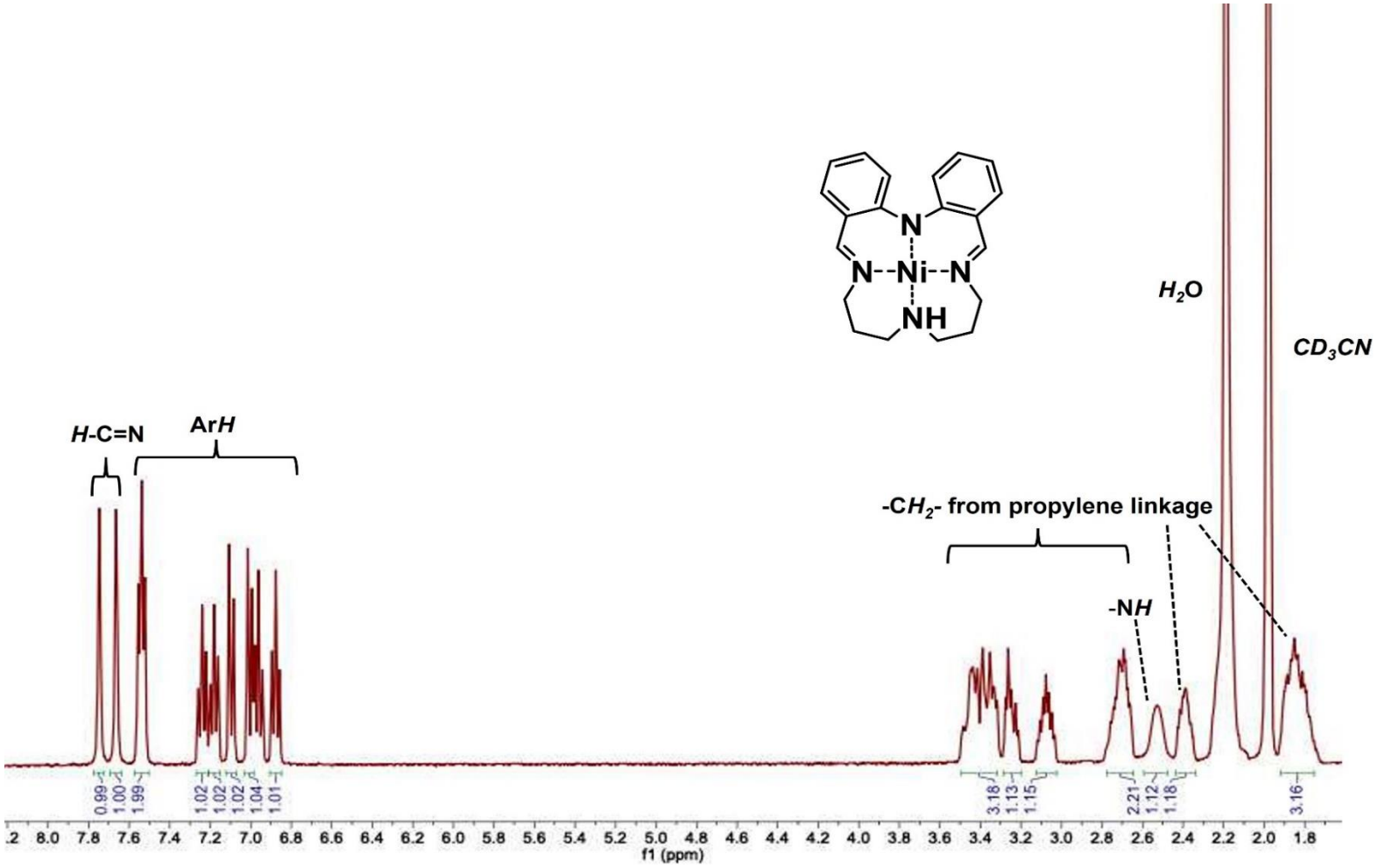

Figure S5 ^{1}H NMR spectrum of [2-Ni](BF$_4$)

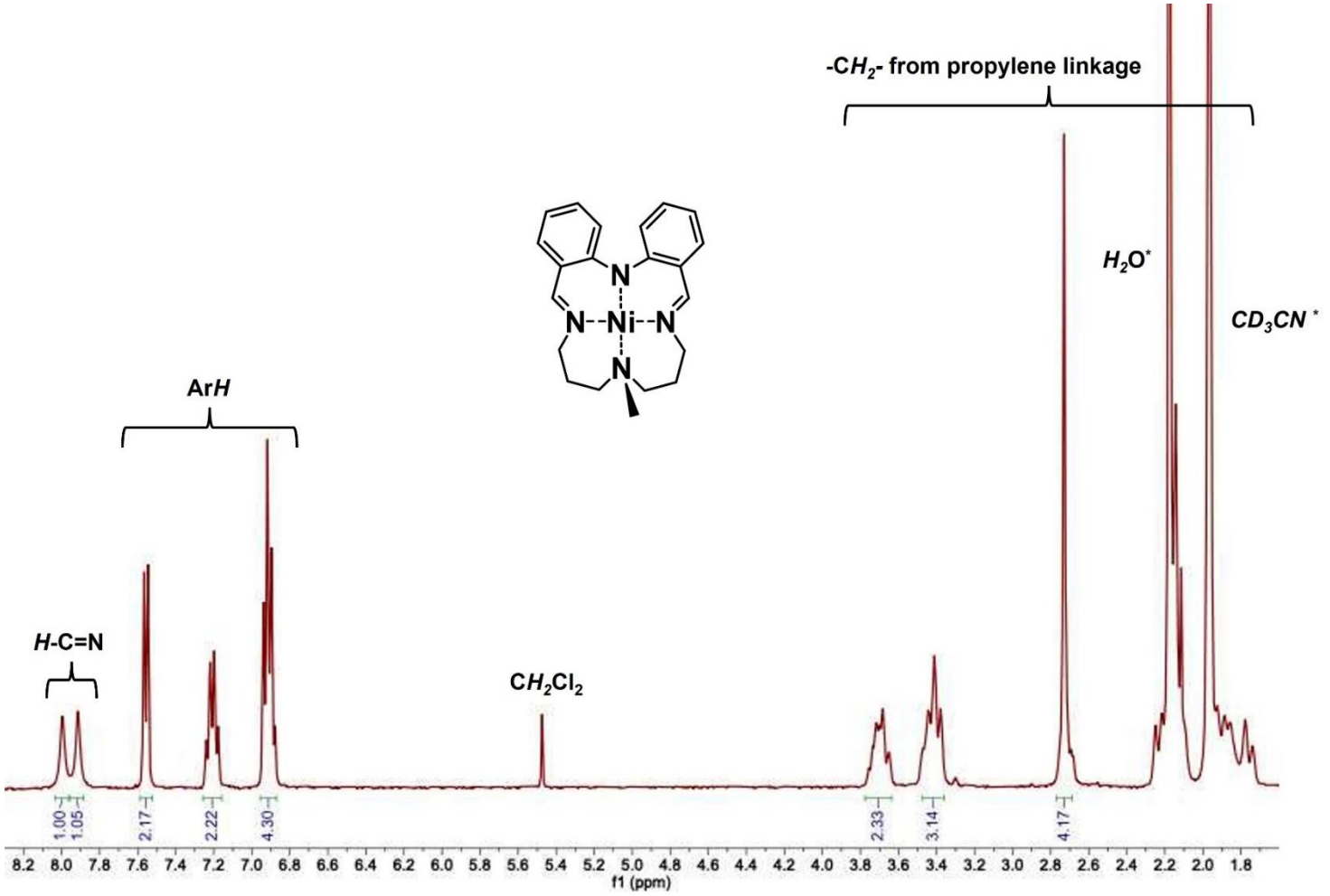

Figure S6 ^{1}H NMR spectrum of [2-Ni]^{Me}(BF_4)

Mass Spectrum List Report

Analysis Info

Analysis Name	D:\Data\Data Service\191111\PLMJ046_RA2_01_3478.d	Acquisition Date	11/11/2019 5:40:19 PM
Method	nv_pos_6min_profile_wguardcol_50-1500_191021.m	Operator	CU.
Sample Name	PLMJ046	Instrument / Ser#	micrOTOF-Q II 10335
Comment			

Acquisition Parameter

Source Type	ESI	Ion Polarity	Positive	Set Nebulizer	3.0 Bar
Focus	Not active	Set Capillary	4000 V	Set Dry Heater	200 °C
Scan Begin	50 m/z	Set End Plate Offset	-500 V	Set Dry Gas	8.0 l/min
Scan End	1500 m/z	Set Collision Cell RF	250.0 Vpp	Set Divert Valve	Waste

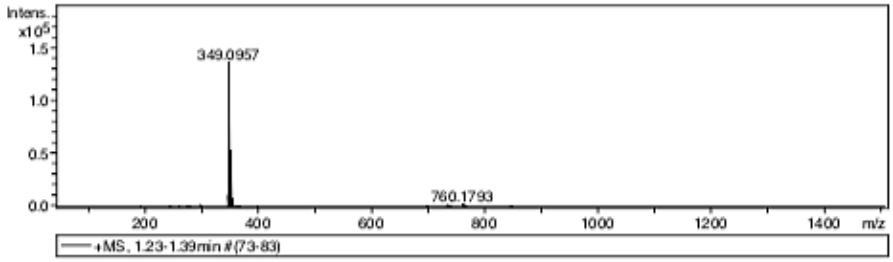

#	m/z	Res.	S/N	I	FWHM
1	192.9438	7767	462.7	268	0.0248
2	243.9411	8473	243.6	331	0.0288
3	260.9312	9109	164.3	266	0.0286
4	277.9221	9014	159.6	300	0.0308
5	298.2739	9393	575.6	1691	0.0318
6	299.2777	9350	108.3	328	0.0320
7	346.0726	9988	52.9	382	0.0346
8	347.0796	9845	1530.1	11148	0.0353
9	348.0841	9542	541.7	3996	0.0365
10	349.0957	8750	18229.6	136074	0.0399
11	350.0978	9409	3647.1	27551	0.0372
12	351.0918	9184	6875.1	52542	0.0382
13	352.0935	9649	1629.0	12596	0.0365
14	353.0898	9541	994.4	7778	0.0370
15	354.0919	9889	202.3	1601	0.0358
16	355.0883	9793	225.7	1806	0.0363
17	356.0916	9698	50.2	407	0.0367
18	365.0898	9639	54.2	484	0.0379
19	367.0956	8069	29.7	271	0.0455
20	733.1599	13351	262.8	1000	0.0549
21	734.1652	12836	103.0	395	0.0572
22	735.1579	13189	296.9	1141	0.0557
23	736.1586	13309	125.5	485	0.0553
24	737.1551	12689	141.6	550	0.0581
25	760.1793	12433	599.0	2570	0.0611
26	761.1810	12693	258.6	1115	0.0600
27	762.1769	12301	516.7	2236	0.0620
28	763.1775	12622	228.6	994	0.0605
29	764.1730	12718	191.6	837	0.0601
30	765.1746	13720	89.2	392	0.0558

Figure S7 High resulotion mass spectrum of [1-Ni](BF_4).

Mass Spectrum List Report

Analysis Info

Analysis Name	D:\Data\Data Service\191125\PLMJ048_RA3_01_3483.d	Acquisition Date	11/25/2019 4:38:16 PM
Method	nv_pos_6min_profile_wguardcol_50-1500_191021.m	Operator	CU.
Sample Name	PLMJ048	Instrument / Ser#	micrOTOF-Q II 10335
Comment			

Acquisition Parameter

Source Type	ESI	Ion Polarity	Positive	Set Nebulizer	3.0 Bar
Focus	Not active	Set Capillary	4000 V	Set Dry Heater	200 °C
Scan Begin	50 m/z	Set End Plate Offset	-500 V	Set Dry Gas	8.0 l/min
Scan End	1500 m/z	Set Collision Cell RF	250.0 Vpp	Set Divert Valve	Waste

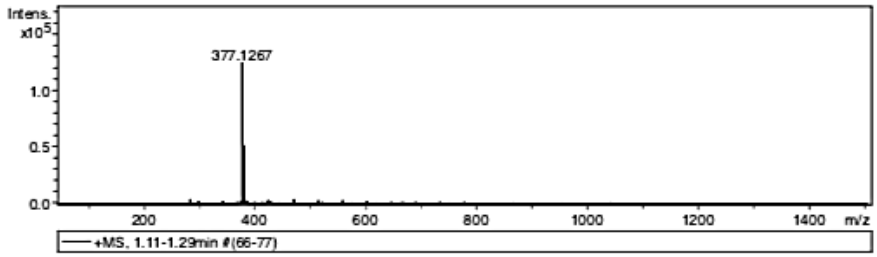

#	m/z	Res.	S/N	I	FWHM
1	284.3304	9040	852.4	3438	0.0315
2	298.2737	9064	326.9	2055	0.0329
3	341.2654	9880	127.5	1952	0.0345
4	368.4245	10305	79.2	1665	0.0358
5	375.1110	10005	78.2	1753	0.0375
6	377.1267	8803	5469.0	124724	0.0428
7	378.1291	9683	1203.0	27691	0.0391
8	379.1223	9651	2205.5	51223	0.0393
9	380.1246	10072	557.9	13078	0.0377
10	381.1209	9948	329.4	7790	0.0383
11	382.1230	10224	68.0	1624	0.0374
12	383.1207	9893	72.8	1754	0.0387
13	384.1873	9507	41.4	1008	0.0404
14	385.2911	10034	76.1	1869	0.0384
15	400.3759	10348	49.2	1087	0.0387
16	422.1108	10717	55.9	1026	0.0394
17	425.3596	10554	185.1	3287	0.0403
18	428.4082	10419	72.2	1247	0.0411
19	429.3166	10410	61.7	1056	0.0412
20	469.3851	10926	379.0	3869	0.0430
21	470.3884	10832	111.7	1122	0.0434
22	513.4115	10772	389.5	3144	0.0477
23	514.4152	11333	126.1	1020	0.0454
24	557.4384	11798	339.0	2818	0.0473
25	601.4650	11701	232.1	1991	0.0514
26	645.4893	12497	192.9	1709	0.0517
27	666.6385	12185	173.8	1564	0.0547
28	689.5151	12424	165.8	1452	0.0555
29	733.5421	12982	183.7	1399	0.0565
30	777.5684	12950	158.6	1036	0.0600

Figure S8 High resulotion mass spectrum of [2-Ni](BF_4).

Mass Spectrum List Report

Analysis Info

Analysis Name	D:\Data\Data Service\201221\PLMJ079_NiN4Me_RC2_01_5092.d	Acquisition Date	12/21/2020 3:44:40 PM
Method	nv_pos_5min_profile_190214.m	Operator	CU.
Sample Name	PLMJ079_NiN4Me	Instrument / Ser#	micrOTOF-Q II 10335
Comment			

Acquisition Parameter

Source Type	ESI	Ion Polarity	Positive	Set Nebulizer	3.0 Bar
Focus	Not active	Set Capillary	4000 V	Set Dry Heater	200 °C
Scan Begin	100 m/z	Set End Plate Offset	-500 V	Set Dry Gas	8.0 l/min
Scan End	1500 m/z	Set Collision Cell RF	250.0 Vpp	Set Divert Valve	Waste

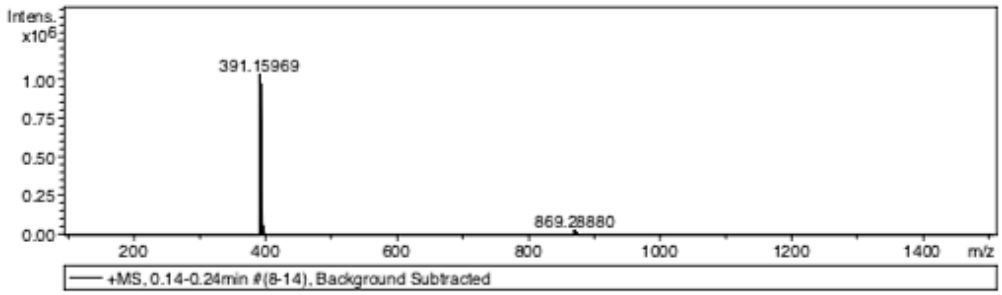

#	m/z	Res.	S/N	I	FWHM
1	195.57037	6894	167.9	1722	0.02837
2	196.07397	6746	329.1	3363	0.02907
3	196.57268	6441	142.5	1459	0.03052
4	197.07094	6859	141.9	1451	0.02873
5	391.15969	3156	196.8	1033315	0.12395
6	392.14840	6414	155.1	827626	0.06114
7	393.14618	4835	179.7	973995	0.08131
8	394.14117	8152	86.0	473290	0.04835
9	395.13697	8588	51.1	285388	0.04601
10	397.13349	9506	10.3	59077	0.04178
11	868.29041	11016	11.8	8178	0.07882
12	869.28880	10413	49.5	34623	0.08348
13	870.28925	10866	32.4	22957	0.08009
14	871.28523	10567	44.2	31777	0.08245
15	872.28516	10800	22.4	16296	0.08076
16	873.28234	10732	16.3	12062	0.08137
17	1349.43196	11821	25.5	1120	0.11415

Figure S9 High resulotion mass spectrum of $[2\text{-Ni}]^{Me}(BF_4)$.

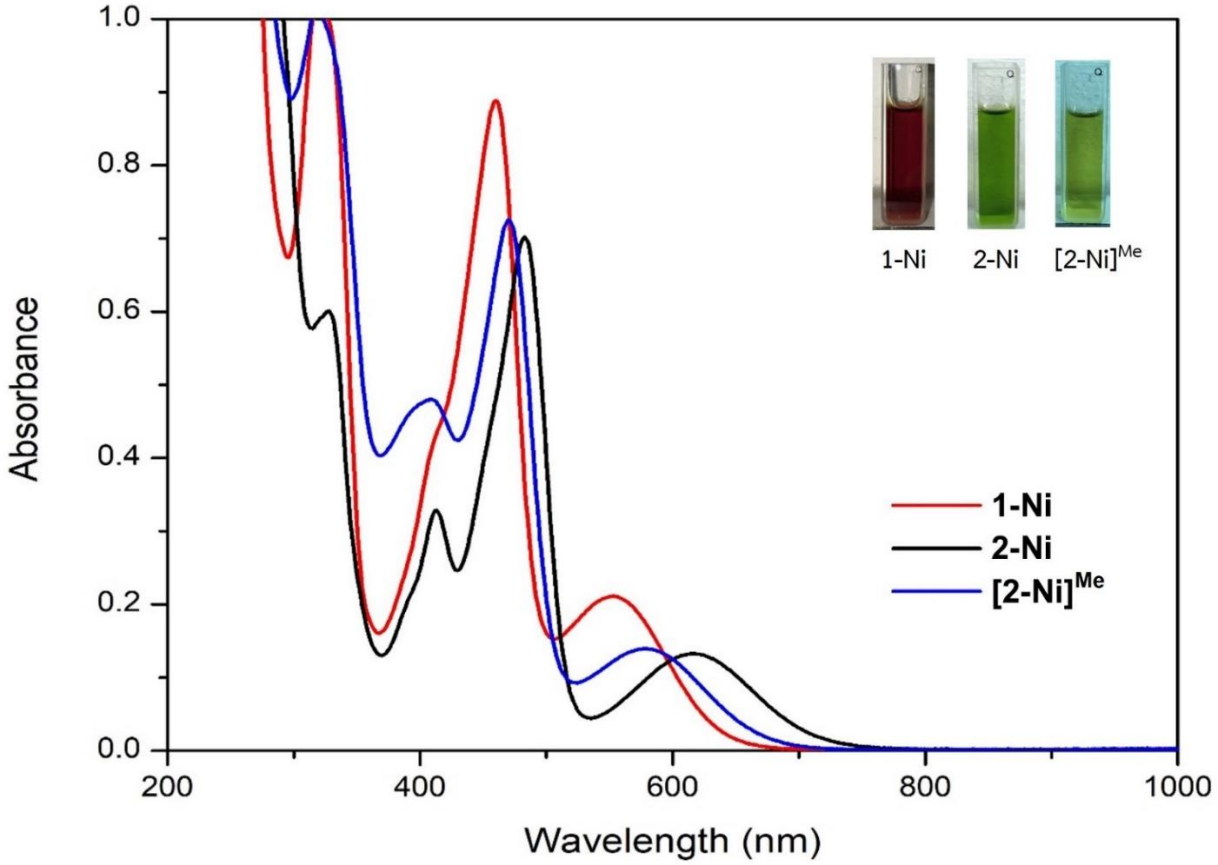

Figure S10 UV-visible adsorption profiles of 1-Ni *(red trace)*, 2-Ni *(black trace)* and [2-Ni]^{Me} *(blue trace)* in CH_3CN at 0.1 mM concentration. Inset: the colour of 1-Ni, 2-Ni, and [2-Ni]^{Me} in CH_3CN at 1 mM

Table S1 Redox potential of Ni^{II}/Ni^{I} couples of **1-Ni** at different scan rates.

Scan rate (V s^{-1})	E_{pc} (V)	E_{pa} (V)	$E_{1/2}$ (V)
0.05	-1.89	-1.82	-1.85
0.1	-1.89	-1.82	-1.85
0.25	-1.90	-1.81	-1.85
0.5	-1.90	-1.81	-1.85
1	-1.92	-1.80	-1.85
2.5	-1.92	-1.79	-1.85
5	-1.92	-1.79	-1.85
10	-1.95	-1.78	-1.86

Table S2 Reductive current of Ni^{II}/Ni^{I} couples of **1-Ni** at different scan rates.

Scan rate (V s^{-1})	i_{pc} (μA)	i_{pa} (μA)	i_{pc}/ i_{pa}
0.05	23.01	-	-
0.1	30.96	-	-
0.25	50.35	-	-
0.5	72.12	-	-
1	104.10	-	-
2.5	160.20	-	-
5	230.50	-	-
10	330.75	-	-

จุฬาลงกรณ์มหาวิทยาลัย
Chulalongkorn University

Table S3 Redox potential of Ni^{II}/Ni^{I} couples of **2-Ni** at different scan rates.

Scan rate (V s^{-1})	E_{pc} (V)	E_{pa} (V)	$E_{1/2}$ (V)
0.05	-1.75	-1.68	-1.72
0.1	-1.75	-1.68	-1.72
0.25	-1.75	-1.68	-1.72
0.5	-1.75	-1.68	-1.72
1	-1.76	-1.67	-1.72
2.5	-1.76	-1.66	-1.71
5	-1.77	-1.66	-1.72
10	-1.78	-1.65	-1.72

Table S4 Reductive and oxidative current of Ni^{II}/Ni^{I} couples of **2-Ni** at different scan rates.

Scan rate (V s^{-1})	i_{pc} (μA)	i_{pa} (μA)	i_{pc}/ i_{pa}
0.05	23.01	20.84	1.10
0.1	30.96	28.26	1.10
0.25	50.35	46.62	1.08
0.5	72.12	63.05	1.14
1	104.10	93.20	1.12
2.5	160.20	139.30	1.15
5	230.50	205.80	1.12
10	330.75	285.13	1.16

จุฬาลงกรณ์มหาวิทยาลัย
Chulalongkorn University

Table S5 Redox potential of Ni^{II}/Ni^{I} couples of [**2-Ni**]^{Me} at different scan rates.

Scan rate (V s^{-1})	E_{pc} (V)	E_{pa} (V)	$E_{1/2}$ (V)
0.05	-1.55	-1.49	-1.52
0.1	-1.55	-1.49	-1.52
0.2	-1.56	-1.49	-1.53
0.4	-1.56	-1.48	-1.52
0.6	-1.56	-1.48	-1.52
0.8	-1.56	-1.49	-1.53
1.0	-1.56	-1.48	-1.52

Table S6 Reductive and oxidative current of Ni^{II}/Ni^{I} couples of [**2-Ni**]^{Me} at different scan rates.

Scan rate (V s^{-1})	i_{pc} (μA)	i_{pa} (μA)	i_{pc}/ i_{pa}
0.05	22.32	21.12	1.05
0.1	31.01	29.83	1.04
0.2	43.74	42.00	1.04
0.4	63.39	60.45	1.05
0.6	76.92	73.76	1.04
0.8	89.57	84.54	1.06
1.0	98.81	94.22	1.05

จุฬาลงกรณ์มหาวิทยาลัย
Chulalongkorn University

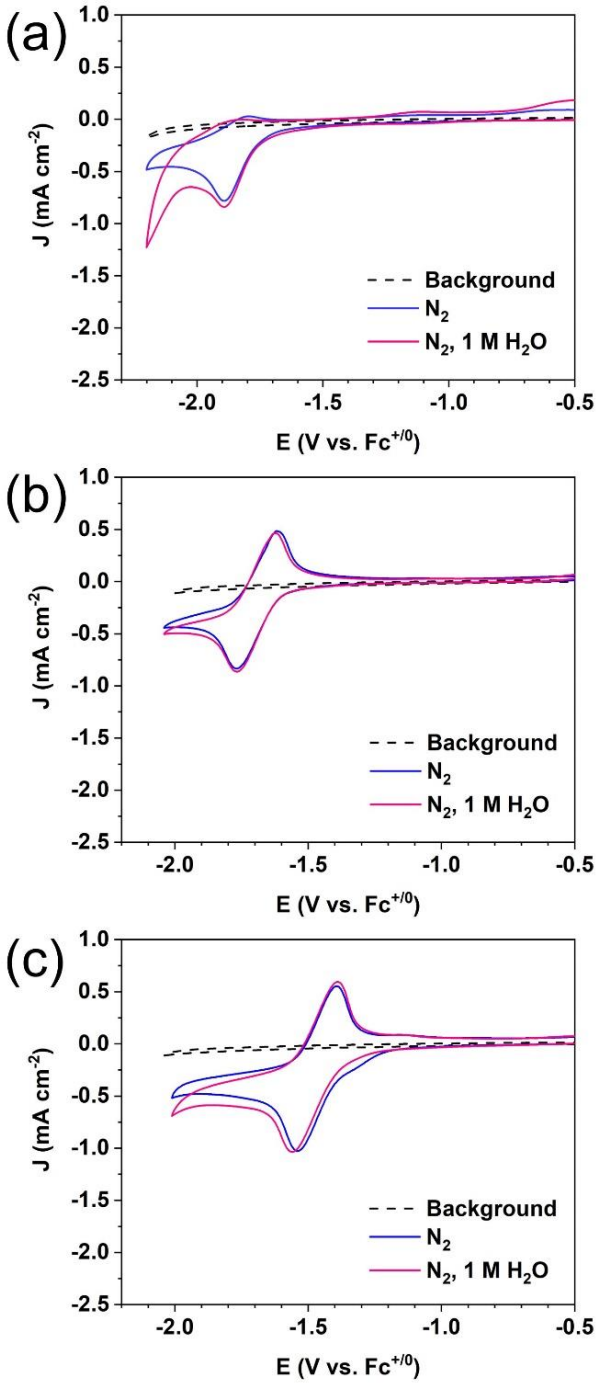

Figure S11 Cyclic voltammograms of (a) 1-Ni, (b) 2-Ni, and (c) $[2\text{-Ni}]^{Me}$ at 1 mM concentration in 0.1 M NBu_4PF_6/CH_3CN (**V** = 0.1 V**/s**) under N_2 (blue) and under N_2 with 1 M H_2O (pink). Background signals were collected under CO_2-saturated 0.1 M NBu_4PF_6/CH_3CN and illustrated in black-dashed line. Carbon paper (Area = 1 cm^2) was used as a working electrode.

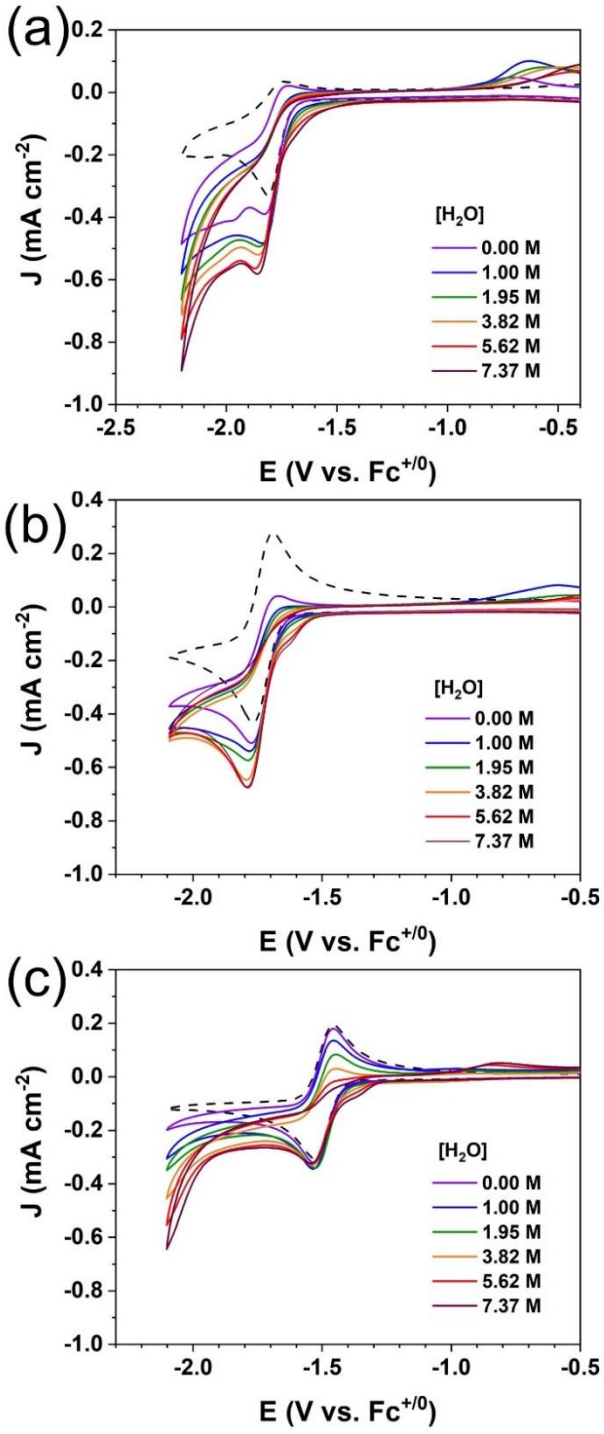

Figure S12 Cyclic voltammograms (CVs) of (a) 1-Ni, (b) 2-Ni and (c) $[2\text{-Ni}]^{Me}$ in CO_2-saturated CH_3CN/ 0.1 M Bu_4NPF_6 with the various concentration of H_2O. CVs in N_2-saturated CH_3CN/ 0.1 M Bu_4NPF_6 were illustrated in the broken line. Glassy carbon (Area = 0.071 cm^2) was used as a working electrode.

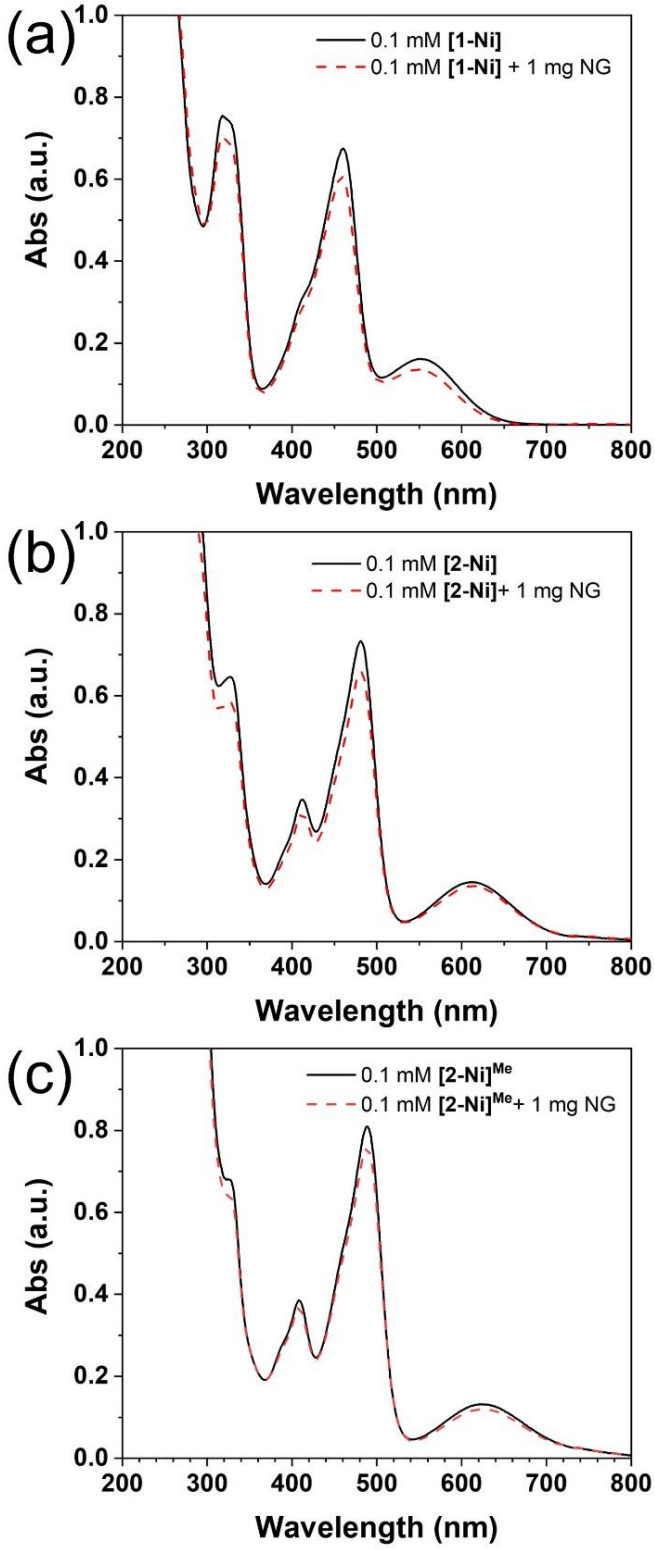

Figure S13 UV-visible spectra of (a) 1-Ni, (b) 2-Ni and (c) $[2\text{-Ni}]^{Me}$ complexes before (black solid line) and after (red dotted line) adsorption on NG.

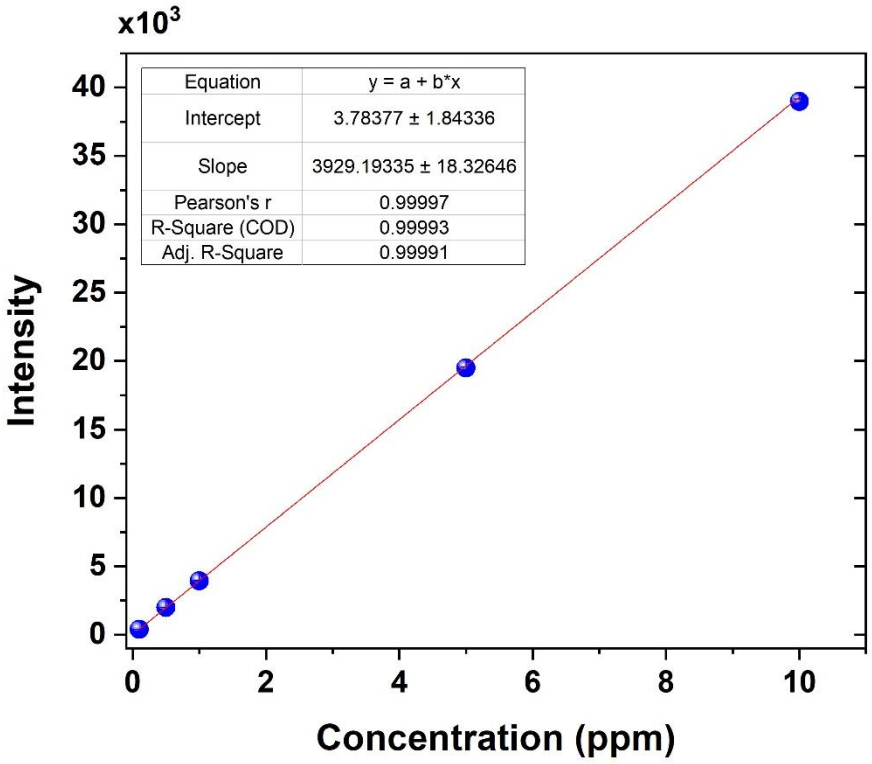

Figure S14 Calibration curve of standard Ni solution in 1% HNO_3.

Table S7 Standard Ni concentration measured by inductively coupled plasmas-optical emission spectroscopy (ICP-OES) for constructing a calibration curve.

Concentration (ppm)	Intensity (a.u.)	Standard Derivation	%RSD
0.1	396.7	0.08994	0.02
0.5	1985	6.431	0.32
1	3935	17.57	0.45
5	19500	99.1	0.5
10	38980	184.4	0.47

จุฬาลงกรณ์มหาวิทยาลัย
Chulalongkorn University

Table S8 Calculated concentration of Ni content in as-prepared hybrid catalyst by using ICP-OES (1-Ni@NG, 2-Ni@NG, and [2-Ni]^{Me}@NG)

Samples	Intensity (a.u.)	Concentration of Ni (ppm)	Concentration of Ni (μmol mg^{-1})
1-Ni@NG	2794	0.71	0.78
2-Ni@NG	1843	0.47	0.52
[2-Ni]^{Me}@NG	1411	0.36	0.40

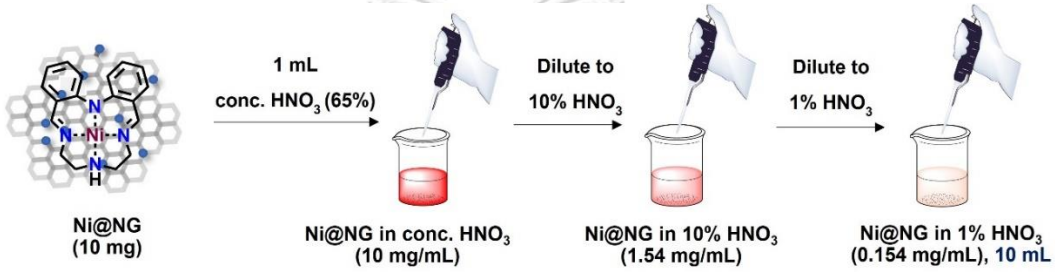

Figure S15 Diagram of Ni@NG sample preparation for ICP-OES.

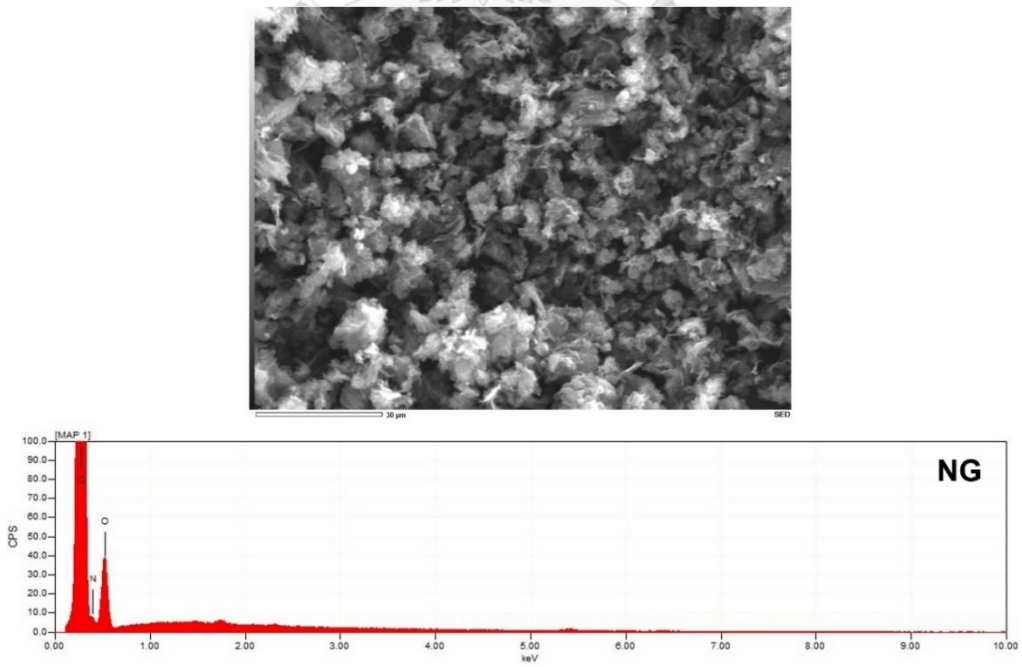

Figure S16 Scanning electron microscopy (SEM) image of N-doped graphene at 1000-fold magnification and energy dispersive X-ray spectrum (EDS) of NG.

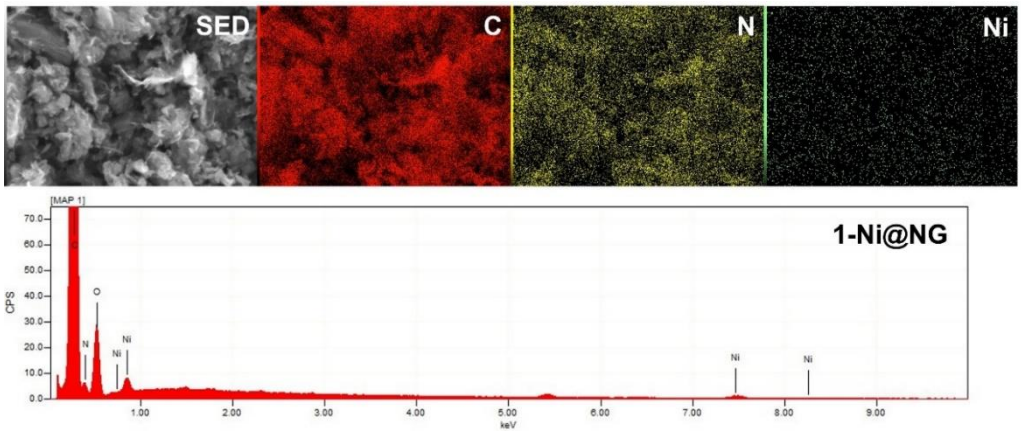

Figure S17 3000-fold-magnified SEM images coupled with elemental mapping of 1-Ni@NG. C (red), N (yellow), Ni (green). EDS spectrum of 1-Ni@NG.

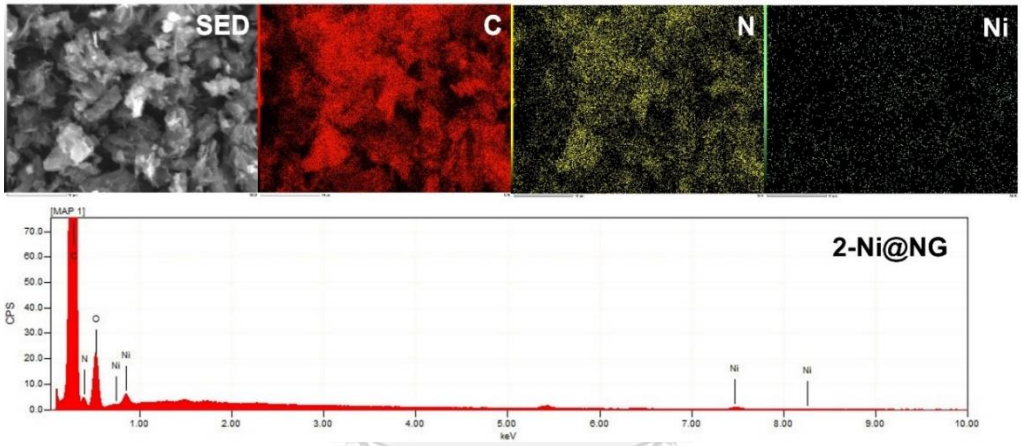

Figure S18 3000-fold-magnified SEM images coupled with elemental mapping of 2-Ni@NG. C (red), N (yellow), Ni (green). EDS spectrum of 2-Ni@NG.

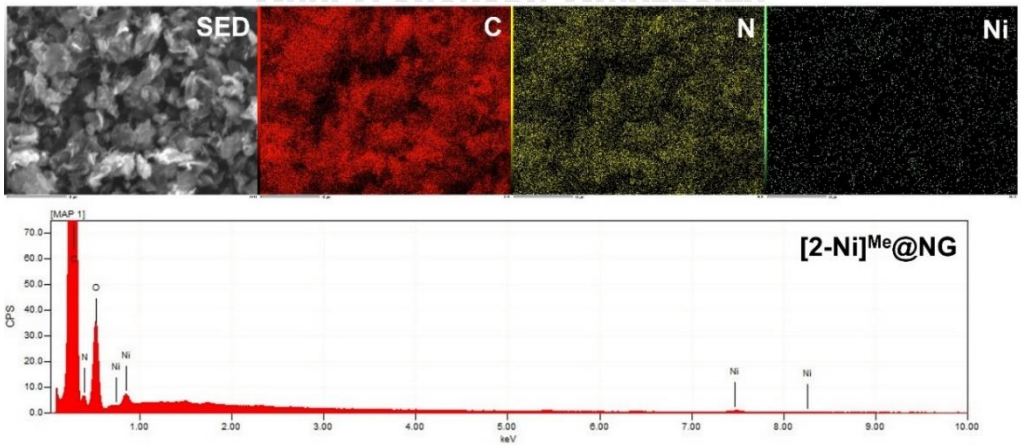

Figure S19 3000-fold-magnified SEM images coupled with elemental mapping of $[2\text{-Ni}]^{Me}$@NG. C (red), N (yellow), Ni (green). EDS spectrum of $[2\text{-Ni}]^{Me}$@NG.

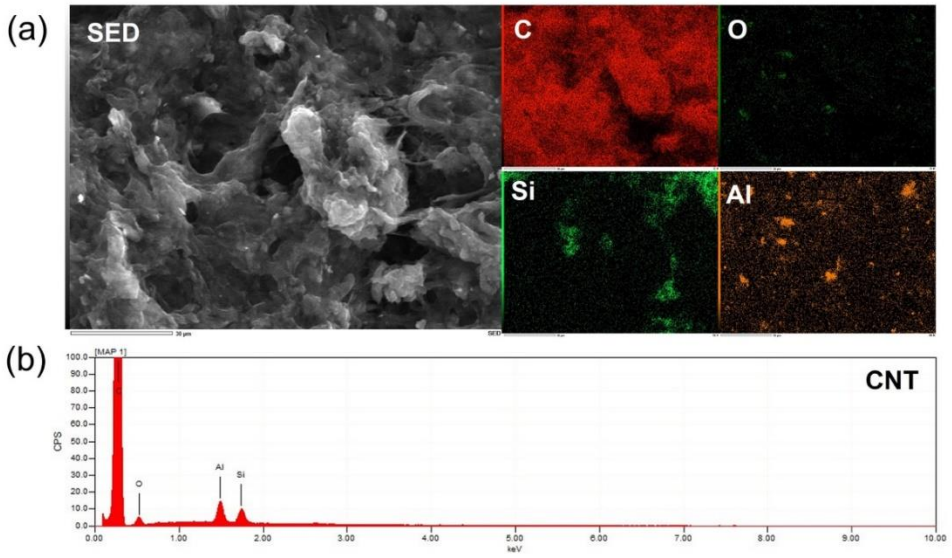

Figure S20 (a) Scanning electron microscopic (SEM) image of pristine CNT and elemental mapping (C = red, O = dark green, Si = light green, Al = orange). (b) Energy dispersive X-ray spectroscopy (EDS) of pristine CNT. Silicon wafer was used as a holder for sample preparation.

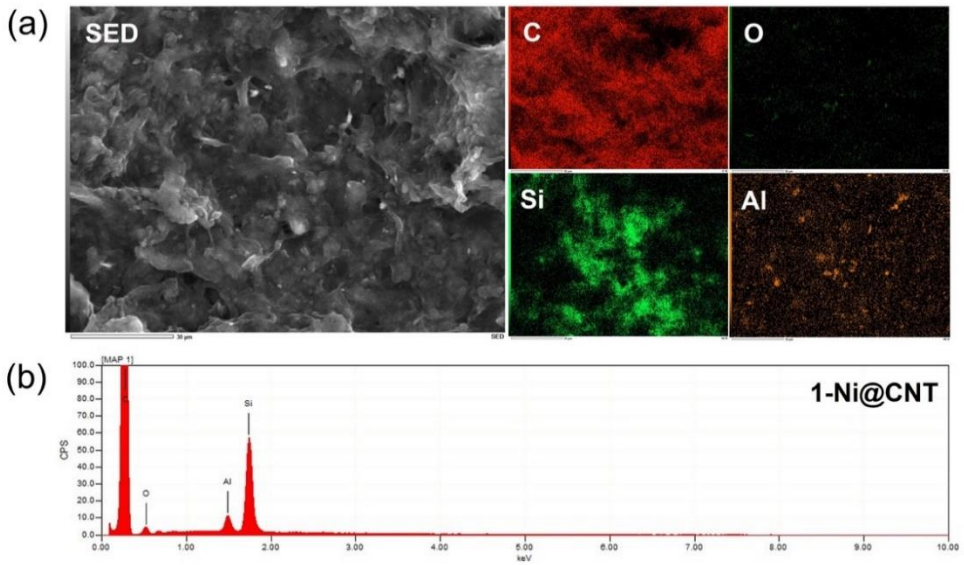

Figure S21 (a) Scanning electron microscopic (SEM) image of 1-Ni@CNT and elemental mapping (C = red, O = dark green, Si = light green, Al = orange). (b) Energy dispersive X-ray spectroscopy (EDS) of 1-Ni@CNT. Silicon wafer was used as a holder for sample preparation.

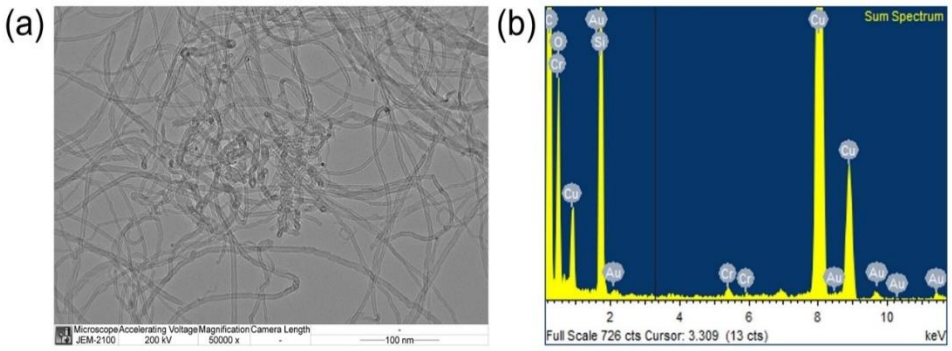

Figure S22 (a) Transmission electron microscopic (TEM) image of 1-Ni@CNT. (b) Energy dispersive X-ray spectroscopy (EDS) of 1-Ni@CNT. Cu grid was used as a holder for sample preparation.

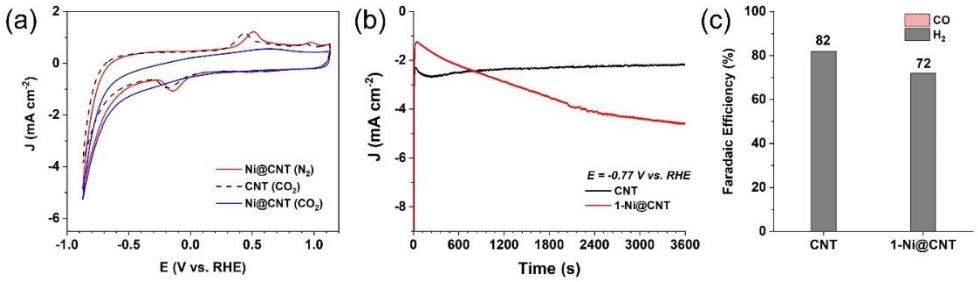

Figure S23 (a) Cyclic voltammograms of CNT and 1-Ni@CNT in 0.5 M $NaHCO_3$. (b) Chronoamperometric measurement of CNT and 1-Ni@CNT in CO_2-saturated 0.5 M $NaHCO_3$ (pH = 7.3) for 1 h. (c) Faradaic efficiency of CNT and 1-Ni@CNT showing only H_2 was observed during the bulk electrolysis.

จุฬาลงกรณ์มหาวิทยาลัย
Chulalongkorn University

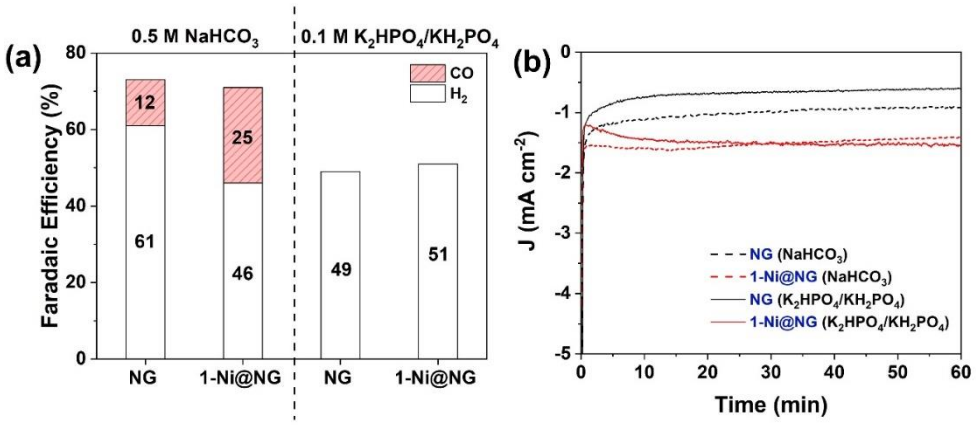

Figure S24 (a) Faradaic efficiencies and (b) current-time profiles for controlled potential electrolysis for 1 h at -0.67 V *vs.* RHE in N_2-saturated 0.1 M K_2HPO_4/KH_2PO_4 (pH 8.1) of NG (black solid line) and 1-Ni@NG (red solid line) versus in N_2-saturated 0.5 M $NaHCO_3$ (pH 8.7) of NG (black dotted line) and 1-Ni@NG (red dotted line).

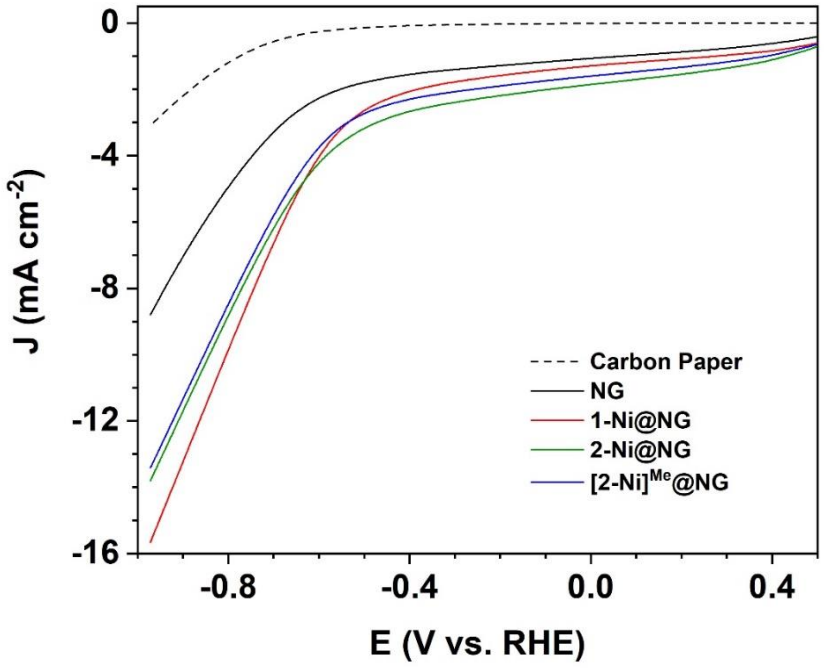

Figure S25 Linear sweep voltammetry (LSV) in CO_2-saturated 0.5 M $NaHCO_3$ for carbon paper (black dotted line), NG (black solid line), 1-Ni@NG (red solid line), 2-Ni@NG (green solid line), and $[2\text{-Ni}]^{Me}$@NG (blue solid line) at the scan rate of 0.05 V/s.

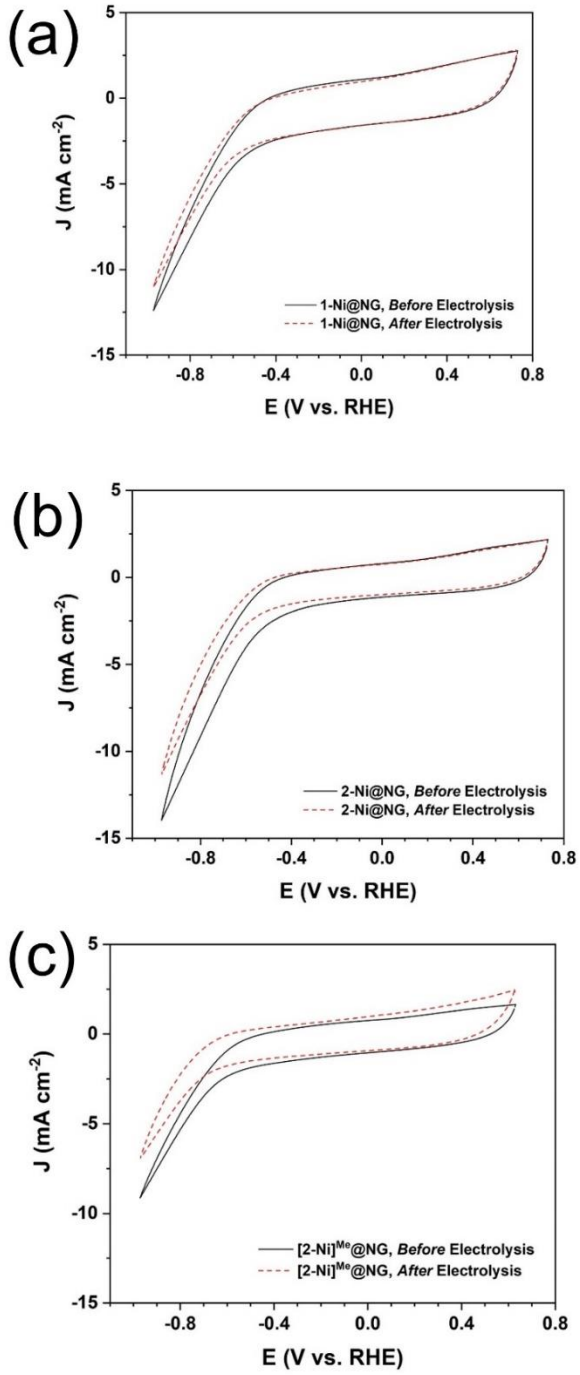

Figure S26 Cyclic voltammetry in CO_2-saturated 0.5 M $NaHCO_3$ before (black solid line) and after electrolysis (red-dotted line) at -0.67 V vs. RHE for 4 h for (a) 1-Ni@NG, (b) 2-Ni@NG and (c) $[2\text{-Ni}]^{Me}$@NG.

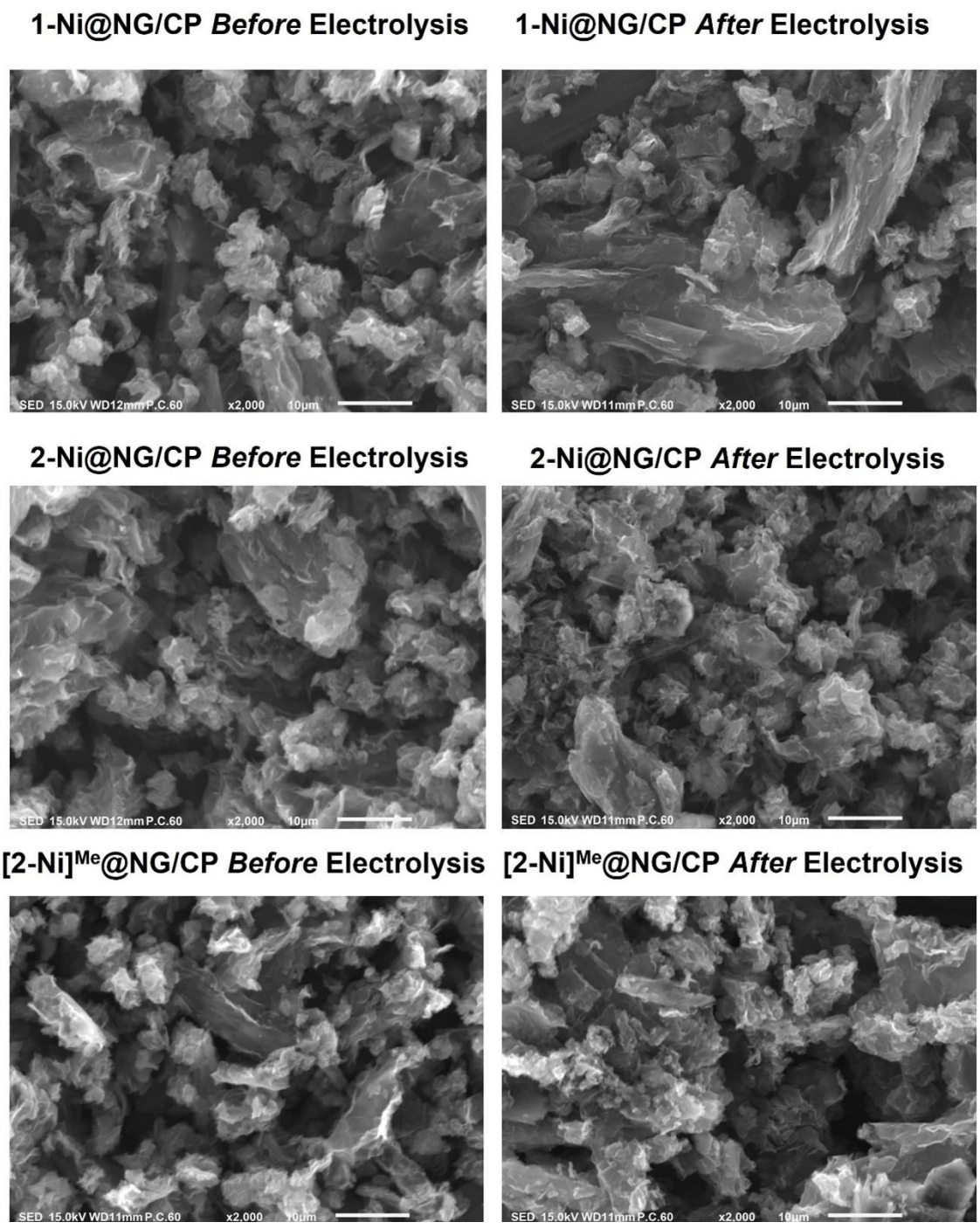

Figure S27 SEM images at 2000-fold magnification of **1-Ni@NG/CP**, **2-Ni@NG/CP** and **[2-Ni]^{Me}@NG/CP** before and after electrocatalysis for 4 h at the applied potential of -0.67 V *vs.* RHE.

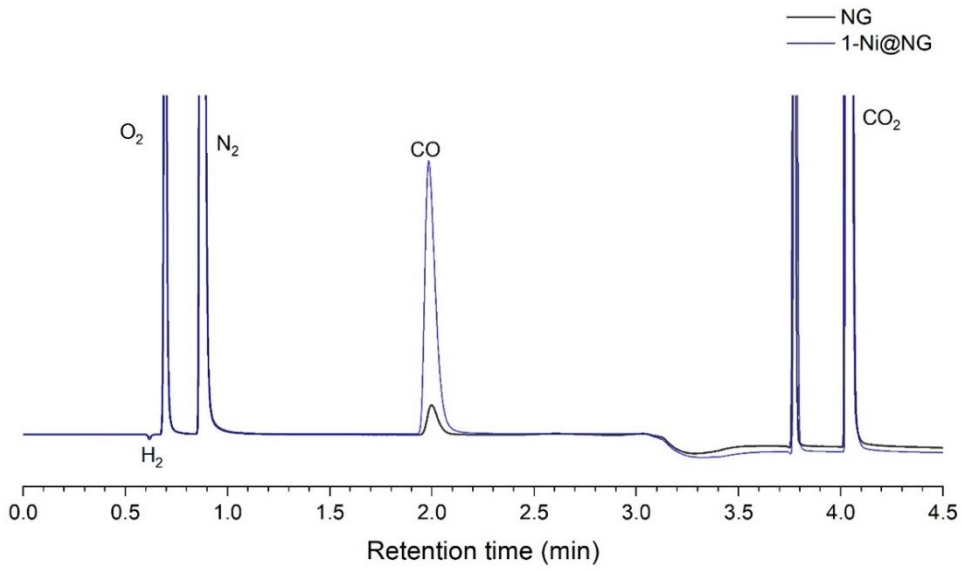

Figure S28 GC traces of bulk electrolysis using NG (black) and 1-Ni@NG (blue) in 0.5 M $NaHCO_3$ at E = -0.77 V *vs.* RHE for 1 h. Retention time of H_2 (0.617), O_2 (0.694), N_2 (0.869), CO (2.010) and CO_2 (4.023). The carrier gas was He and the detector was a thermal conductivity detector (TCD).

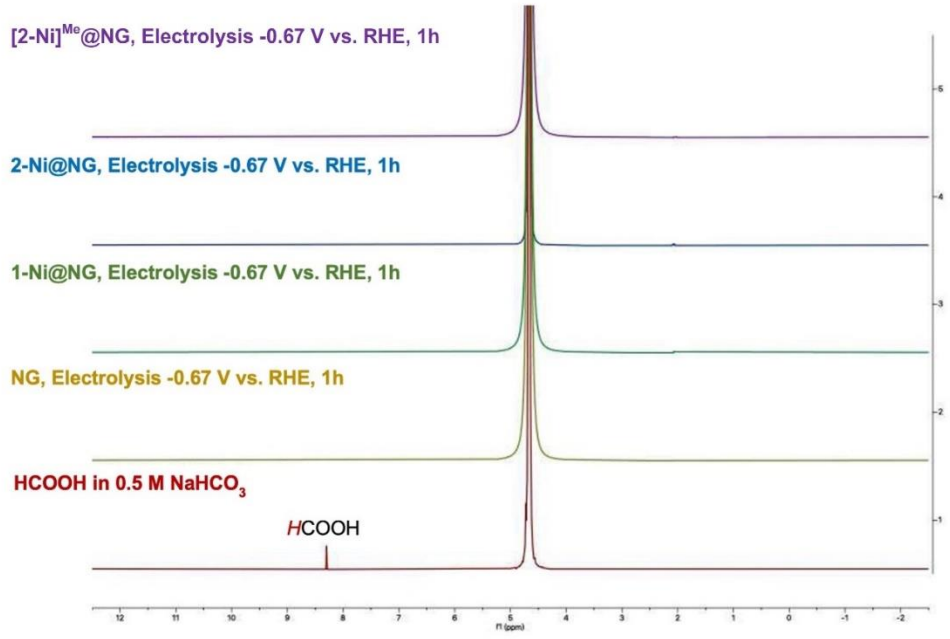

Figure S29 ^1H nuclear magnetic resonance (NMR) spectra of HCOOH in 0.5 M $NaHCO_3$ mixed with D_2O and aliquot after electrolysis at -0.67 V vs. RHE for NG, 1-Ni@NG, 2-Ni@NG and $[2\text{-Ni}]^{Me}$@NG.

Calculation of Faradaic Efficiency

$$\%\text{Faradaic Efficiency} = \frac{Q_{output}}{Q_{input}} \times 100$$

where e_{input} = the total number of moles of electrons measured during electrolysis

e_{output} = the number of moles of electrons required for reducing CO_2 to CO

For bulk electrolysis at *E = -0.77 V vs. RHE*

$$e_{input} = \frac{Q}{F} = \frac{\int i\,dt}{F} = \frac{11.60\ C}{96485 \frac{C}{mole\ of\ electrons}} = 1.20 \times 10^{-4} \text{ mole of electron}$$

Calculation of Faradaic Efficiency of CO (FE_{CO})

Volume of measured CO from GC = 4.42%, which was calibrated from standard gas

Head space of H-type cell = 28 mL

Hence, volume of CO produced = 28 mL x 0.0442 = 1.24 mL

Conversion of volume to mole of produced CO

From the law of ideal gases, n = PV/RT

n = (1 atm)(1.24 x 10^{-3} L)/(0.0821 L atm mol^{-1} K^{-1})(298.15 K)

จุฬาลงกรณ์มหาวิทยาลัย
CHULALONGKORN UNIVERSITY

Thus, moles of produced CO n_{CO} = 5.07 x 10^{-5} mol

Electrochemical CO_2-to-CO conversion: $CO_2 + 2H^+ + 2e^- \rightarrow CO + H_2O$

$$e_{output} = 5.07 \times 10^{-5} \text{ mol of CO} \times \frac{2\ mol\ of\ electrons}{1\ mol\ of\ CO} = 1.01 \times 10^{-4} \text{ mol of electrons}$$

$$\text{Hence, } \%FE_{CO} = \frac{e_{output}}{e_{input}} \times 100 = \frac{1.01 \times 10^{-4}\ mole\ electrons}{1.20 \times 10^{-4}\ mole\ electrons} \times 100 = 84.2\%$$

Calculation of Faradaic Efficiency of H_2 (FE_{H2})

Volume of measured H_2 from GC = 0.87%, which was calibrated from standard gas

Head space of H-type cell = 28 mL

Hence, volume of produced H_2 = 28 mL x 0.0087 = 0.24 mL

Conversion of volume to mole of produced H_2

From the law of ideal gases, n = PV/RT

$$n = (1\ atm)(0.24 \times 10^{-3}\ L)/(0.0821\ L\ atm\ mol^{-1}\ K^{-1})(298.15\ K)$$

Thus, moles of produced H_2 $n_{H2} = 0.98 \times 10^{-5}$ mol

Hydrogen Evolution Reaction (HER): $2H^+ + 2e^- \rightarrow H_2$

e_{output} = 0.98 x 10^{-5} mol of H_2 x $\frac{2\ mol\ of\ electrons}{1\ mol\ of\ CO}$ = 1.96 x 10^{-5} mol of electrons

Hence, $\%FE_{H2} = \frac{e_{output}}{e_{input}} \times 100 = \frac{1.96 \times 10^{-5}\ mole\ electrons}{1.20 \times 10^{-4}\ mole\ electrons} \times 100 = 16.3\%$

จุฬาลงกรณ์มหาวิทยาลัย
CHULALONGKORN UNIVERSITY

Table S9 Comparison of the ECR performance of Ni@NG catalysts from this work with high-performance ECR molecular-based catalysts from recent literatures.

Catalyst	Cathode Material	Electrolyte	Applied Potential (V vs. RHE)	J (mA/cm^2)	Product(s)	%FE	TOF (h^{-1})	Ref
1-Ni@NG	Carbon Paper	0.5 M $NaHCO_3$ (pH 7.4)	-0.67	~2	CO	81	97.2	This work
2-Ni@NG				~3		75	151.2	
$[2\text{-Ni}]^{Me}$@NG				~1.5		68	93.6	
Pyrene-modified Ni(cyclam)/MWCNT	GDL	0.1 M Bu_4NPF_6/ CH_3CN + 1% H_2O	-2.54[a]	~10	CO	>90	4.27(s^{-1})	72
NiPc	CFP	0.5 M $KHCO_3$ (pH 7.2)	-0.80	-	CO	<40	-	99
NiPc/CNT	Carbon Paper	0.5 M $KHCO_3$ (pH 7.2)	-0.78	-	CO	78	1025	100
PyNiPc/CNT				-		~100	8715	
Ni(Salen-NO_2)	GDL	0.5 M $KHCO_3$ (pH 7.5)	-1.50[b]	-	CO CH_4 C_2H_6	~40 ~17 ~17	-	101
Ni(Salen-NH_2)/Graphite plates	Graphite Electrode	0.5 M $KHCO_3$ (pH 7.0)	-1.80[c]	-	HCOOH CH_3OH C_2H_5OH	4.7 11.4 28.6	0.33(s^{-1}) 0.8(s^{-1}) 2.1(s^{-1})	73
Ni-CNT-PP	Glassy	0.5 M $KHCO_3$	-0.71	13.4	CO	96	0.6 x 10^5	102

จุฬาลงกรณ์มหาวิทยาลัย CHULALONGKORN UNIVERSITY

Ni-CNT-CC	carbon, RDE	(pH 7.3)		32.3	CO	99	~10^5	
Ni-PMOF	Carbon Cloth	0.5 M $KHCO_3$ (pH 7.2)	-0.80	0.47	CO	18.5	8.11	103
Co-PMOF				~18	CO	98.7	1656	
CoPc	CFP	0.5 M $KHCO_3$ (pH 7.2)	-0.80	-	CO	99	~42	99
CoPc/CCG	Carbon paper	0.1 M $KHCO_3$ (pH 6.8)	-0.59	~0.8	CO	63	~2 (s^{-1})	70
CoPc-Py/CNT	Carbon paper	0.2 M $KHCO_3$ (pH 7.0)	-0.63	~5	CO	98	34.5(s^{-1})	104
CoFPc/carbon cloth	Carbon cloth	0.5 M $NaHCO_3$ (pH 7.3)	-0.80	~4	CO	93	1.6(s^{-1})	105
Fe(bpc)Cl(H_2O)/NG	GC	0.5 M $NaHCO_3$ (pH 7.3)	-0.58	~6	CO	90	2.1(s^{-1})	71
Fe-TPPy/CNT	GC	0.1 M $NaHCO_3$ (pH 6.8)	-0.60	19.6	CO CH_4	37 17	0.97(s^{-1}) 0.07(s^{-1})	68
Fe-*adj*-TPPy/CNT	GC		-0.60	30.4	CO CH_4	67 25	3.49 (s^{-1}) 0.07(s^{-1})	

[a] Applied potential was reported in *V vs.* $Fc^{+/0}$, [b] Applied potential was reported in *V vs. SHE*, [c] Applied potential was reported in *V vs. Ag/AgCl,* ECSA = electrochemically active surface area, CFP = carbon fibre paper, GDL = gas diffusion electrode, GC = glassy carbon, RDE = rotating disk electrode, Pc = phthalocyanine, bpc = 4,5-dichloro-1,2-bis(pyridine-2-carboximido)benzene, CCG = chemically converted graphene, CNT = carbon nanotube, MWCNT = multi-walled carbon nanotube.

Table S10 Comparison of selected bond lengths (Å), angles (°) and twist of diphenylamine unit for 1-Ni, 2-Ni and [2-Ni]^{Me}.

	1-Ni[a]	**2-Ni**[b]	**[2-Ni]^{Me}**
Bond lengths [Å]			
Ni1–N1	1.869(3)	1.867(2)	1.907(5)
Ni1–N2	1.861(7)	1.894(2)	1.914(4)
Ni1–N3	1.924(4)	1.942(2)	2.115(2)
Ni1–N4	1.830(7)	1.899(2)	2.014(4)
Bond angles [°]			
N1–Ni1–N2	94.9(3)	89.48(10)	87.4(2)
N1–Ni1–N3	179.3(4)	174.78(10)	175.12(2)
N1–Ni1–N4	95.3(3)	90.51(10)	92.0(2)
N2–Ni1–N3	85.2(3)	85.98(10)	88.34(2)
N2–Ni1–N4	169.83(19)	174.32(9)	179.5(2)
N3–Ni1–N4	84.6(3)	94.26(10)	92.2(2)
Twist of phenyl rings [°]	47.3	63.4	60.9

[a,b]Crystallographic data was obtained from ref. 76 and 75, respectively.

จุฬาลงกรณ์มหาวิทยาลัย
Chulalongkorn University

Table S11 Selected bond lengths (Å) and angles (°) for $[NiL^{ACR}](BF_4)_2$ and $[NiL^{ACR}](ClO_4)_2$

	$[NiL^{ACR}](BF_4)_2$	$[NiL^{ACR}](ClO_4)_2$
Ni1–N1	2.078(2)	2.081(2)
Ni1–N2	1.957(2)	1.967(2)
Ni1–N3	2.110(2)	2.115(2)
Ni1–N4	2.059(2)	2.065(2)
Ni1–N5	2.061(2)	2.068(2)
N1–Ni1–N2	92.43(8)	92.57(9)
N1–Ni1–N3	174.18(8)	174.22(8)
N1–Ni1–N4	102.33(8)	102.25(9)
N1–Ni1–N5	94.44(8)	94.55(9)
N2–Ni1–N3	83.72(8)	83.47(9)
N2–Ni1–N4	103.13(9)	102.53(10)
N2–Ni1–N5	114.34(9)	116.40(11)
N3–Ni1–N4	82.84(8)	82.77(9)
N3–Ni1–N5	83.24(9)	83.51(9)
N4–Ni1–N5	138.08(9)	136.69(11)

จุฬาลงกรณ์มหาวิทยาลัย
CHULALONGKORN UNIVERSITY

Table S12 Hydrogen-bond geometry (Å,°) for $[NiL^{ACR}](BF_4)$

D–H···*A*	*D*–H	H···*A*	*D*···*A*	*D*–H···*A*
N4–H4*A*···F6^{i}	0.89	2.12	2.997(6)	167
N4–H4*A*···F6*A*^{i}	0.89	2.36	3.193(9)	155
N4–H4*A*···F8^{i}	0.89	2.56	3.260(14)	136
N4–H4*A*···F8*A*^{i}	0.89	2.35	3.158(8)	151
N4–H4*B*···N6	0.89	2.41	3.175(4)	144
N5–H5*A*···F3	0.89	2.44	3.234(14)	148
N5–H5*A*···F3*A*	0.89	2.26	3.108(11)	160
N5–H5*B*···F7*A*	0.89	2.31	3.059(13)	142
N5–H5*B*···F8	0.89	2.24	2.970(11)	139
C4–H4···F6^{ii}	0.93	2.46	3.238(6)	141
C11–H11···F5*A*^{iii}	0.93	2.64	3.252(7)	124

Symmetry codes: (i) *x*–1, *y*, *z*; (ii) *x*–1, *y*+1, *z*; (iii) –*x*+1, –*y*, –*z*+1

จุฬาลงกรณ์มหาวิทยาลัย
Chulalongkorn University

Table S13 Hydrogen-bond geometry (Å, °) for $[NiL^{ACR}](ClO_4)_2$

D–H···*A*	*D*–H	H···*A*	*D*···*A*	*D*–H···*A*
N4–H4*A*···O5^{i}	0.89	2.36	3.166(6)	151
N4–H4*A*···O7*A*^{i}	0.89	2.15	3.022(8)	166
N4–H4*B*···N6^{i}	0.89	2.39	3.162(4)	146
N5–H5*A*···O3	0.89	2.38	3.198(6)	154
N5–H5*B*···O8	0.89	2.35	3.088(8)	141
N5–H5*B*···O8*A*	0.89	2.30	3.013(10)	137
C11–H11···O6^{ii}	0.93	2.61	3.254(7)	127

Symmetry codes: (i) *x*−1, *y*, *z*; (ii) −*x*+1, −*y*, −*z*+1.

จุฬาลงกรณ์มหาวิทยาลัย
CHULALONGKORN UNIVERSITY

REFERENCES

1. Chu, S.; Majumdar, A., Opportunities and challenges for a sustainable energy future. *Nature* **2012,** *488* (7411), 294-303.

2. Abanades, J. C.; Rubin, E. S.; Mazzotti, M.; Herzog, H. J., On the climate change mitigation potential of CO_2 conversion to fuels. *Energy Environ. Sci.* **2017,** *10* (12), 2491-2499.

3. Crippa M., G. D., Banja M., Solazzo E., Muntean M., Schaaf E., Pagani F., Monforti-Ferrario F., Olivier, J.G.J., Quadrelli, R., Risquez Martin, A., Taghavi-Moharamli, P., Grassi, G., Rossi, S., Oom, D., Branco, A., San-Miguel, J., Vignati. *CO_2 Emissions of All World Countries – JRC/IEA/PBL 2022 Report*; 2022.

4. Kamkeng, A. D. N.; Wang, M.; Hu, J.; Du, W.; Qian, F., Transformation technologies for CO_2 utilisation: Current status, challenges and future prospects. *J. Chem. Eng.* **2021,** *409*.

5. Cai, X.; Hu, Y. H., Advances in catalytic conversion of methane and carbon dioxide to highly valuable products. *Energy Sci. Eng.* **2019,** *7* (1), 4-29.

6. Aresta, M.; Dibenedetto, A.; Angelini, A., Catalysis for the valorization of exhaust carbon: from CO_2 to chemicals, materials, and fuels. technological use of CO_2. *Chem. Rev.* **2014,** *114* (3), 1709-42.

7. Centi, G.; Quadrelli, E. A.; Perathoner, S., Catalysis for CO_2 conversion: a key technology for rapid introduction of renewable energy in the value chain of chemical industries. *Energy Environ. Sci.* **2013,** *6* (6).

8. Do, T. N.; You, C.; Kim, J., A CO_2 utilization framework for liquid fuels and chemical production: techno-economic and environmental analysis. *Energy Environ. Sci.* **2022,** *15* (1), 169-184.

9. Chen, X.; Chen, Y.; Song, C.; Ji, P.; Wang, N.; Wang, W.; Cui, L., Recent Advances in Supported Metal Catalysts and Oxide Catalysts for the Reverse Water-Gas Shift Reaction. *Front. Chem.* **2020,** *8*, 709.

10. Yahiro, H.; Murawaki, K.; Saiki, K.; Yamamoto, T.; Yamaura, H., Study on the supported Cu-based catalysts for the low-temperature water–gas shift reaction. *Catal.*

จุฬาลงกรณ์มหาวิทยาลัย
Chulalongkorn University

Today **2007,** *126* (3-4), 436-440.

11. Zhang, Q.; Pastor-Pérez, L.; Gu, S.; Ramirez Reina, T., Transition Metal Carbides (TMCs) Catalysts for Gas Phase CO_2 Upgrading Reactions: A Comprehensive Overview. *Catalysts* **2020,** *10* (9).

12. Sarp, S.; Gonzalez Hernandez, S.; Chen, C.; Sheehan, S. W., Alcohol Production from Carbon Dioxide: Methanol as a Fuel and Chemical Feedstock. *Joule* **2021,** *5* (1), 59-76.

13. Ahmed, A. A.; Al Labadidi, M.; Hamada, A. T.; Orhan, M. F., Design and Utilization of a Direct Methanol Fuel Cell. *Membr.* **2022,** *12* (12).

14. Li, W.; Wang, H.; Jiang, X.; Zhu, J.; Liu, Z.; Guo, X.; Song, C., A short review of recent advances in CO_2 hydrogenation to hydrocarbons over heterogeneous catalysts. *RSC. Adv.* **2018,** *8* (14), 7651-7669.

15. Ashok, J.; Pati, S.; Hongmanorom, P.; Tianxi, Z.; Junmei, C.; Kawi, S., A review of recent catalyst advances in CO_2 methanation processes. *Catal. Today* **2020,** *356*, 471-489.

16. Galadima, A.; Muraza, O., Catalytic thermal conversion of CO_2 into fuels: Perspective and challenges. *Renewable Sustainable Energy Rev.* **2019,** *115*.

17. Porta, A.; Falbo, L.; Visconti, C. G.; Lietti, L.; Bassano, C.; Deiana, P., Synthesis of Ru-based catalysts for CO_2 methanation and experimental assessment of intraporous transport limitations. *Catal. Today* **2020,** *343*, 38-47.

18. Wittich, K.; Krämer, M.; Bottke, N.; Schunk, S. A., Catalytic Dry Reforming of Methane: Insights from Model Systems. *ChemCatChem* **2020,** *12* (8), 2130-2147.

19. Ranjekar, A. M.; Yadav, G. D., Dry reforming of methane for syngas production: A review and assessment of catalyst development and efficacy. *J. Indian Chem. Soc.* **2021,** *98* (1).

20. Wu, J.; Huang, Y.; Ye, W.; Li, Y., CO_2 Reduction: From the Electrochemical to Photochemical Approach. *Adv. Sci.* **2017,** *4* (11), 1700194.

21. Qiao, J.; Liu, Y.; Hong, F.; Zhang, J., A review of catalysts for the electroreduction of carbon dioxide to produce low-carbon fuels. *Chem. Soc. Rev.* **2014,** *43* (2), 631-75.

22. Kortlever, R.; Shen, J.; Schouten, K. J.; Calle-Vallejo, F.; Koper, M. T., Catalysts

จุฬาลงกรณ์มหาวิทยาลัย
Chulalongkorn University

and Reaction Pathways for the Electrochemical Reduction of Carbon Dioxide. *J. Phys. Chem. Lett.* **2015,** *6* (20), 4073-82.

23. Benson, E. E.; Kubiak, C. P.; Sathrum, A. J.; Smieja, J. M., Electrocatalytic and homogeneous approaches to conversion of CO_2 to liquid fuels. *Chem. Soc. Rev.* **2009,** *38* (1), 89-99.

24. Nam, D. H.; De Luna, P.; Rosas-Hernandez, A.; Thevenon, A.; Li, F.; Agapie, T.; Peters, J. C.; Shekhah, O.; Eddaoudi, M.; Sargent, E. H., Molecular enhancement of heterogeneous CO_2 reduction. *Nat. Mater.* **2020,** *19* (3), 266-276.

25. Overa, S.; Ko, B. H.; Zhao, Y.; Jiao, F., Electrochemical Approaches for CO_2 Conversion to Chemicals: A Journey toward Practical Applications. *Acc. Chem. Res.* **2022,** *55* (5), 638-648.

26. Francke, R.; Schille, B.; Roemelt, M., Homogeneously Catalyzed Electroreduction of Carbon Dioxide-Methods, Mechanisms, and Catalysts. *Chem Rev* **2018,** *118* (9), 4631-4701.

27. Lu, S.; Huynh, H. L.; Lou, F.; Guo, M.; Yu, Z., Electrochemical reduction of CO_2 to CH_4 over transition metal atom embedded antimonene: First-principles study. *J.CO2 Util.* **2021,** *51*.

28. Ambre, R. B.; Daniel, Q.; Fan, T.; Chen, H.; Zhang, B.; Wang, L.; Ahlquist, M. S.; Duan, L.; Sun, L., Molecular engineering for efficient and selective iron porphyrin catalysts for electrochemical reduction of CO_2 to CO. *Chem. Commun.* **2016,** *52* (100), 14478-14481.

29. Elgrishi, N.; Chambers, M. B.; Wang, X.; Fontecave, M., Molecular polypyridine-based metal complexes as catalysts for the reduction of CO_2. *Chem. Soc. Rev.* **2017,** *46* (3), 761-796.

30. Su, X.; McCardle, K. M.; Chen, L.; Panetier, J. A.; Jurss, J. W., Robust and Selective Cobalt Catalysts Bearing Redox-Active Bipyridyl-N-heterocyclic Carbene Frameworks for Electrochemical CO_2 Reduction in Aqueous Solutions. *ACS Catal.* **2019,** *9* (8), 7398-7408.

31. Su, X.; McCardle, K. M.; Panetier, J. A.; Jurss, J. W., Electrocatalytic CO_2 reduction with nickel complexes supported by tunable bipyridyl-N-heterocyclic carbene donors: understanding redox-active macrocycles. *Chem. Commun.* **2018,** *54*

จุฬาลงกรณ์มหาวิทยาลัย
Chulalongkorn University

(27), 3351-3354.

32. Feng, Q.; Sun, Y.; Gu, X.; Dong, Z., Advances of Cobalt Phthalocyanine in Electrocatalytic CO_2 Reduction to CO: a Mini Review. *Electrocatalysis* **2022,** *13* (6), 675-690.

33. Boutin, E.; Merakeb, L.; Ma, B.; Boudy, B.; Wang, M.; Bonin, J.; Anxolabehere-Mallart, E.; Robert, M., Molecular catalysis of CO_2 reduction: recent advances and perspectives in electrochemical and light-driven processes with selected Fe, Ni and Co aza macrocyclic and polypyridine complexes. *Chem. Soc. Rev.* **2020**.

34. Liu, D.-C.; Zhong, D.-C.; Lu, T.-B., Non-noble metal-based molecular complexes for CO_2 reduction: From the ligand design perspective. *EnergyChem* **2020,** *2* (3).

35. Beley, M.; Collin, J. P.; Ruppert, R.; Sauvage, J. P., Electrocatalytic reduction of carbon dioxide by nickel cyclam^{2+} in water: study of the factors affecting the efficiency and the selectivity of the process. *J. Am. Chem. Soc.* **1986,** *108* (24), 7461-7467.

36. Froehlich, J. D.; Kubiak, C. P., Homogeneous CO2 reduction by Ni(cyclam) at a glassy carbon electrode. *Inorg Chem* **2012,** *51* (7), 3932-4.

37. Froehlich, J. D.; Kubiak, C. P., The homogeneous reduction of CO(2) by [Ni(cyclam)](+): increased catalytic rates with the addition of a CO scavenger. *J Am Chem Soc* **2015,** *137* (10), 3565-73.

38. Gerschel, P.; Battistella, B.; Siegmund, D.; Ray, K.; Apfel, U.-P., Electrochemical CO_2 Reduction — The Effect of Chalcogenide Exchange in Ni-Isocyclam Complexes. *Organometallics* **2020,** *39* (9), 1497-1510.

39. Cao, L.-M.; Huang, H.-H.; Wang, J.-W.; Zhong, D.-C.; Lu, T.-B., The synergistic catalysis effect within a dinuclear nickel complex for efficient and selective electrocatalytic reduction of CO2 to CO. *Green Chemistry* **2018,** *20* (4), 798-803.

40. Hay, R. W.; Kinsman, B.; Smith, C. I., The chemistry of nickel(II) complexes of 1,4,7,11-tetra-azacyclotetradecane (isocyclam). *Polyhedron* **1995,** *14* (9), 1245-1249.

41. Rudolph, M.; Dautz, S.; Jäger, E.-G., Macrocyclic $[N_4]^{2-}$ Coordinated Nickel Complexes as Catalysts for the Formation of Oxalate by Electrochemical Reduction of Carbon Dioxide. *J. Am. Chem. Soc.* **2000,** *122* (44), 10821-10830.

42. Lacy, D. C.; McCrory, C. C.; Peters, J. C., Studies of cobalt-mediated electrocatalytic CO_2 reduction using a redox-active ligand. *Inorg. Chem.* **2014,** *53* (10),

จุฬาลงกรณ์มหาวิทยาลัย
Chulalongkorn University

4980-8.

43. Nie, W.; Tarnopol, D. E.; McCrory, C. C. L., Enhancing a Molecular Electrocatalyst's Activity for CO_2 Reduction by Simultaneously Modulating Three Substituent Effects. *J. Am. Chem. Soc.* **2021,** *143* (10), 3764-3778.

44. Nichols, A. W.; Chatterjee, S.; Sabat, M.; Machan, C. W., Electrocatalytic Reduction of CO_2 to Formate by an Iron Schiff Base Complex. *Inorg. Chem.* **2018,** *57* (4), 2111-2121.

45. Zhao, X.; Li, J.; Jian, H.; Lu, M.; Wang, M., Two Novel Schiff Base Manganese Complexes as Bifunctional Electrocatalysts for CO_2 Reduction and Water Oxidation. *Molecules* **2023,** *28* (3).

46. Appel, A. M.; Bercaw, J. E.; Bocarsly, A. B.; Dobbek, H.; DuBois, D. L.; Dupuis, M.; Ferry, J. G.; Fujita, E.; Hille, R.; Kenis, P. J.; Kerfeld, C. A.; Morris, R. H.; Peden, C. H.; Portis, A. R.; Ragsdale, S. W.; Rauchfuss, T. B.; Reek, J. N.; Seefeldt, L. C.; Thauer, R. K.; Waldrop, G. L., Frontiers, opportunities, and challenges in biochemical and chemical catalysis of CO_2 fixation. *Chem. Rev.* **2013,** *113* (8), 6621-58.

47. Mondal, B.; Song, J.; Neese, F.; Ye, S., Bio-inspired mechanistic insights into CO_2 reduction. *Curr. Opin. Chem. Biol.* **2015,** *25*, 103-9.

48. Svetlitchnyi, V.; Peschel, C.; Acker, G.; Meyer, O., Two membrane-associated NiFeS-carbon monoxide dehydrogenases from the anaerobic carbon-monoxide-utilizing eubacterium Carboxydothermus hydrogenoformans. *J. Bacteriol.* **2001,** *183* (17), 5134-44.

49. Jeoung, J.-H.; Dobbek, H., Carbon Dioxide Activation at the Ni,Fe-Cluster of Anaerobic Carbon Monoxide Dehydrogenase. *Science* **2007,** *318* (5855), 1461-1464.

50. Nichols, A. W.; Machan, C. W., Secondary-Sphere Effects in Molecular Electrocatalytic CO_2 Reduction. *Front. Chem.* **2019,** *7*, 397.

51. Amanullah, S.; Saha, P.; Nayek, A.; Ahmed, M. E.; Dey, A., Biochemical and artificial pathways for the reduction of carbon dioxide, nitrite and the competing proton reduction: effect of 2nd sphere interactions in catalysis. *Chem. Soc. Rev.* **2021,** *50* (6), 3755-3823.

52. Nichols, E. M.; Derrick, J. S.; Nistanaki, S. K.; Smith, P. T.; Chang, C. J., Positional effects of second-sphere amide pendants on electrochemical CO_2 reduction catalyzed

จุฬาลงกรณ์มหาวิทยาลัย
Chulalongkorn University

by iron porphyrins. *Chem. Sci.* **2018,** *9* (11), 2952-2960.

53. Derrick, J. S.; Loipersberger, M.; Nistanaki, S. K.; Rothweiler, A. V.; Head-Gordon, M.; Nichols, E. M.; Chang, C. J., Templating Bicarbonate in the Second Coordination Sphere Enhances Electrochemical CO_2 Reduction Catalyzed by Iron Porphyrins. *J. Am. Chem. Soc.* **2022,** *144* (26), 11656-11663.

54. Margarit, C. G.; Schnedermann, C.; Asimow, N. G.; Nocera, D. G., Carbon Dioxide Reduction by Iron Hangman Porphyrins. *Organometallics* **2018,** *38* (6), 1219-1223.

55. Gotico, P.; Boitrel, B.; Guillot, R.; Sircoglou, M.; Quaranta, A.; Halime, Z.; Leibl, W.; Aukauloo, A., Second-Sphere Biomimetic Multipoint Hydrogen-Bonding Patterns to Boost CO_2 Reduction of Iron Porphyrins. *Angew. Chem. Int. Ed.* **2019,** *58* (14), 4504-4509.

56. Narouz, M. R.; De La Torre, P.; An, L.; Chang, C. J., Multifunctional Charge and Hydrogen-Bond Effects of Second-Sphere Imidazolium Pendants Promote Capture and Electrochemical Reduction of CO_2 in Water Catalyzed by Iron Porphyrins. *Angew. Chem. Int. Ed.* **2022,** *61* (37), e202207666.

57. Nichols, E. M.; Chang, C. J., Urea-Based Multipoint Hydrogen-Bond Donor Additive Promotes Electrochemical CO_2 Reduction Catalyzed by Nickel Cyclam. *Organometallics* **2018,** *38* (6), 1213-1218.

58. Jiang, Z.; Wang, Y.; Zhang, X.; Zheng, H.; Wang, X.; Liang, Y., Revealing the hidden performance of metal phthalocyanines for CO_2 reduction electrocatalysis by hybridization with carbon nanotubes. *Nano Res.* **2019,** *12* (9), 2330-2334.

59. Zhu, M.; Ye, R.; Jin, K.; Lazouski, N.; Manthiram, K., Elucidating the Reactivity and Mechanism of CO_2 Electroreduction at Highly Dispersed Cobalt Phthalocyanine. *ACS Energy Lett.* **2018,** *3* (6), 1381-1386.

60. Yue, Z.; Ou, C.; Ding, N.; Tao, L.; Zhao, J.; Chen, J., Advances in Metal Phthalocyanine based Carbon Composites for Electrocatalytic CO_2 Reduction. *ChemCatChem* **2020,** *12* (24), 6103-6130.

61. Wu, Y.; Liang, Y.; Wang, H., Heterogeneous Molecular Catalysts of Metal Phthalocyanines for Electrochemical CO_2 Reduction Reactions. *Acc. Chem. Res.* **2021,** *54* (16), 3149-3159.

62. Juthathan, M.; Chantarojsiri, T.; Tuntulani, T.; Leeladee, P., Atomic- and

จุฬาลงกรณ์มหาวิทยาลัย
Chulalongkorn University

Molecular-Level Modulation of Dispersed Active Sites for Electrocatalytic CO_2 Reduction. *Chem. Asian. J.* **2022,** *17* (12), e202200237.

63. Gawande, M. B.; Fornasiero, P.; Zbořil, R., Carbon-Based Single-Atom Catalysts for Advanced Applications. *ACS Catal.* **2020,** *10* (3), 2231-2259.

64. Cui, H.; Guo, Y.; Guo, L.; Wang, L.; Zhou, Z.; Peng, Z., Heteroatom-doped carbon materials and their composites as electrocatalysts for CO_2 reduction. *J. Mater. Chem. A* **2018,** *6* (39), 18782-18793.

65. Huang, L.; Li, W.; Zeng, M.; He, G.; Shearing, P. R.; Parkin, I. P.; Brett, D. J. L., Metal-Nitrogen-doped carbon single-atom electrocatalysts for CO_2 electroreduction. *Compos. B. Eng.* **2021,** *220*.

66. Hu, X. M.; Ronne, M. H.; Pedersen, S. U.; Skrydstrup, T.; Daasbjerg, K., Enhanced Catalytic Activity of Cobalt Porphyrin in CO_2 Electroreduction upon Immobilization on Carbon Materials. *Angew. Chem. Int. Ed.* **2017,** *56* (23), 6468-6472.

67. Zhang, X.; Wang, Y.; Gu, M.; Wang, M.; Zhang, Z.; Pan, W.; Jiang, Z.; Zheng, H.; Lucero, M.; Wang, H.; Sterbinsky, G. E.; Ma, Q.; Wang, Y.-G.; Feng, Z.; Li, J.; Dai, H.; Liang, Y., Molecular engineering of dispersed nickel phthalocyanines on carbon nanotubes for selective CO_2 reduction. *Nat. Energy* **2020,** *5* (9), 684-692.

68. Abdinejad, M.; Dao, C.; Deng, B.; Dinic, F.; Voznyy, O.; Zhang, X.-a.; Kraatz, H.-B., Electrocatalytic Reduction of CO_2 to CH_4 and CO in Aqueous Solution Using Pyridine-Porphyrins Immobilized onto Carbon Nanotubes. *ACS Sustain. Chem. Eng.* **2020,** *8* (25), 9549-9557.

69. Dou, S.; Sun, L.; Xi, S.; Li, X.; Su, T.; Fan, H. J.; Wang, X., Enlarging the pi-Conjugation of Cobalt Porphyrin for Highly Active and Selective CO_2 Electroreduction. *ChemSusChem* **2021,** *14* (9), 2126-2132.

70. Choi, J.; Wagner, P.; Gambhir, S.; Jalili, R.; MacFarlane, D. R.; Wallace, G. G.; Officer, D. L., Steric Modification of a Cobalt Phthalocyanine/Graphene Catalyst To Give Enhanced and Stable Electrochemical CO_2 Reduction to CO. *ACS Energy Lett.* **2019,** *4* (3), 666-672.

71. Mohamed, E. A.; Zahran, Z. N.; Tsubonouchi, Y.; Saito, K.; Yui, T.; Yagi, M., Highly Efficient and Selective Electrocatalytic CO_2-to-CO Conversion by a Non-heme

จุฬาลงกรณ์มหาวิทยาลัย
Chulalongkorn University

Iron Complex with an In-Plane N_4 Ligand in Heterogeneous Aqueous Media. *ACS Appl. Energy Mater.* **2020,** *3* (5), 4114-4120.

72. Pugliese, S.; Huan, N. T.; Forte, J.; Grammatico, D.; Zanna, S.; Su, B. L.; Li, Y.; Fontecave, M., Functionalization of Carbon Nanotubes with Nickel Cyclam for the Electrochemical Reduction of CO_2. *ChemSusChem* **2020,** *13* (23), 6449-6456.

73. Bose, P.; Mukherjee, C.; Golder, A. K., A Ni^{II} complex of the tetradentate salen ligand H_2L^{NH2} comprising an anchoring $–NH_2$ group: synthesis, characterization and electrocatalytic CO_2 reduction to alcohols. *Inorg. Chem. Front.* **2019,** *6* (7), 1721-1728.

74. Greenwell, F.; Neri, G.; Piercy, V.; Cowan, A. J., Noncovalent immobilization of a nickel cyclam catalyst on carbon electrodes for CO_2 reduction using aqueous electrolyte. *Electrochim. Acta* **2021,** *392*.

75. Wilson, R. K.; Brooker, S., Complexes of a porphyrin-like N4-donor Schiff-base macrocycle. *Dalton Trans.* **2013,** *42* (22), 7913-23.

76. Sanyal, R.; Cameron, S. A.; Brooker, S., Synthesis and complexes of an N4 Schiff-base macrocycle derived from 2,2′-iminobisbenzaldehyde. *Dalton Trans.* **2011,** *40* (45), 12277-12287.

77. Black, D. S. C.; Rothnie, N. E., Metal template reactions. XIX. Macrocyclic metal complexes derived from 2,2'-iminobisbenzaldehyde and some primary diamines with additional nitrogen donor atoms. *Aust. J. of Chem.* **1983,** *36* (12), 2395-2406.

78. Juthathan, M.; Chantarojsiri, T.; Chainok, K.; Butburee, T.; Thamyongkit, P.; Tuntulani, T.; Leeladee, P., Molecularly dispersed nickel complexes on N-doped graphene for electrochemical CO_2 reduction. *Dalton Trans.* **2023**, DOI: 10.1039/d3dt00878a.

79. Elgrishi, N.; Rountree, K. J.; McCarthy, B. D.; Rountree, E. S.; Eisenhart, T. T.; Dempsey, J. L., A Practical Beginner's Guide to Cyclic Voltammetry. *J. Chem. Ed.* **2017,** *95* (2), 197-206.

80. Thoi, V. S.; Chang, C. J., Nickel N-heterocyclic carbene-pyridine complexes that exhibit selectivity for electrocatalytic reduction of carbon dioxide over water. *Chem. Commun.* **2011,** *47* (23), 6578-80.

81. dos Santos, T. C.; Mancera, R. C.; Rocha, M. V. J.; da Silva, A. F. M.; Furtado, I. O.; Barreto, J.; Stavale, F.; Archanjo, B. S.; de M. Carneiro, J. W.; Costa, L. T.; Ronconi,

จุฬาลงกรณ์มหาวิทยาลัย
Chulalongkorn University

C. M., CO_2 and H_2 adsorption on 3D nitrogen-doped porous graphene: Experimental and theoretical studies. *J. CO_2 Util.* **2021,** *48*.

82. de Oliveira Neto, P. H.; Rodrigues, J.; de Sousa, L. E.; Gargano, R.; da Cunha, W. F., CO_2 adsorption in nitrogen-doped single-layered graphene quantum dots: a spectroscopic investigation. *J. Mol. Model* **2019,** *25* (3), 66.

83. Goeppert, A.; Czaun, M.; May, R. B.; Prakash, G. K.; Olah, G. A.; Narayanan, S. R., Carbon dioxide capture from the air using a polyamine based regenerable solid adsorbent. *J. Am. Chem. Soc.* **2011,** *133* (50), 20164-7.

84. Daiyan, R.; Lu, X.; Tan, X.; Zhu, X.; Chen, R.; Smith, S. C.; Amal, R., Antipoisoning Nickel–Carbon Electrocatalyst for Practical Electrochemical CO_2 Reduction to CO. *ACS Appl. Energy Mater.* **2019,** *2* (11), 8002-8009.

85. Liang, H. W.; Bruller, S.; Dong, R.; Zhang, J.; Feng, X.; Mullen, K., Molecular metal-Nx centres in porous carbon for electrocatalytic hydrogen evolution. *Nat. Commun.* **2015,** *6*, 7992.

86. Dunwell, M.; Lu, Q.; Heyes, J. M.; Rosen, J.; Chen, J. G.; Yan, Y.; Jiao, F.; Xu, B., The Central Role of Bicarbonate in the Electrochemical Reduction of Carbon Dioxide on Gold. *J. Am. Chem. Soc.* **2017,** *139* (10), 3774-3783.

87. Wuttig, A.; Yoon, Y.; Ryu, J.; Surendranath, Y., Bicarbonate Is Not a General Acid in Au-Catalyzed CO_2 Electroreduction. *J. Am. Chem. Soc.* **2017,** *139* (47), 17109-17113.

88. Martin, D. J.; McCarthy, B. D.; Donley, C. L.; Dempsey, J. L., Electrochemical hydrogenation of a homogeneous nickel complex to form a surface adsorbed hydrogen-evolving species. *Chem. Commun.* **2015,** *51* (25), 5290-3.

89. Anxolabehere-Mallart, E.; Costentin, C.; Fournier, M.; Nowak, S.; Robert, M.; Saveant, J. M., Boron-capped tris(glyoximato) cobalt clathrochelate as a precursor for the electrodeposition of nanoparticles catalyzing H_2 evolution in water. *J. Am. Chem. Soc.* **2012,** *134* (14), 6104-7.

90. Spek, A. L., PLATON SQUEEZE: a tool for the calculation of the disordered solvent contribution to the calculated structure factors. *Acta Crystallogr. C Struct. Chem.* **2015,** *71* (Pt 1), 9-18.

91. Sheldrick, G. M., SHELXT - integrated space-group and crystal-structure determination. *Acta Crystallogr. A.* **2015,** *71* (Pt 1), 3-8.

จุฬาลงกรณ์มหาวิทยาลัย
Chulalongkorn University

92. Sheldrick, G. M., Crystal structure refinement with SHELXL. *Acta Crystallogr. C Struct. Chem.* **2015,** *71* (Pt 1), 3-8.

93. Dolomanov, O. V.; Bourhis, L. J.; Gildea, R. J.; Howard, J. A. K.; Puschmann, H., OLEX2: a complete structure solution, refinement and analysis program. *J. Appl. Crystallogr.* **2009,** *42* (2), 339-341.

94. Malthus, S. J.; Wilson, R. K.; Larsen, D. S.; Brooker, S., Acridine-based ligands from cobalt(II) mediated rearrangement of diphenylamine-based starting materials. *Supramol. Chem.* **2015,** *28* (1-2), 98-107.

95. Sickerman, N. S.; Park, Y. J.; Ng, G. K.; Bates, J. E.; Hilkert, M.; Ziller, J. W.; Furche, F.; Borovik, A. S., Synthesis, structure, and physical properties for a series of trigonal bipyramidal M(II)-Cl complexes with intramolecular hydrogen bonds. *Dalton Trans.* **2012,** *41* (15), 4358-64.

96. Sadhu, M. H.; Solanki, A.; Kumar, S. B., Mixed ligand complexes of copper(II), cobalt(II), nickel(II) and zinc(II) with thiocyanate and pyrazole based tetradentate ligand: Syntheses, characterizations and structures. *Polyhedron* **2015,** *100*, 206-214.

97. Lau, N.; Sano, Y.; Ziller, J. W.; Borovik, A. S., Terminal Ni(II)-OH/-OH_2 complexes in trigonal bipyramidal geometries derived from H_2O. *Polyhedron* **2017,** *125*, 179-185.

98. Dai, Y.; Xu, K.; Li, Q.; Wang, C.; Liu, X.; Wang, P., Acridine-based complex as amino acid anion fluorescent sensor in aqueous solution. *Spectrochim. Acta A Mol. Biomol. Spectrosc.* **2016,** *157*, 1-5.

99. Zhang, Z.; Xiao, J.; Chen, X. J.; Yu, S.; Yu, L.; Si, R.; Wang, Y.; Wang, S.; Meng, X.; Wang, Y.; Tian, Z. Q.; Deng, D., Reaction Mechanisms of Well-Defined Metal-N_4 Sites in Electrocatalytic CO_2 Reduction. *Angew. Chem. Int. Ed.* **2018,** *57* (50), 16339-16342.

100. Ma, D.-D.; Han, S.-G.; Cao, C.; Li, X.; Wu, X.-T.; Zhu, Q.-L., Remarkable electrocatalytic CO_2 reduction with ultrahigh CO/H_2 ratio over single-molecularly immobilized pyrrolidinonyl nickel phthalocyanine. *Appl. Catal. B* **2020,** *264*.

101. Singh, S.; Phukan, B.; Mukherjee, C.; Verma, A., Salen ligand complexes as electrocatalysts for direct electrochemical reduction of gaseous carbon dioxide to value added products. *RSC Adv.* **2015,** *5* (5), 3581-3589.

102. Liu, S.; Yang, H. B.; Hung, S. F.; Ding, J.; Cai, W.; Liu, L.; Gao, J.; Li, X.; Ren,

จุฬาลงกรณ์มหาวิทยาลัย
Chulalongkorn University

X.; Kuang, Z.; Huang, Y.; Zhang, T.; Liu, B., Elucidating the Electrocatalytic CO_2 Reduction Reaction over a Model Single-Atom Nickel Catalyst. *Angew. Chem. Int. Ed.* **2020,** *59* (2), 798-803.

103. Wang, Y. R.; Huang, Q.; He, C. T.; Chen, Y.; Liu, J.; Shen, F. C.; Lan, Y. Q., Oriented electron transmission in polyoxometalate-metalloporphyrin organic framework for highly selective electroreduction of CO_2. *Nat. Commun.* **2018,** *9* (1), 4466.

104. Zhu, M.; Chen, J.; Guo, R.; Xu, J.; Fang, X.; Han, Y.-F., Cobalt phthalocyanine coordinated to pyridine-functionalized carbon nanotubes with enhanced CO_2 electroreduction. *Appl. Catal. B* **2019,** *251*, 112-118.

105. Morlanés, N.; Takanabe, K.; Rodionov, V., Simultaneous Reduction of CO_2 and Splitting of H_2O by a Single Immobilized Cobalt Phthalocyanine Electrocatalyst. *ACS Catal.* **2016,** *6* (5), 3092-3095.

จุฬาลงกรณ์มหาวิทยาลัย
Chulalongkorn University

VITA

NAME	METHASIT JUTHATHAN
DATE OF BIRTH	1 December 1995
PLACE OF BIRTH	Bangkok
INSTITUTIONS ATTENDED	B.Sc. (Hons) Mahidol University, 2014-2018
HOME ADDRESS	39/88 Mhoo Ban Hua-na, Nongkae, Hua Hin, Prachuabkirikhun, 77110
PUBLICATION	[1] Atomic- and Molecular-Level Modulation of Dispersed Active Sites for Electrochemical CO2 Reduction. Juthathan M., Chantarojsiri T., Tuntulani T., Leeladee P. Chem. Asian. J. 2022, 17, e202200237. [2] Molecularly Dispersed Nickel Complexes on N-doped Graphene for Electrochemical CO2 Reduction. Juthathan M., Chantarojsiri T., Chainok K., Butburee T., Thamyongkit P., Tuntulani T., Leeladee P. Dalton Trans. 2023, DOI: 10.1039/d3dt00878a.

จุฬาลงกรณ์มหาวิทยาลัย
CHULALONGKORN UNIVERSITY